UNIVERSIDADE DA CORUÑA

PhD Thesis

Automatic computation of the Arteriovenous Ratio and assessment of its effectiveness as a prognostic indicator in hypertension

Sonia González Vázquez

Departamento de Computación

July 2013

PhD Advisors:

Noelia Barreira Rodríguez

Manuel F. González Penedo

Marc Saez Zafra

Dr. Manuel F. González Penedo, Dra. Noelia Barreira Rodríguez y Dr. Marc Saez Zafra

CERTIFICAN:

Que la memoria titulada "Automatic computation of the Arteriovenous Ratio and assessment of its effectiveness as a prognostic indicator in hypertension", ha sido realizada por Dª. Sonia González Vázquez bajo nuestra dirección en el Departamento de Computación de la Universidade da Coruña y concluye la Tesis que presenta para optar al grado de Doctor con la mención de Doctor Internacional.

A Coruña, 09 de julio de 2013

Fdo: Manuel F. González Penedo
Director de la Tesis doctoral
Departamento de Computación
Facultad de Informática
Universidade da Coruña

Fdo: Noelia Barreira Rodríguez
Directora de la Tesis doctoral
Departamento de Computación
Facultad de Informática
Universidade da Coruña

Fdo: Marc Saez Zafra
Director de la Tesis doctoral
Departamento de Economía
Facultat de Ciències Econòmiques i Empresarials
Universitat de Girona

Agradecimientos

En primer lugar me gustaría dar las gracias a mis directores de tesis, Manuel Penedo, Noelia Barreira y Marc Saez, por todo el apoyo recibido durante la etapa de realización de la misma y por transmitirme su optimismo. Penedo, gracias por confiar en mi, por ofrecerme la oportunidad de trabajar en el VARPA, por todo lo que me has enseado, por motivarme y guiarme durante esta etapa. Gracias también por todas esas reuniones infinitas que a pesar de caracterizarse por su extensión siempre han sido muy fructíferas. Noelia, moitas gracias pola túa importante colaboración tanto na tese como nos artigos que publicamos, esto non sería posible sen ti. Gracias por esas correccións, por ver o lado positivo que a min me custaba atopar, polos regalitos incentivadores na etapa final de redacción e por ter sempre un oco para min na túa complicada axenda. En xeral, gracias por preocuparte polo grupo e por responsabilizarte de moitas tarefas deste. Marc, gracias por transmitir tu optimismo y tu energía positiva en todas las reuniones que hemos tenido, por valorar siempre los resultados obtenidos como si se tratasen de lo mejor y por tu colaboración en los artículos que hemos publicado. Gracias por mi estancia de profesora en Girona y por tus regalitos en forma de paper via e-mail.

Gracias a todos mis compaeros del VARPA, ha sido genial compartir estos aos con vosotros. Gracias Marcos, Jorge y José por esas amenas charlas de política e indignación y como no, arterias, venas, AVR's, retinas y procesamiento de imagen en general. Vero, gracias por tu amabilidad y por tu preocupación por el grupo. Cas y Marta, gracias por vuestra ayuda en mi proyecto de fin de carrera y por ser 100% VARPA a pesar de la distancia. Brais, gracias pola túa aportación na tese e polos memory leaks, aínda que curto, foi divertido traballar contigo. Especialmente, gracias Lucía, por ser la mejor compañera de trabajo que uno puede tener, gracias por esos viernes de auto-boicot, por ser la perfecta guía de programación cultural de A Coruña y por compartir conmigo no sólo el interés por el procesamiento de imágenes sino también afficiónes como el cuero y la artesanía en general, gracias por ser como eres.

También me gustaría manifestar mi agradecimiento al equipo médico compuesto por

Antonio Pose, Francisco Gómez-Ulla, Gabriel Coll, Marta Pena-Seijo, María Rodríguez y María Sanmartin, sin cuya colaboración no habría sido posible realizar esta tesis. Especialmente, gracias a María, Marta y María por realizar el tedioso trabajo del etiquetado de los vasos retinianos y el cálculo manual del AVR. También gracias Gabriel por valorar siempre tan positivamente los resultados obtenidos.

Gracias tambin a Antonio Mosquera por las discusiones e historias compartidas en las diferentes reuniones y viajes en las que hemos coincidido.

Obrigada a Aurélio Campilho, Ana Maria Mendonça e Jorge Silva pela recepção muito calorosa na minha estadia em Porto e o bom ambiente de trabalho. Obrigada a Catarina, Carlos e Marlene pelas refeições partilhadas e as aulas de português.

A mis compañeros de MQiTIC de Girona, Carmen y Alex, por guiarme en mis primeros pasos como profesora, me lo pasado muy bien con vosotros. También gracias a Olga Ivina, por esos cafés y por hacerme más amena mi estancia en Girona.

A Paula, Cris, Olaya, Pepa y Juan Luís por las risas y las discusiones que compartimos a la hora del tupper en el CITIC.

Gracias a todos mis amigos por quererme y apoyarme durante este recorrido. Gracias Mitos, Isa, Javi, Meli, Lore, Moro, Yan, Gracia, Héctor, Jalley, Giusi, Diego, Kobe, Lore, Tebas, Iria, Jacobo, Adri, Yuli, Nan, Flavia, Choskar, Carol, chicos/as, se acabó el hablar de la tesis, he terminado, salí de la cueva y estoy aquí de nuevo lista para vosotros.

Héctor, gracias por hacerme reir cada día, sobre todo en esos momentos en los que la tontería, el enfado o el mal genio se apodera de uno sin razón.

Gracias a miña gran familia, a todos os meus primos/as e tíos/as, en especial a Carmen, José e Ramona.

Por último gracias mamá, papá, Eloy, Miguel, Ramo, Celsa e a miñas pequenas María e Antía, por quererme e apoiarme en todos os meus proxectos.

Resumen

La retina es la única parte del cuerpo humano en donde se pueden observar los vasos sanguíneos directamente de una forma no invasiva mediante un examen de fondo de ojo. De esta manera, la imagen de la retina mediante las técnicas de procesamiento de imágenes se convirtió en un campo de clave para el diagnóstico precoz de varias enfermedades sistémicas que provocan alteraciones visibles en dicha imagen. Así, alteraciones en el ancho de los vasos retinianos se asocian con patologías tales como diabetes o hipertensión. De hecho, el estrechamiento de las arterias constituye un indicio precoz de la hipertensión arterial sistémica, siendo una característica del grado I de la retinopatía hipertensiva de acuerdo con la clasificación de Keith-Wagener-Barker. En este sentido, se han realizado esfuerzos para desarrollar programas asistidos por ordenador para medir con precisión los cambios en el ancho de los vasos a través del índice arteriovenoso (IAV), es decir, la relación entre los calibres de las arterias y las venas. Sin embargo, aunque estos sistemas se han usado en muchos estudios con fines de investigación, su aplicabilidad en la práctica clínica diaria es todavía discutida.

En este trabajo, se propone una nueva metodología para el cálculo del IAV con el fin de estratificar el riesgo cardiovascular de los hipertensos. Por un lado, se ha desarrollado un método completamente automático para estimar el IAV en una imagen de fondo de ojo de un paciente. Por otro lado, se propone un sistema para monitorizar el IAV del paciente a lo largo del tiempo. Para este fin, las mediciones del IAV en las diferentes imágenes adquiridas sobre el mismo ojo del paciente en diferentes fechas se estiman usando el mismo conjunto de vasos medidos en las mismas áreas. Por lo tanto, la mediciones obtenidos de esta manera son comparables y precisas, debido a que son independientes en el conjunto de vasos seleccionados para el cálculo.

Las dos técnicas se han integrado en SIRIUS, un sistema web destinado a incluir diferentes servicios en el campo del análisis de la imagen retiniana. El sistema incluye también gestión de pacientes y revisiones, lo que facilita el análisis de las lesiones retinianas causadas por diferentes patologías y su evolución después de un determinado tratamiento.

Además al ser una aplicación distribuída a través de la web, proporciona un entorno de colaboración entre diferentes médicos, investigadores y centros.

Resumo

A retina é a única parte do corpo humano onde se poden observar os vasos sanguíneos directamente dunha maneira non invasiva mediante un examen do fondo do ollo. Desta maneira, a imaxe da retina mediante as técnicas de procesamento de imáxenes converteuse nun campo chave para o diagnóstico precoz de varias enfermidades sistémicas que provocan alteracións visibles en dita imaxe. Así, cambios no ancho dos vasos retinianos asócianse con patoloxías tales como a diabetes ou a hipertensión. De feito, o estreitamento das arterias constitúe un indicio prematuro da hipertensión arterial sistémica, sendo unha característica do grado I da retinopatía hipertensiva dacordo coa clasificación de Keith-Wagener-Barker. Neste sentido, fixerónse moitos esforzos para desenvolver programas asistidos por ordenador para medir con precisión os cambios no ancho dos vasos a través do índice arteriovenoso (IAV), é dicir, a relación entre os calibres das arterias e das veas. Nembargantes, aínda que estes sistemas foron usados en moitos estudios con fins investigadores, a sua aplicabilidade na práctica clínica diaria aínda é discutida.

Neste traballo, proponse unha nova metodoloxía para o cálculo do IAV co fin de estratificar o risco cardiovascular dos hipertensos. Por un lado, desenvolveuse un método completamente automático para estimar o IAV nunha imaxe de fondo de ollo dun doente. Por outra banda, proponse un sistema para monitorizar o IAV dun doente a lo longo do tempo. Para isto, as medicións do IAV nas diferentes imaxes adquiridas sobre o mesmo ollo do doente en diferentes datas fanse usando o mesmo conxunto de vasos medidos nas mesmas áreas. Polo tanto, as medicións obtidas desta maneira son comparables e precisas, debido a que son independentes do conxunto de vasos seleccionados para o cálculo.

As dúas técnicas foron integradas no SIRIUS, un sistema web destinado a incluir diferentes servicios no campo da análise da imaxe retiniana. O sistema inclúe tamén xestión de doentes e revisións, facilitando a análise e estudo das lesións retinianas causadas por diferentes patoloxías e a súa evolución despois dun determinado tratamento. Ademais ao ser unha aplicación distribuída a través da web, proporciona un entorno de colaboración entre diferentes médicos, investigadores e centros.

Summary

Retina is the only part in the human body where blood vessels can be directly observed in a non-invasive way through an eye fundus examination. In this manner, the retinal imaging assisted by image processing techniques became a key field for the early diagnosis of several systemic diseases which cause visible alterations in the fundus image. Thus, changes in the retinal vessel widths are associated with pathologies such as diabetes or hypertension. In fact, arteriolar narrowing constitutes an early sign of systemic hypertension, being a feature for the grade I of hypertension retinopathy according to Keith-Wagener-Barker classification. In this sense, some efforts have been made to develop computer-assisted programs to measure accurately abnormalities in the vessel widths through the arteriovenous ratio (AVR), that is, the relation between arteriolar and venular vessel widths. However, although these systems have been used in many studies for research purposes, their applicability to daily clinical practice is yet discussed.

In this work, a new methodology for the AVR computation is proposed in order to stratify the cardiovascular risk of hypertension. On one hand, a fully automatic method to estimate the AVR in a sample patient's image is developed. On the other hand, an AVR monitoring system to compute the patient's AVR over time was implemented. To this end, the AVR measurements computed in the different patient's images acquired from the same eye at different dates, uses the same set of vessels measured at the same areas. Thus, the measurements achieved in this manner are comparable and precise due to they are independent on the set of vessels selected for the calculus.

The two approaches have been integrated in SIRIUS, a web-based system aimed to include different services in the field of retinal image analysis. It includes patient and checkup management, making easier to analyze the retinal lesions caused by different pathologies and their evolution after a specific treatment. Moreover, being a application distributed via the web, it provides a collaborative environment among different physicians, researchers and medical centers.

1. Resumen

La retina es la única parte del cuerpo humano en donde se pueden observar los vasos sanguíneos directamente de una forma no invasiva mediante un examen de fondo de ojo. De esta manera, la imagen de la retina mediante las técnicas de procesamiento de imágenes se convirtió en un campo de clave para el diagnóstico precoz de varias enfermedades sistémicas que provocan alteraciones visibles en dicha imagen. Así, alteraciones en el ancho de los vasos retinianos se asocian con patologías tales como diabetes o hipertensión. De hecho, el estrechamiento de las arterias constituye un signo precoz de la hipertensión arterial sistémica, siendo una característica del grado I de la retinopatía hipertensiva de acuerdo con la clasificación de Keith-Wagener-Barker. En este sentido, se han realizado esfuerzos para desarrollar programas asistidos por ordenador para medir con precisión los cambios en el ancho de los vasos a través del índice arteriovenoso (IAV), es decir, la relación entre los calibres de las arterias y las venas. Sin embargo, aunque estos sistemas se han usado en muchos estudios con fines de investigación, su aplicabilidad en la práctica clínica diaria es todavía discutida.

En este trabajo, se propone una nueva metodología para el cálculo del IAV con el fin de estratificar el riesgo cardiovascular de los hipertensos. Por un lado, se ha desarrollado un método completamente automático para estimar el IAV en una imagen de fondo de ojo de un paciente. Por otro lado, se propone un sistema para monitorizar el IAV del paciente a lo largo del tiempo. Para este fin, las mediciones del IAV en las diferentes imágenes adquiridas sobre el mismo ojo del paciente en diferentes fechas se estiman usando el mismo conjunto de vasos medidos en las mismas áreas. Por lo tanto, la mediciones obtenidos de esta manera son comparables y precisas, debido a que son independientes en el conjunto de vasos seleccionados para el cálculo.

Las dos técnicas se han integrado en SIRIUS, un sistema web destinado a incluir diferentes servicios en el campo del análisis de la imagen retiniana. El sistema incluye también gestión de pacientes y revisiones, lo que facilita el análisis de las lesiones retinianas causadas por diferentes patologías y su evolución después de un determinado tratamiento.

Además al ser una aplicación distribuida a través de la web, proporciona un entorno de colaboración entre diferentes médicos, investigadores y centros.

2. Metodología

El objetivo de este trabajo es desarrollar un método automático para calcular la *índice arteriovenoso* (IAV) en imágenes de fondo de ojo con el fin de evaluar las alteraciones en el calibre de las arterias y de las venas causadas por diferentes enfermedades. El IAV se ha relacionado con diversas patologías tales como la diabetes, el síndrome metabólico, la hipertensión o el fallo cardíaco entre otros.

Este trabajo se centra en analizar la relación entre el IAV y la hipertensión. La respuesta primaria de los vasos de la retina a la hipertensión sistémica es el estrechamiento arterial, que caracteriza el grado I de la retinopatía hipertensiva. Sin embargo, la dificultad para obtener una medida cuantitativa precisa y fiable del estrechamiento arterial generalizado impide correlacionar el grado I de la retinopatía hipertensiva con la hipertensión. En el primer capítulo de este trabajo se presenta una extensa descripción de la retinopatía hipertensiva, así como de la necesidad de desarrollar métodos fiables para medir el estrechamiento arterial a través del IAV con el fin de estratificar el riesgo cardiovascular asociado a la hipertensión.

El método propuesto para calcular el IAV es completamente automático. De acuerdo con varios estudios [1, 2, 3], el IAV se calcula como ratio entre los calibres de las arterias y las venas medidos en varias circunferencias centradas en el disco óptico. Así, en el Capítulo 2 se describe el método para delimitar la región de interés, es decir, se localiza el disco óptico y los segmentos de vasos en las circunferencias de análisis. El método de localización del disco óptico se basa en un filtrado de diferencia de gaussianas (DoG) y en la transformada de Hough, mientras que las líneas centrales de los segmentos de vasos en las circunferencias de análisis se detectan a través del operador MLSEC-ST.

Las técnicas propuestas para medir el calibre de los vasos y discriminar los vasos en

arterias y venas se describen en el Capítulo 3. El método de medición se basa en modelos deformables, mientras que la clasificación combina un clustering local usando el algoritmo K-means y un seguimiento de los vasos basado en caminos mínimos.

El Capítulo 4 propone el algoritmo para seleccionar el conjunto de segmentos de vasos adecuados para la estimación del IAV que emula la selección realizada por los expertos médicos. Por otra parte, se presenta también un nuevo método basado en el registro de vasos con el fin de calcular el IAV del paciente en imágenes adquiridas en diferentes fechas utilizando el mismo conjunto de vasos medidos en los mismos puntos.

La metodología para estimar el IAV, así como en el método de monitorización se integraron en la aplicación web SIRIUS descrita en el Capítulo 5.

Cada capítulo citado anteriormente incluye además una amplia revisión de otras técnicas presentadas en la literatura para cada paso de la metodología propuesta.

En el Capítulo 6 se resumen los experimentos llevados a cabo para validar la metodología propuesta así como también los estudios clínicos realizados.

Finalmente el Capítulo 7 resume las principales aportaciones del trabajo así como futuras líneas de investigación.

3. Conclusiones y Aportaciones

De acuerdo con la validación realizada en el Capítulo 6 se pueden hacer las siguientes observaciones. Por un lado, el método propuesto para localizar el disco óptico funciona muy bien en imágenes sanas pero presenta limitaciones en algunas retinas enfermas. Esto se debe a que se basa fundamentalmente en la detección de las áreas ms brillantes de la imagen en las que se han detectado un gran número de líneas centrales de vasos. Sin embargo, las imágenes no saludables pueden presentar zonas brillantes que no se corresponden con el disco óptico y donde falsos positivos en las líneas centrales de los vasos son más probables. Por otro lado, en el estudio POSTEL, la detección de vasos se ha comparado con ART-VENA, un método semiautomático para el cálculo del IAV

clínicamente validado. El enfoque propuesto mejora la sensibilidad y reduce los vasos falsos positivos logrados con ART-VENA en una base de datos compuesta por imágenes tomadas en dos centros diferentes.

La evaluación del método de medición del calibre vascular realizada en la base de datos pública REVIEW indica que el método es comparable y, en algunos casos, supera el rendimiento alcanzado por otras técnicas. Sin embargo, las imágenes del conjunto REVIEW con alto reflejo vascular en el centro de los vasos y compresión JPEG causan bordes difusos que evidencian limitaciones en el detector de bordes de Canny. El principal inconveniente de este método es el tratamiento de las imágenes de alta resolución con un alto reflejo vascular en el centro de los vasos, en el que los detectores de las línea centrales de los vasos y los detectores de bordes pueden interpretar como un único vaso dos vasos diferentes. Este fenómeno no aparece si se reduce la imagen. Por lo tanto, un preprocesamiento para localizar o filtrar el reflejo vascular podría mejorar el método.

Con respecto a la clasificación de los vasos en arterias y venas, el algoritmo de clustering local permite a mitigar el efecto de la luminosidad no uniforme en la clasificación, mientras que el método de seguimiento de los vasos proporciona una manera de garantizar la clase de un vaso teniendo en cuenta la información de color a lo largo de la estructura vascular. Otros métodos de clasificación supervisadas y no supervisados, en combinación con varios vectores de características han sido probados y el enfoque propuesto demostró ser el mejor para el conjunto de imágnes utilizadas.

Los experimentos llevados a cabo en un conjunto de imágenes grande para probar el cálculo IAV seleccionando diferentes conjuntos de vasos demostraron que el método proporciona una estimación del IAV próxima a la obtenida por los expertos médicos. Por otra parte, los experimentos han puesto de manifiesto la alta influencia de los vasos seleccionados en el cálculo, y la necesidad de estimar el IAV de un paciente utilizando el mismo conjunto de vasos. Este hallazgo fue presentado también previamente por Knudtson et al. [4] quienes se dieron cuenta de que las fórmulas de Hubbard [2] dependían del número de vasos seleccionados y propusieron una reformulación usando sólo las seis principales arterias y venas.

El sistema de monitorización del IAV es otra importante contribución de este trabajo ya que proporciona una medida fiable de la evolución del calibre vascular. La correlación obtenida entre el IAV calculado por el sistema de monitorización y un experto médico demostró que el sistema se comporta casi como otro experto médico.

La metodología propuesta para calcular el IAV, así como el sistema de monitorización se integraron en la aplicación web SIRIUS. Los estudios clínicos y experimentos realizados a lo largo de este trabajo demostraron que el sistema SIRIUS ofrece un entorno de colaboración perfecto para médicos e investigadores de diferentes centros.

La utilidad del sistema se demostró con las validaciones clínicas realizadas en los estudios POSTEL y VAMPAHICA con imágenes obtenidas en diferentes centros de salud y tomadas con distintos retinógrafos. El primer estudio mostró un incremento en el IAV y en el calibre arteriolar medio en pacientes hipertensos después de seis meses de tratamiento. Por el contrario, el segundo reveló un incremento en el IAV en el cuartil más alto al final de un año de seguimiento mientras la hipertrofia ventricular izquierda y la cantidad de órganos diana dañados experimentaron un resultado favorable. A pesar de estos hallazgos, sería interesante realizar más estudios con mayor número de pacientes y durante un período más largo de seguimiento para definitivamente establecer el AVR como indicador pronóstico en la hipertensión y para estratificar el riesgo cardiovascular.

To my parents

"No one can lie,

no one can hide anything,

when he looks directly

into someone's eyes."

PAULO COELHO

"The eye is the window of the human body

through which it feels its way and enjoys the beauty of the world.

Owing to the eye the soul is content to stay in its bodily prison,

for without it such bodily prison is torture."

LEONARDO DA VINCI

Contents

List of Figures

List of Tables

Chapter 1

Introduction

The transparency of the retina makes it in a direct window for the human vasculature through an eye fundus examination. Thus, some systemic diseases cause alterations in the retinal vessels or in the eye fundus which can be observed in retinal images. In this sense, with the increasing development of image processing techniques, retina imaging constitutes a key for diagnosis support.

Between the cited alterations, the arteriolar narrowing is considered an early sign of hypertension which is rated by the World Health Organization as one of the most important causes of premature worldwide. Some efforts have been made to stratify the hypertension risk from the arteriolar narrowing, however reliable methods which measure alterations in the arteriolar widths are needed.

This chapter is introductory, and it is devoted to describe the main features of the eye fundus image, as well as to characterize the hypertensive retinopathy focusing on the arteriolar narrowing.

In the first section, we give a brief description of the eye's and retina's anatomy, the fundus image and the equipment needed to capture it, as well as the parts and lesions of the retina which are visible in that image. The next section is devoted to characterize hypertensive retinopathy, detailing which lesions are consequence of it. The

Section 1.3 focuses on the arteriolar narrowing lesion and the measure to assess it, that is, the *arteriovenous ratio* (AVR) whose computation is the objective of this work. Finally, in the Section 1.4, a work overview is given.

1.1 Retina

The eyeball is composed of three tunics or layers and a refracting media called the humours. The first and most external tunic is formed by the *sclera* and *cornea*, the second one is composed of *choroid*, *ciliary body* and *iris*; finally, the third and inner tunic is the retina (Figure 1.1).

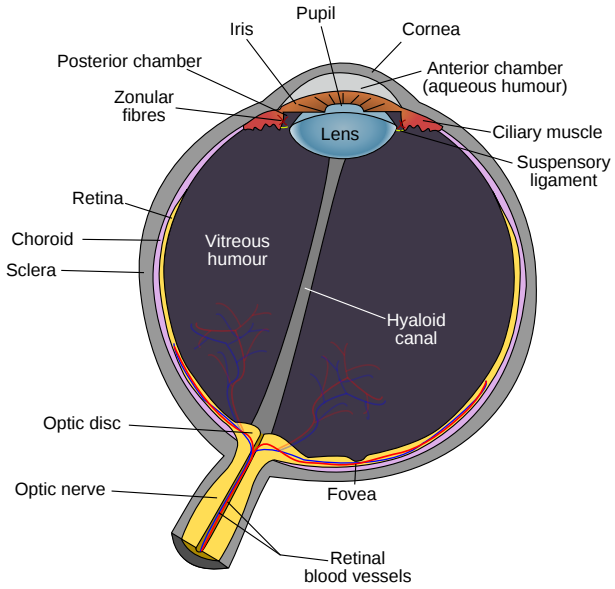

Figure 1.1: Schematic diagram of the human eye.

Despite that the retina is located in a peripheral area, it is actually part of the central nervous system [5] and its function is to translate light into nerve signals and send them to the brain via the optic nerve. There are five types of neurons in the retina which are stacked in layers. Among these, the photoreceptors (rods and cones), are specialized in different aspects of the vision. The former are very sensitive to light and they are

responsible for vision in dim light, whereas the latter are responsible of the visual acuity and color perception.

Regarding the circulation, the retina is irrigated by two vascular networks, the retinal and the choroidal vessels [6]. The latter are the responsible of irrigating the external retina whereas the internal area is irrigated by the central retinal artery. This vessel enters the retina in the optic nerve and branches into four vessels at level of the optic nerve head. Thus, each retina quadrant is irrigated by a vessel. The central retinal artery branches off the ophthalmic artery which, in term, branches off the carotid artery. The venular drainage in the retina is realized almost exclusively through the central retinal vein which drains in the superior ophthalmic vein.

1.1.1 Eye fundus image

Leonardo da Vinci said that the *"The eye is the window of the human body"*. Thus, the eye, and specifically, the retina, due to its transparency and the accessibility to the vascular structures, provides a unique opportunity to study the microvasculature directly in a non-invasive manner.

The first instrument for looking into the eye was invented in 1841 by Charles Babbage, but it was unable to obtain an image with it. It was in 1851 when the ophthalmoscope of Hermann von Helmholtz made possible to observe the human eye fundus. The Augenspiegel (eye mirror) of Helmholtz was a curve mirror with a hole, illuminated by a candle (Figure 1.2). The source light rays passed through the pupil, and the reflected rays from the subject's retina went through the hole, creating the subject's retina image directly on observer's retina. The candle was quickly replaced by the gravity-fed oil lamp, the Argand gas-burning lamp and finally, the bulb, in 1885.

The modern fundus camera was created by the Carl Zeiss Company in 1926. In 1953, with the Kodachrome color film, the Zeiss camera was converted in the standard for color retinal images. The fluorescein angiography supposed a great impact in the retina understanding in 1960. From this, the continuous advances of manufacturers such as

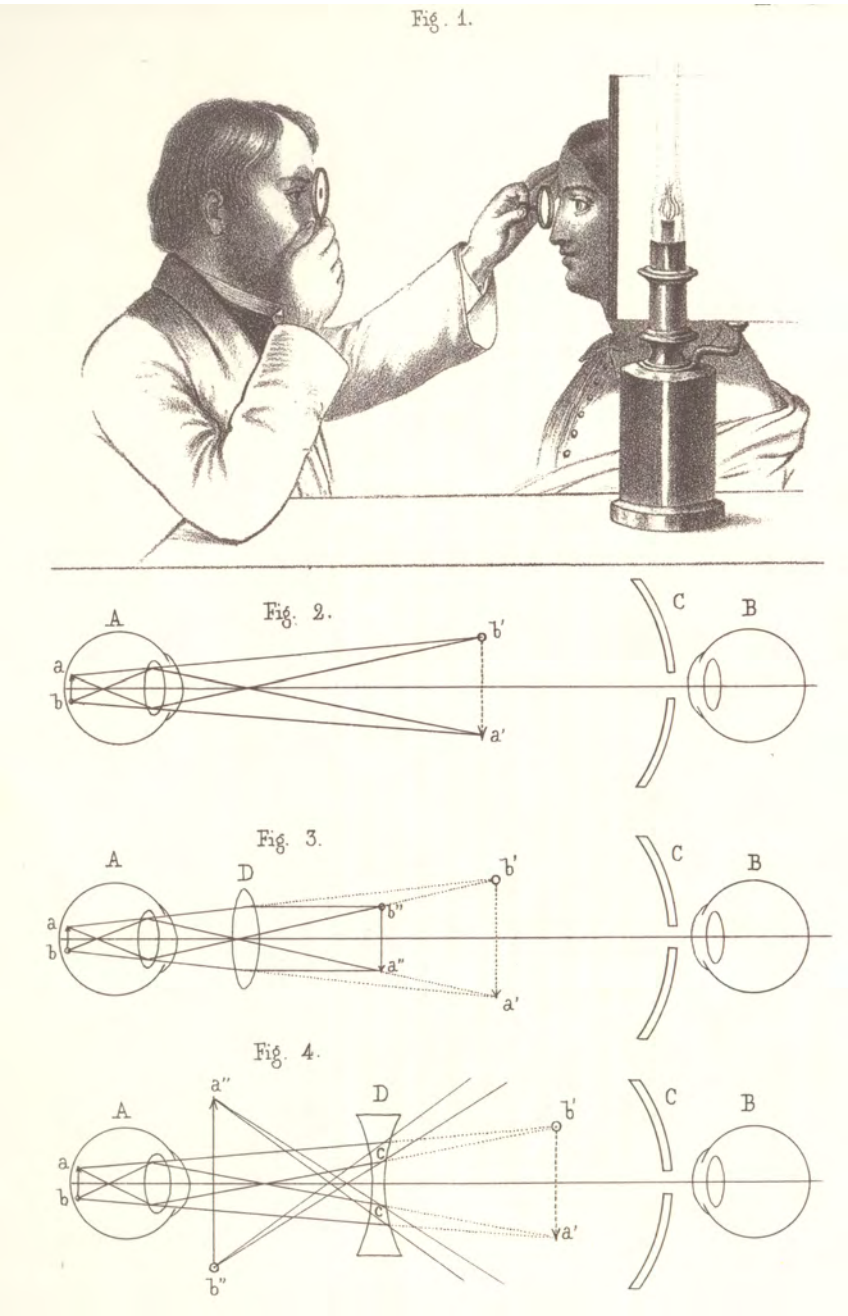

Figure 1.2: Fundus examination with the ophthalmoscope (Fig. 1) and ophthalmoscope operating schemes with a concave mirror (Fig. 2), concave mirror and convex lens (Fig. 3) and concave mirror and concave lens (Fig. 4).

Zeiss, Topcon, or Canon, and the digital photography have revolutionized the field of retinal imaging.

Samples of left and right eye fundus images are shown in the Figure 1.3. This figure shows the quadrants in which the retina is divided for description purposes. Thus, a vertical line divides the retina into *nasal* and *temporal* divisions, whereas an horizontal line divides it into *superior* and *inferior* divisions. Moreover, the area centered on the macula and located between the superior and inferior temporal vessel arcades is called the *posterior pole*. The different parts of the retina that can be observed in an eye fundus examination are shown in the Figure 1.4. The brightest area where the optic nerve exits the retina, is the *optic disc*, *papilla* or *optic nerve head*. Also it is known as *the blind spot* since there are no photoreceptors in this area. It is the main entry of the *retinal vascular network*. The *macula* or *macula lutea* is located approximately 3mm temporal to the optic disc and its diameter is around 1.5mm. The name macula lutea is due to the presence of xanthophyll, a yellow carotenoid pigment. Its center is the fovea, a 0.35mm-wide depression specialized in the visual acuity. Thus, the highest density of cone photoreceptors is in this area.

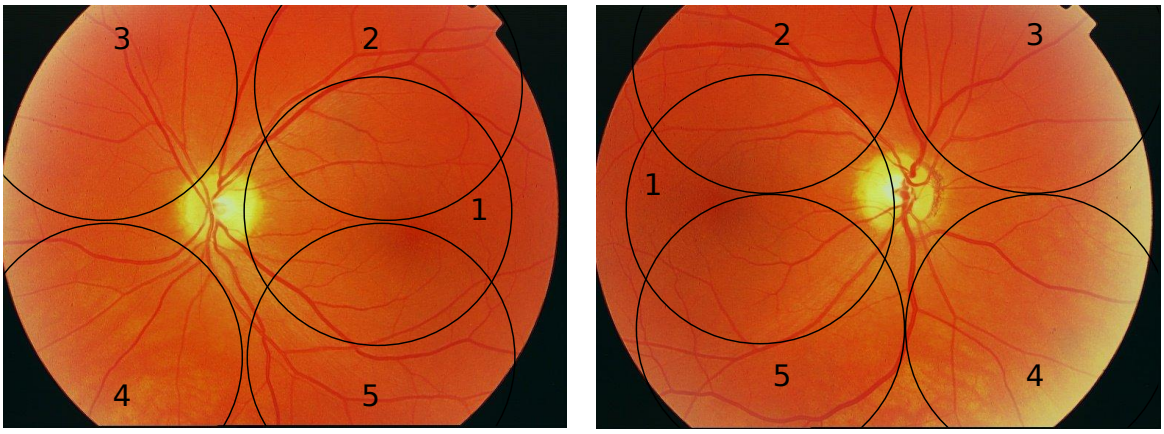

(a) (b)

Figure 1.3: Retinal division in quadrants in (a) left and (b) right eyes. The zone (1) is the posterior pole centered on the fovea, (2) and (5) are the superior and inferior temporal areas, respectively, whereas, (3) and (4) are the superior and inferior nasal zones, respectively.

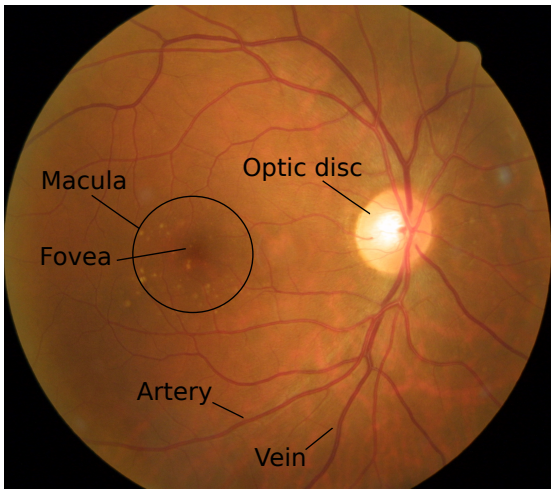

Figure 1.4: Sample of eye fundus image.

1.1.2 Lesions in the eye fundus

Certain diseases cause alterations in retina which are visible in a fundus image. These lesions can be classified according to the part of retina affected: the blood vessels or the retina itself. Some of the lesions are cited below:

- Alterations in the blood vessels
  - *Vessel narrowing o widening.* Several diseases cause narrowing or widening of the retinal vessels which affect veins and arteries differently. Some studies [7] associate the venular widening with hyperglycemia, diabetes and metabolic syndrome whereas hypertension causes a generalized arteriolar vasoconstriction which reduces the arteriolar width visibly. As Figure 1.5 shows, the arteriolar narrowing can be generalized or focal. The arteriolar width must be determined respect to the vein width. Normally the artery-vein relation is 3/4, existing an alteration when it is lower than 2/3. The focal narrowing is due to spasms produced by a no sclerotic arteries.
  - *Arteriovenous nicking.* The effect of the blood pressure over the artery walls can produce sclerosis in the arteries. This can be due to hypertension or due to the aging. The hardened artery compresses the vein which has a thinner

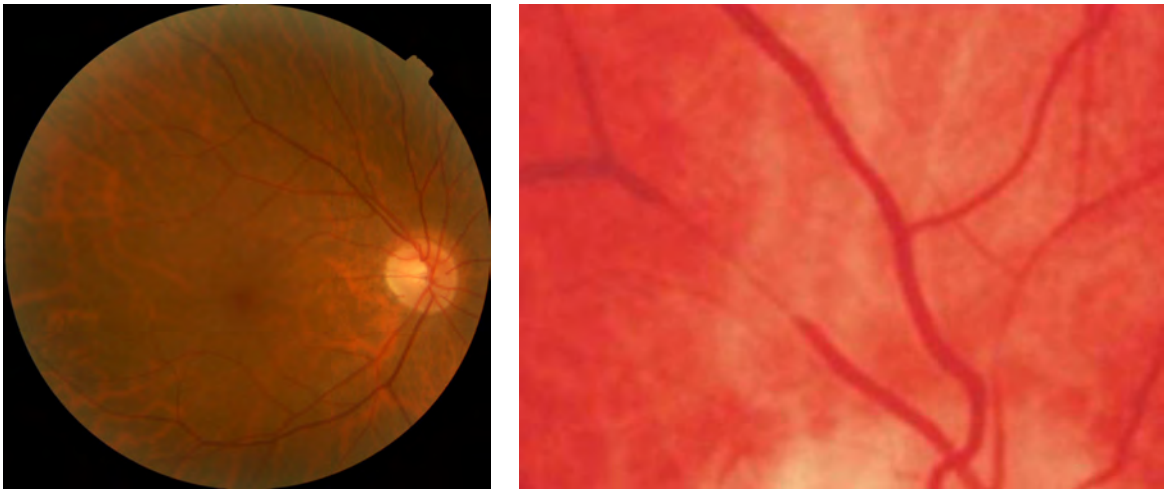

(a) (b)

Figure 1.5: Example of (a) generalized and (b) focal arteriolar narrowing.

wall causing an alteration in the vein width, the *Gunn's sign* (Figure 1.6(a)), or abrupt change in the vein route at the crossing, the *Salus's sign* (Figure 1.6(b)). These alterations can be observed when the artery is over the vein at the crossing, which occurs in 70% of cases.

(a) (b)

Figure 1.6: Example of arteriovenous nicking.(a) Gunn's sign, (b) Salus's sign.

– *Irregularities in the route of blood vessels.* The retinal vessels in normal patients

are slightly crooked and winding. However, the vessel morphology can be modified, becoming more tortuous (Figure 1.7) or straighter and more elongated, in response to pathologies such as hypertension. The tortuosity in big arteries is a sign of vascular sclerosis but it can also appear at early stages of hypertension. Vein tortuosity may not be related to hypertension, but it can increase due to heart failure or hypotension.

Figure 1.7: Example of vessel tortuosity.

– *Vascular reflex changes.* In healthy patients the blood vessel walls are transparent and no visible ophthalmoscopically. Thus, the red colors of arteries and veins are due to blood flow. This flow under the opthalmoscope light, produces a reflex in the vessel wall of 1/3 the vessel width. However, the arteriosclerosis increases the density of the vessel walls so the reflex can be wider. Moreover, the reflex can lose its reddish appearance and becomes more metallic, coppery and wider, the so-called copper wire arteriole (Figure 1.8(a)). If the lost of transparency is total and the central reflex occupies the whole width of the artery is known as silver wire arteriole (Figure 1.8(b)).

– *Neovascularization.* It consists on the proliferation of new blood vessels (Figure 1.9). Their appearance is winding and tortuous and they can arise isolated or in small bunchs.

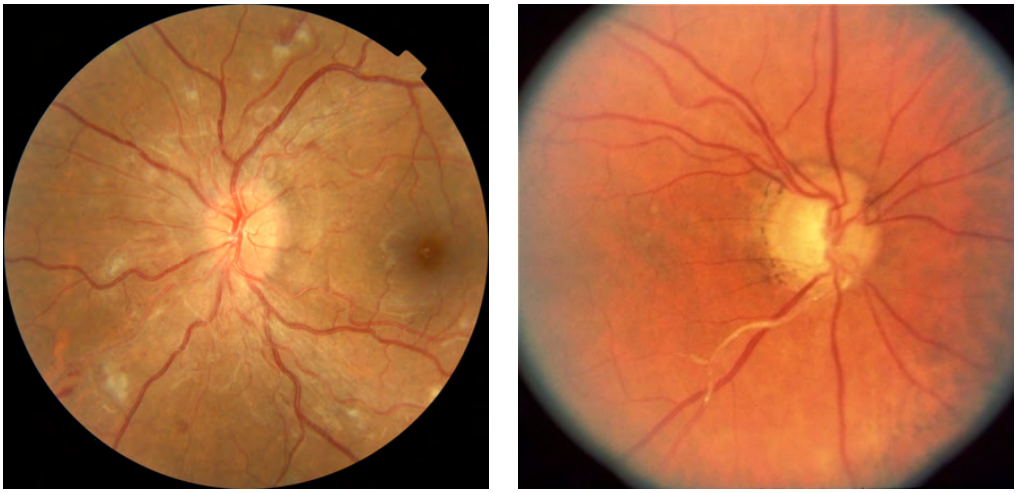

(a) (b)

Figure 1.8: Example of vascular reflex changes.(a) Coper wire arteries, (b) Silver wire arteries.

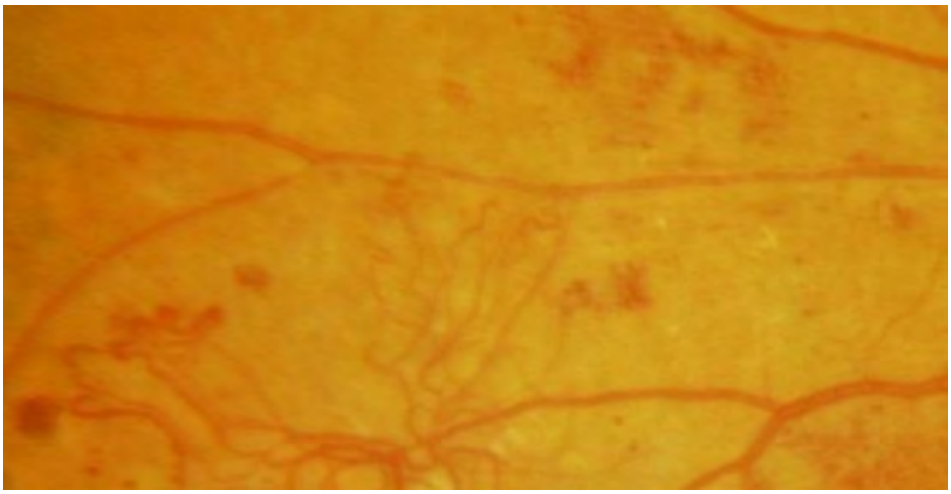

Figure 1.9: Example of neovascularization.

- Alterations in the retina fundus

  – *Hard exudates.* The hard or lipidic exudates, are yellowish deposits (Figure 1.10(a)) of lipids and proteins which come from the extravasation of intravascular content due to an increment in the permeability, or due to the remains of hemorrhages. They are small spots with sharp contours but they tend to group in plaques, rings or stars (Figure 1.10(b)). The possible causes includes: hypertension, diabetes, arteriosclerosis, vasculitis, vascular malformations, and venous occlusions.

(a) (b)

Figure 1.10: Example of hard exudates, (a) isolated or (b) grouped in a macular star.

  – *Soft exudates or cotton wool spots.* They are white and cottony spots bigger than hard exudates with a round or oval shape of ill-defined borders (Figures 1.10(b) and 1.11). They are located at the posterior pole. The soft exudates are due to severe ischemia produced by an intense arteriolar vasoconstriction which can cause necrosis of the artery itself. They are signs of malignant hypertension, diabetes, gravidic retinopathy, dysproteinemia, vasculitis, anemia, leucosis, and venous occlusions.

  – *Aneurysms.* Two kinds can be distinguished: microaneurysms and macroaneurysms. The microaneurysms are small swelling of the vessels, and they are the most characteristic lesion of diabetic retinopathy. The macroaneurysms are

(a) (b)

Figure 1.11: Example of soft exudates.

dilations of the large arterioles of the retina associated with systemic hypertension, exudation and hemorrhages.

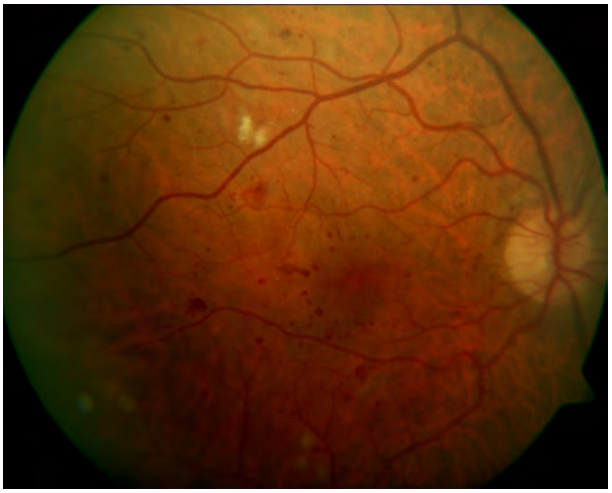

Figure 1.12: Examples of aneurysms.

– *Hemorrhages.* They are blood residues which can occur on the retinal surface, *preretinal hemorrhages* (Figure 1.13(a)), or in the retinal tissue, *intraretinal hemorrhages*, (Figures 1.10(a) and 1.13(b)). The preretinal hemorrhages are large and they usually take on a keel shape. On the contrary, the intraretinal hemorrhages can present a flame or splinter shape if they affect the superficial nerve fiber layer, or, they can have a round or amorphous shape in case of deeper

hemorrhages. They can appear in hypertension, diabetes, blood dyscrasias, trauma as well as subarachnoid and subdural hemorrhages.

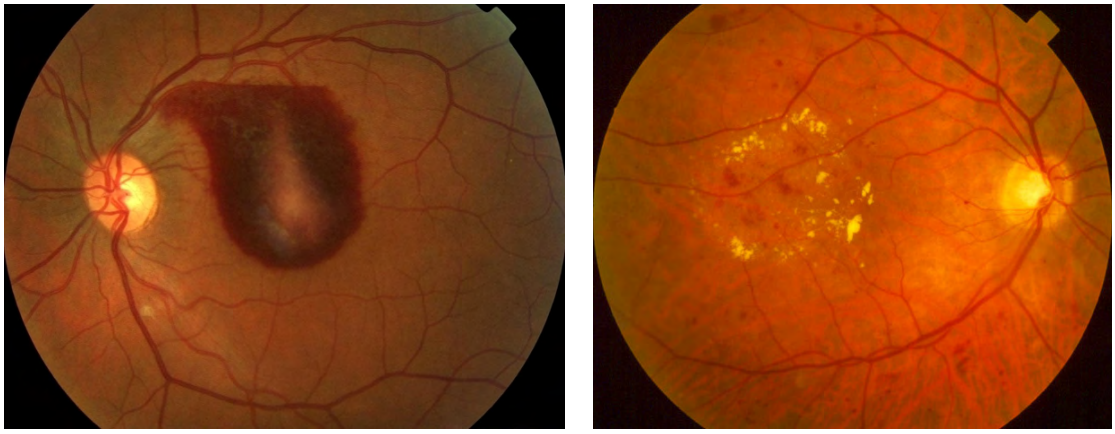

(a) (b)

Figure 1.13: Examples of (a) preretinal and (b) intraretinal hemorrhages, superficial (in flame of splinter) and deeper (rounded).

– *Papilledema.* It is a non-inflammatory swelling of the optic nerve head which affect to patients with increased intracranial pressure and ocular venous outflow obstruction (Figure 1.14). It coexists with other alterations mentioned above as a result of hypertension, although, in malignant hypertension may occur alone.

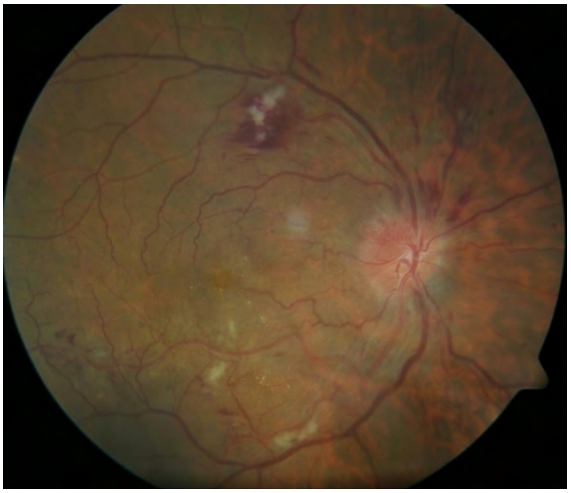

Figure 1.14: Example of papilledema.

1.2 Hypertensive retinopathy

Systemic hypertension is diagnosed by repeatable measurements of an high blood pressure, that is, when the diastolic blood pressure is 90 mmHg or above, or the systolic pressure is 140 mmHg or above [8]. Hypertension increases cardiovascular risk causing target-organ damage, including retinopathy. Thus, since the retina can be visualized directly and in a non-invasive manner, the identification of hypertensive retinopathy is a important way to stratify cardiovascular risk.

The primary response of the retinal arterioles to the systemic hypertension is the vasoconstriction. However, this constriction may not be observed in older patients due to the involutional sclerosis of the arteries caused by aging. In addition, the atherosclerosis can lead as well to alterations in retinal blood vessels.

Thus, since Marcus Gunn's described in 1898 [9] the alterations in retinal vessels in hypertensive patients, several classification systems tried to correlate the observed changes with the disease. The first and most used classification of the retinal alterations related to the hypertension is the Keith-Wagener-Barker [10, 11]. It is based on clinical findings and established four grades of hypertensive retinopathy with increasing severity. In the Scheie's work [12], a modification of this classification is proposed to discriminate between hypertensive and arteriosclerotic abnormalities. Both classifications are shown in the Table 1.1.

Despite these classifications are the standard used to assess the hypertensive retinopathy, several studies have questioned them due to, among others reasons, the poor correlation with the severity of the disease. Thus, other classifications appeared which focus on describing the appearance of the eye fundus rather than grading the retinopathy, such as, the two-grade classification (non-malignant vs malignant) proposed in [13].

As Table 1.1 shows, the alterations which characterize the hypertensive retinopathy are: focal and generalized arteriolar narrowing, hemorrhages, hard exudates, cotton-wool spots, changes in arteriolar reflex or even papilledema. However, the first alteration gener-

Keith-Wagener-Barker [10, 11]		Scheie [12]	
Grade	Features	Grade	Features
		0	No changes
I	Mild generalized retinal arteriolar narrowing	1	Barely detectable arterial narrowing
II	Definite focal narrowing and arteriovenous nipping	2	Obvious arterial narrowing with focal irregularities plus light reflex changes
III	The above and retinal hemorrhages, exudates and cotton-wool spots	3	Grade 2 plus copper wiring and retinal hemorrhages/exudate
IV	Severe grade III and papilledema	4	Grade 3 plus silver wiring and papilledema

Table 1.1: Keith-Wagener-Barker and Scheie classifications of hypertensive retinopathy.

ally consists on an arteriolar narrowing [12]. In fact, this lesion constitutes the first grade of the hypertensive retinopathy in the two classifications. Moreover, nowadays, lesions of grades 3 and 4 such as hemorrhages or exudates are rarely observed [14, 15]. Thus, it seems that the arteriolar narrowing could be the best indicator to stratify cardiovascular risk.

1.3 Arteriolar narrowing and arteriovenous ratio

The previous section showed that the arteriolar narrowing is the primary response of the retinal vessels to the systemic hypertension [12]. However, the difficulty to obtain a reliable quantitative measure of the generalized narrowing prevents to correlate the grades I and II of the hypertensive retinopathy with hypertension, arteriosclerosis, cerebral vasculopathy or other systemic pathologies. For this reason some studies [16] question the use of arteriolar narrowing for the risk stratification in hypertensive patients, whereas this does not occur with the other advanced lesions of eye fundus (exudates, hemorrhages or papilledema) [17, 15]. Also, the European guidelines for the management of arterial hypertension [14, 15] explicitly exclude arteriolar narrowing and the arteriovenous nicking,

the grades I and II, to stratify the cardiovascular risk of hypertension and they confine to research the use of some methods which measure the vessel widths.

In this sense, some efforts have been made to develop no subjective, precise and reproducible methods to measure the degree of narrowing in arteries through the *arteriovenous ratio* (AVR), that is, the ratio between arteriolar and venular vessel widths measured in an area centered in the optic disc. Thus, an automatic procedure which estimate the AVR must locate the optic disc, detect and measure the retinal vessels in the region of interest and classify them into arteries and veins.

The use of more objective methods in some studies such as, the Atherosclerosis Risk in Communities Study (ARIC) [2, 18] or the Blue Mountains Eye Study [19], allows to show the association between the AVR and the hypertension.

In addition, the AVR has been also associated with metabolic syndrome [20], diabetes mellitus [21], cerebral white matter lesions [22], carotid stiffness [23], heart failure [24], cardiovascular morbidity and mortality [25] and stroke [26].

Thus, the aim of this work is the development of an automatic method for the AVR computation. The measure obtained must be repeatable and reliable in order to assess the patient's microvasculature over the time. Furthermore, the connection between alterations in microcirculation and the systemic hypertension will be analyzed, assessing the effectiveness of the AVR as a prognostic indicator of this disease.

The proposed method will be integrated in a telemedicine system to allow the collaboration between physicians and researches working in different places.

1.4 Work overview

This work is organized as follows.

Chapter 2 focuses on delimiting the region of interest where the AVR is estimated. This encompasses the optic disc segmentation and the location of the vascular structures.

Chapter 3 is devoted to explain the most important phases in the AVR computation, these are, the measurement of the retinal vessel widths in the region of interest and their distinction in artery and vein types.

Chapter 4 is devoted to present two procedures for the AVR computation. The former computes the AVR automatically within a patient's image independently, whereas, the latter obtains the measure in new patient's images from an AVR result achieved in a reference image. This last manner is one of the most important contributions of this work, that is, the use of a vessel registration procedure to compute the patient's AVR in distinct images acquired at different times using the same set of vessels, and measured in the same areas.

Chapter 5 presents SIRIUS (System for the Integration of Retinal Images Understanding Services), a telemedicine system for the retinal image analysis where the proposed AVR methods have been integrated.

Chapter 6 shows the results obtained in the system validation as well as the clinical validation.

Finally, Chapter 7 provides a brief overview of some concluding remarks and future directions.

Chapter 2

ROI extraction

The aim of this chapter is to describe the algorithms for identifying the region of interest, that is, the areas where the vessel widths are measured for computing the *arteriovenous ratio* (AVR). In the previous chapter, several methodologies to estimate the AVR have been mentioned. Despite their differences, all of these methods share a common bond: the measurement area, a concentric zone around the *optic disc* (OD) in order to measure the retinal vessels at equidistant points from the vascular network center. Hence, the goal of this chapter is present an automatic method to delimit this region of interest (ROI) where the AVR will be estimated. Thus, the algorithm proposed to detect the OD is described in Section 2.1, whereas, Section 2.2 explains how the vessels are located in several circumferences of analysis concentric to the OD.

2.1 Optic disc location

The *optic disc* (OD) can be considered one of the most relevant structures of the eye fundus since, besides representing an important diagnosis and prevention indicator for several pathologies such as glaucoma and diabetic retinopathy, it is the major landmark to detect other structures in the eye. Thus, the OD location is probably the first stage of any automatic algorithm for retinal analysis. In this case, it is an essential step to develop

an automatic tool for AVR computation.

2.1.1 Review of available methods

The OD is normally the brightest area in the fundus image and it is the entrance into the eyeball of the optic nerve and the blood vessel network. These two characteristics of the OD constitute the principal bases used in the most OD location techniques.

Looking through the techniques found in the literature, the OD location issue can be divided into two different problems: the location of the OD center and the OD segmentation, that is, its boundary extraction. Most of the approaches which resolve the first problem rely on template matching [27, 28, 29] and on identifying the area with the highest intensity or color variation respect to adjacent blood vessels [30, 31]. In some cases, the obtained OD center is roughly located and it must be readjusted by the segmentation method. The boundary extraction techniques are mainly based on the Hough transform [31, 32, 33] and deformable models [28, 29, 34].

Specifically, Akita and Kuga [35] proposed locating the OD by vessel backtracking. Mendels et al. [34] used morphological filtering to remove the vessel structures and GVF-based snakes to find the OD boundary. Walter and Klein [36] approximated the OD locus by the centroid of the brightest parts in the luminance of the HSL color space obtained by an area threshold, whereas the OD boundary is located in the red component of RGB color model applying a watershed transformation. Foracchia et al. [37] presented a new method that consist of modeling the main retinal vessels by two parabolas which have a common vertex, the OD center. A thresholded edge mask result of Sobel operator is used as the input of the circle Hough transform in [32]. Hoover and Goldbaum [38] proposed a fuzzy vessel convergence as main feature to locate the OD position. The OD center is found as the intersection point between finite lines (vessel segments). If the convergence is not strong, the center is approximated by the brightest point after an image equalization. In [39], after a vessel tree segmentation and a vessel direction map identification, the optic disc is located by matching its neighbor vessels to an expected vessel's direction filter.

Niemeijer et al. [40] reformulated the problem of finding a certain structure in retina images as a regression problem. For that, they made some assumptions about the way in which the image has been captured such as centered in fovea or centered in OD. In [33] three different methods are combined to get a reliable initial approximation of the OD center. The first method approximates the center by the point of largest difference between the maxima and minima intensity in a neighborhood. The second one proposes as center the point of maximum intensity variance; and the third one selects the maximum of a Gaussian low pass filter. The boundary segmentation is performed using the components R and G of the RGB color space in parallel combining morphological and edge detection techniques. Finally, a Hough transform is applied to readjust the OD center. Recently, Mendonça et al. [41] proposed a new method to measure the vessel convergence founded in entropy of vessel directions.

2.1.2 Proposed method

The main purpose of this step is obtain a precise location of the OD center since it is essential for the AVR calculus, whereas an approximated OD segmentation is enough to delimit the region of interest where the vessels will be measured. The procedure to detect the OD used combines an intensity-based approach, and another based on the convergence of the vessel tree. The aim of the former is to delimit the region of interest where the OD is approximately situated, whereas, the latter tunes the segmentation by the circular Hough transform [42] using the centerlines and the edges of the vessels.

The algorithm is based on the approach proposed in [43]. First, the region of interest (ROI) is demarcated using a blob detection method, the *Difference of Gaussian* or DoG operator. Thus, given the input image $I(x, y)$, the difference of Gaussian is defined as the subtraction between two blurred version of $I(x, y)$ smoothed with two different scaled Gaussian filters.

Given a two-dimensional Gaussian filter, $g_\sigma(x, y)$ with variance σ^2

$$g_\sigma(x, y) = \frac{1}{\sqrt{2\pi\sigma^2}} e^{-(x^2+y^2)/2\sigma^2} \tag{2.1}$$

the difference of Gaussian can be defined by the following equation

$$\begin{aligned} g_{\sigma_1}(x,y) * I(x,y) - g_{\sigma_2}(x,y) * I(x,y) = \\ = \frac{1}{\sqrt{2\pi\sigma_1^2}} e^{-(x^2+y^2)/2\sigma_1^2} * I(x,y) - \frac{1}{\sqrt{2\pi\sigma_2^2}} e^{-(x^2+y^2)/2\sigma_2^2} * I(x,y) \end{aligned} \tag{2.2}$$

Hence, the DoG as an operator or convolution kernel is determined by next formula

$$DoG = g_{\sigma_1}(x,y) - g_{\sigma_2}(x,y) = \frac{1}{\sqrt{2\pi}} \left[\frac{1}{\sigma_1} e^{-(x^2+y^2)/2\sigma_1^2} - \frac{1}{\sigma_2} e^{(x^2+y^2)/2\sigma_2^2} \right] \tag{2.3}$$

where σ_1 and σ_2 take typical values of the optic disc radius, being $\sigma_2 > \sigma_1$. For the images of the experiments, we have used $\sigma_1 = 30$ and $\sigma_2 = 60$ pixels.

The ROI center, that is, the first approximation of OD center (c'_x, c'_y) is located at the maximum of the difference of Gaussian

$$(c'_x, c'_y) = \underset{x,y}{arg\ max} \{DoG * I(x,y)\} \tag{2.4}$$

However wrong OD detection can happen within images which present areas brighter than the optic disc. To avoid this situation, vascular evidences are taking into account to obtain the first approximation of OD center. Then, since the optic nerve is the input of the vascular network, a neighborhood centered on the OD center must contain multiple vessels. Thereby, the vessel centerline binary image I_C is calculated by the *Multilocal Level Set Extrinsic Curvature* (MLSEC) enhanced by the *Structure Tensor* (MLSEC-ST) operator proposed in [44] and it is explained in detail in the Appendix A. It requires that the 1% of the pixels in a squared neighborhood of size σ_1, $\aleph(\sigma_1)$, centered in the expected OD center belong to centerline vessels. Hence the equation 2.4 could be rewritten as follows

$$(c'_x, c'_y) = \underset{x,y}{arg\ max} \{DoG * I(x,y) \ / \sum_{(i,j)\in\aleph(\sigma_1)} I_C(i,j) > 0.01\sigma_1^2\} \tag{2.5}$$

The ROI is bounded by cropping the input image around the center (c'_x, c'_y) using domain information about the optic disc diameter.

$$ROI = I(x,y) \begin{cases} x \in [c'_x - offset, \ldots, c'_x + offset] \\ y \in [c'_y - offset, \ldots, c'_y + offset] \end{cases} \tag{2.6}$$

Figure 2.1 shows the result of DoG and the final ROI as well as the green channel of the RGB original image which it is the input image of the OD location method.

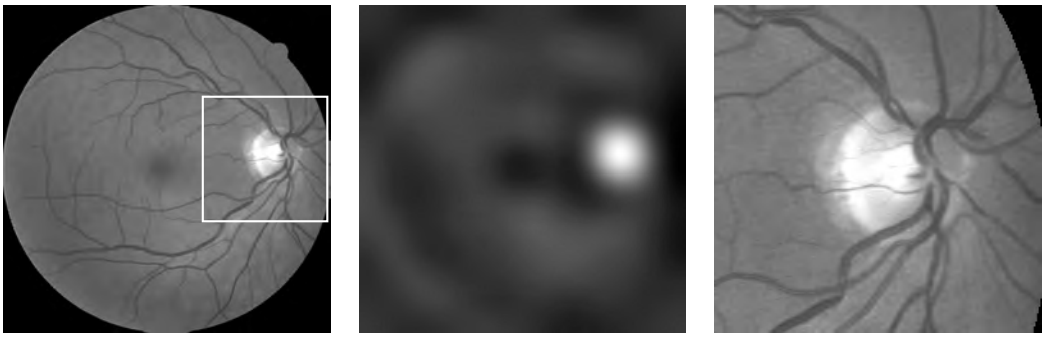

(a) (b) (c)

Figure 2.1: Optic disc ROI detection. (a) Input green channel of RGB color space. (b) DoG result whose maximum value will be the rough optic disc center. (c) Cropped region of interest.

The *circular Hough transform* [45] is appropriated for the OD segmentation since it allows determine the parameters of a circle when a number of points lying on that circle are known. The Hough transform is widely used in Computer Vision to recognize shapes which can be defined by parametric equations. It considers the characteristics of the shape not in the image space, but in the parameter space. That is, each point in the image space votes for a shape determined by its parameters. These votes are stored in an accumulator array. The maximum of the accumulator array corresponds to the desired shape. In case of circle detection, all circles of radius r and center (c_x, c_y) passing through a point (x, y) obey the next parametric equations:

$$\begin{aligned} x &= c_x + r\cos(\theta) \\ y &= c_y + r\sin(\theta) \end{aligned} \tag{2.7}$$

Hence, the accumulator array is a 3D structure of size $N_x \times N_y \times N_r$, representing the space of parameters center-radius delimited by the limits $([c'_x - c_{offset}, c'_x + c_{offset}], [c'_y - c_{offset}, c'_y + c_{offset}], [r_{min}, r_{max}])$. The values for the images used in the experiments performed were $c_{offset} = 40$, $r_{min} = 35$ and $r_{max} = 50$ pixels.

Thus, for each voting edge pixel $p = (x, y)$ and for each possible radius, given the orientation θ_p computed by the gradient, the center to vote is obtained working out the

value of c_x and c_y in the equation 2.7 and obtaining the closest center in the accumulator array. The value of each vote is inversely proportional to the radius size. After that, a Gaussian function is applied to the accumulator array at each dimension to vote not only for an unique center and radius but a neighborhood in order to minimize round-off errors and diffuse edges.

The points which votes in the Hough transform are the edge points of the ROI performing with the Canny operator. However, as it is shown in the Figure 2.2(a), the result of the Canny operator includes not only the optic nerve edge, but also the edges of the vessel structures and noise. So, it is necessary a procedure to avoid the vessel edges participate in the Hough transform voting. To this end, the image I_C computed previously and cropped to the ROI (Figure 2.2(b)) is used to discard the vessels from the voting. Hence, the points suitable for the OD circle voting, P_{Hough}, are the subset of edges points which are not close to a centerline point (Figure 2.2(c)).

$$P_{Hough} = \{(x,y)/I_{Edge}(x,y) = 1 \wedge \sum_{(i,j)\in\aleph(\sigma)} I_C(i,j) = 0\} \tag{2.8}$$

where I_{Edge} and I_C are the binary edge and centerline images, respectively, in the ROI and $\aleph(\sigma)$ is the neighborhood of size σ whose value depends on the image size. For images with a resolution of 768×576, we used $\sigma = 6$, a value around the width of large vessels.

Hence, the center and radius of the OD are those parameters which maximizes the accumulator array of the Hough transform applied to the subset of points defined in the Equation 2.8 (Figure 2.3).

2.2 Retinal vessel detection

As the location of the optic disc, the detection of the retinal vascular tree is a fundamental step in the development of computer-assisted diagnostic systems. Vessel features as length, tortuosity, width and branching index are extensively used by physicians to detect several pathologies at early stages.

(a) (b) (c)

Figure 2.2: Location of the Hough transform input points. (a) Edge points result of Canny edge detector in the ROI, (b) Centerline points result of the MLSEC-ST operator in the ROI, (c) Edge points that votes in the Hough transform.

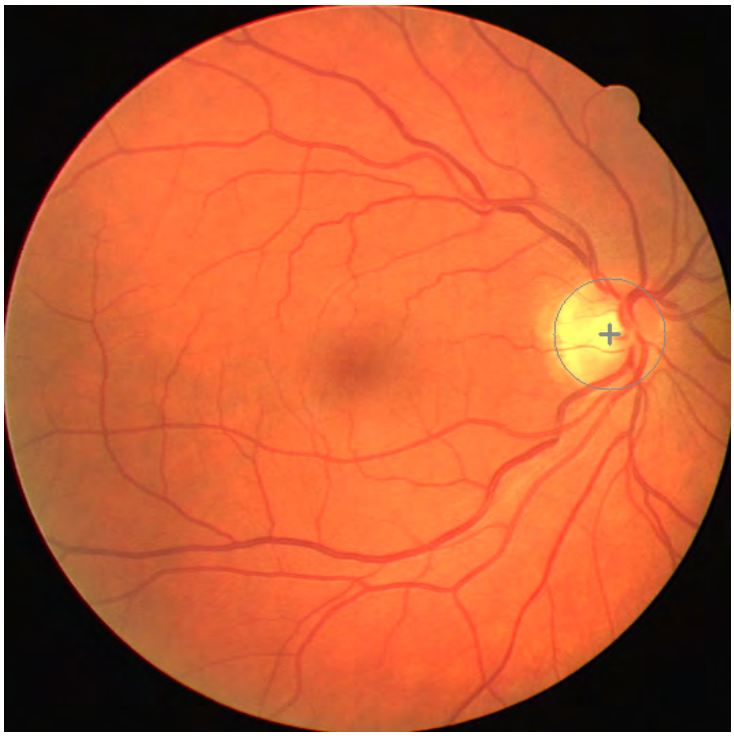

Figure 2.3: Final optic disc center and boundary location through the circle Hough transform.

2.2.1 Review of available methods

The difficulty of detecting the retinal vessel lies in its similarity in shape and gray level with some background features. Furthermore, the presence of noise, pathologies, or the vessel central light reflex, especially in high-resolution images, make the task more difficult. Many authors have suggested methods to segment the retinal vascular network. Recently, Fraz et al. [46] presented a complete survey of the vessel tree segmentation techniques. The authors performed a classification of existing methods among which we highlight the next ones.

- *Matched filtering algorithms:* filters the image with a 2D kernel which tries to model a vessel feature in different orientations [47, 48, 49, 50].
- *Pattern recognition techniques:* classifies the pixels into vessels and background in a supervised or unsupervised manner. Some examples of the supervised methods are the k-NN classifier [51, 52], the Gaussian mixture model [53] or the AdaBoost algorithm [54]. The Fuzzy C-means [55] or the or a entropy based [56] are examples of the unsupervised segmentation methods.
- *Morphological operators:* extracts the vessel shape, such as the edges or the vessel skeleton based on mathematical morphology [57, 46].
- *Tracking algorithms:* starts with a seed from the centerline or edges of vessels and follows the entire vessel guided by direction or other local information [58, 59].
- *The model based approaches:* are subdivided into *profile models* where the cross-sectional profile are fitted by one or several Gaussian functions [47, 48] and deformable models [60, 61].

2.2.2 Proposed method

The proposed method seeks to locate the retinal vessels in the circumferences of analysis where their widths will be measured. The purpose is not to segment the entire vessels

but locating their centerlines in order to use them as seeds of deformable models in the vessel width measurement stage. The technique was proposed by Caderno el al. in [62]. Thus, the MLSEC-ST crease detector (Appendix A) algorithm and a subsequent crease tracking to ensure their continuity are applied. Figure 2.4 shows a schema of the vessel detection model.

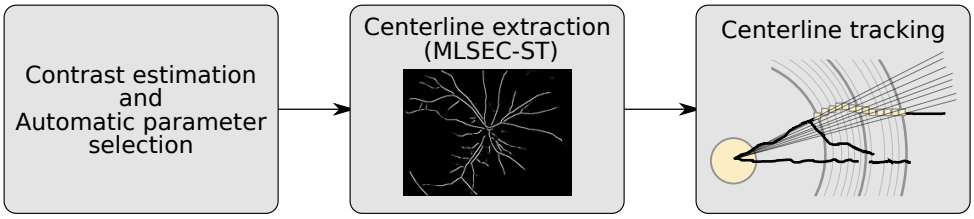

Figure 2.4: Schema of the retinal vessel detection model.

The number and quality of the creases extracted are heavily influenced by the values taken by parameters of the MLSEC-ST operator as Figure 2.5 shows. In this way, the authors proposed an automatic adjustment of parameters depending on the characteristics of the input image, specifically, depending on its contrast. Thus, the images were classified into four classes according to their contrast (low, medium, high and very high) and the parameters were optimized for each class. The image contrast is estimated by analyzing the pixel intensity in the first circumference of analysis, the so-called *linear profile*. As Figure 2.6 shows, the vessels are darker than the background, so they appear as valleys in the linear profile. Thus, the deeper the vessels, the greater the contrast of the image. Thereby, the contrast can be estimated by the variability of the linear profile extreme values, these are, the minimum values located in the valley middle points and the maximum ones located between valleys. Before computing the maximum and minimum values an average filter is applied to minimize the image noise (Figure 2.6). The variability of the linear profile extreme values is computed with the average absolute deviation, $\bar{D}$ as follows:

$$\bar{D} = \frac{1}{n} \sum_{i=0}^{n} |e_i - \mu| \tag{2.9}$$

where e_i represents the intensity of the i-extreme, μ is the average of the extreme inten-

sities and n is the number of extremes. Thus, the values of $\bar{D}$ are used to classify the images into the four contrast categories.

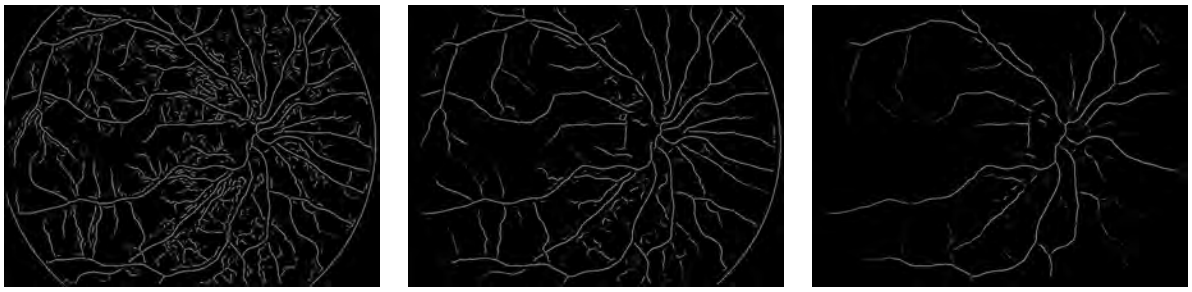

(a) (b) (c)

Figure 2.5: Examples of centerline images obtained from the MLSEC-ST operator using different parameters.

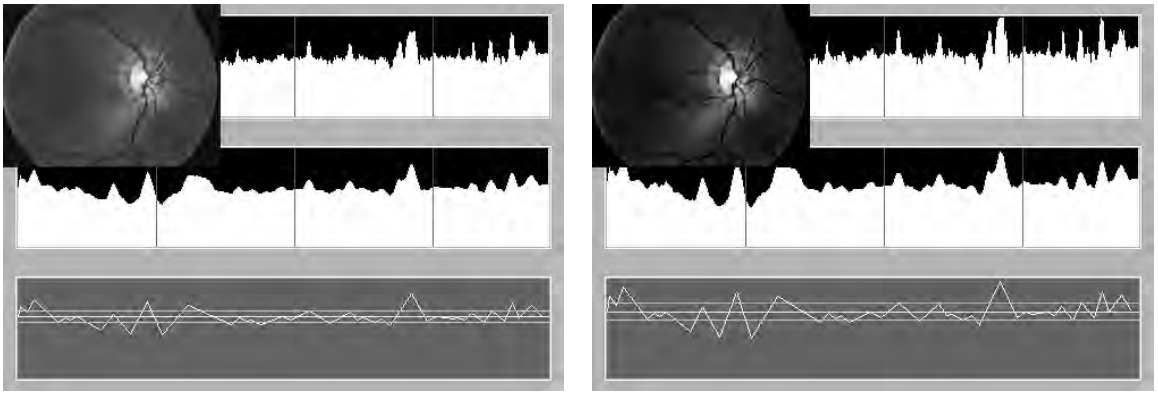

(a) (b)

Figure 2.6: (a) Original histogram of the circumference intensity, smoothed histogram after applying the average filter, histogram extrema where the goodness extrema variance is used as contrastness measure. Middle, upper and lower lines represent μ and the $\mu - \sigma^2$ and $\mu + \sigma^2$ of the extrema intensities. (b)The same graphics in (a) obtained increasing the image contrast artificially.

After the crease extraction, the centerline vessel points in each circumference of analysis C_r, CP_{C_r}, are the crease points which belong to the circumference in the radius of analysis, that is:

$$\underset{r_0 \leq r < r_m}{CP_{C_r}} = \{(x,y)/I_{C_r}(x,y) = 1 \wedge I_{Crease}(x,y) = 1\} \tag{2.10}$$

where I_{C_r} is the mask image of the r-circumference, I_{Crease} is the image result of the crease extraction and m are the number of radius of analysis.

However, due to the presence of noise in the image two undesirable situations may happen: structures which do not belong to vessels are detected as a crease point or discontinuities of a crease in the radius of analysis cause the loss of that vessel (Figure 2.7). Thereby, a tracking is performed with two main purposes in mind: one, to verify the continuity of each crease and avoid false positives as well as loss of vessels; second, to obtain a centerline segment which will be used in the next phase. To this end, the tracking algorithm analyzes the creases in $2n+1$ circumferences spaced a unit distance and which range from $r-n$ to $r+n$. $n=10$ was used to guarantee that small creases coming from noise are not taken into account and to avoid vessel bifurcations and crossovers which are most likely in a bigger area. At each circumference $C_i, i \in \{r-n, r-n+1, \ldots, r+n\}$, the centerline vessel points, p_i, are those crease points which belong to the circumference C_i in the same manner as it was defined in the Equation 2.10. Thus, the Equation 2.10 can be rewritten as follows:

$$\underset{r-n\leq i\leq r+n}{CP_{C_i}} = \{p_i(x,y)/I_{C_i}(x,y) = 1 \wedge I_{Crease}(x,y) = 1\} \tag{2.11}$$

Then a thresholding is applied to avoid false positive creases. For that, the intensity in a 3×3 neighborhood centered in each possible vessel point is analyzed. Then, the point is considered as belonging to the background if the highest intensity in that neighborhood is less than a threshold called the *crease minimum force* ($f=150$). Formally this can be expressed as follows:

$$\underset{p_i(x,y)\in CP_{C_i},\, i\in\{r-n,\ldots,r+n\}}{p_i \in Background} \iff max\{I_{Crease}(k,l)\ ,(k,l) \in \aleph(\sigma)\} < f \tag{2.12}$$

where $\sigma = 3$.

In addition, another situation must be considered: in a specific circumference i, close crease points may belong to the same vessel segment v_{ij}. This is the case of creases parallel to the circumference of analysis or bifurcations located over it. In order to detect if these points are part of the same vessel segment, the euclidean distance between each

pair of centerline points is calculated. The centerline points belong to the same vessel if the distance is less than a threshold d. Formally this can be expressed as follows:

$$p_1\ , p_2 \in v_{ij} \Longleftrightarrow distance(p_1, p_2) < d,\ \ p_1\ , p_2 \in CP_{C_i} \tag{2.13}$$

where $d = 9$ was used and $distance$ is the euclidean distance.

Finally, the angles between the line connecting each centerline point with the optic disc center (c_x, c_y) and the X axis are calculated in order to track the centerline points along the different circumferences. Hence, two centerline points in consecutive circumferences are registered as belonging to the same vessel segment v_{ij} if their angular difference is less than a threshold t_θ (Figure 2.7).

$$\underset{p_1 \in CP_{C_i},\, p_2 \in CP_{C_{i+1}}}{p_1\ , p_2 \in v_{ij}} \Longleftrightarrow |angle(c, p_1) - angle(c, p_2)| < t_\theta \tag{2.14}$$

where $angle(c, p_1)$ and $angle(c, p_2)$ are the angles which form the points p_1 and p_2 with the optic disc center and the abscissa axis and $t_\theta = 0.052$ radians ($3°$) was used.

Each time a centerline point is registered as part of a vessel, V_j, a vote is cast to that vessel. At the end, only the vessels whose number of votes exceeds $2n/3$ votes will be taken into account.

$$V_j = \left\{ v_{ij}\ /\ \sum p \in v_{ij} > \frac{2n}{3} \right\} \tag{2.15}$$

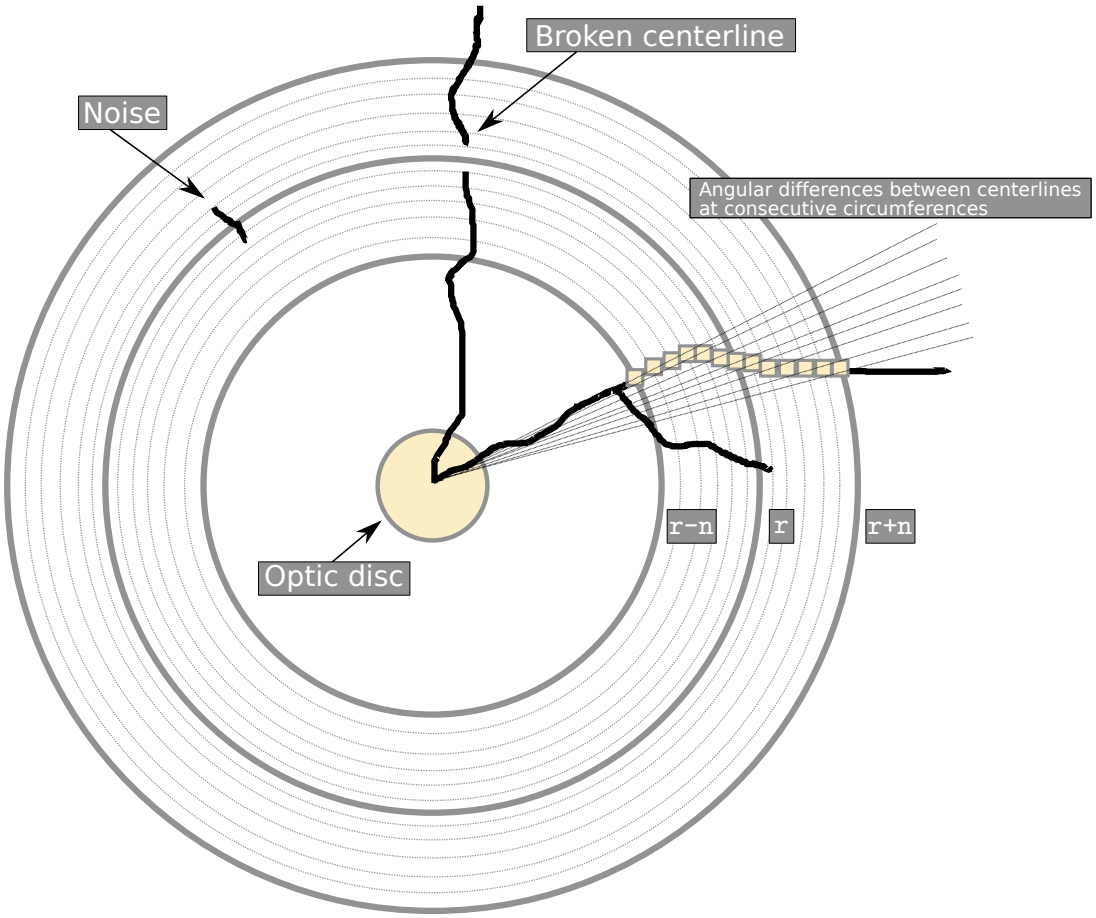

Figure 2.7: Vessel centerline tracking schema.

Chapter 3

Width measurement and vessel classification

This chapter covers, perhaps, the two most important steps in the automatic calculation of the *arteriovenous ratio* (AVR): These stages are the precise measurement of retinal vessel widths and their separation between arteries and veins.

The proposed techniques for both stages as well as other approaches found in the literature are discussed in detail in the two sections of this chapter.

3.1 Vessel width measurement

Normal aging, diabetes, hypertension or atherosclerosis, among other factors can lead to alterations in the vessel width. Thus, the automatic measurement of the retinal vessel width plays an important role in diagnosis and assessment of the patient condition. Accurate measurement is wholly dependent on the vessel tree segmentation. In turn, this task is complicated by diverse factors such as the wide variety of images (resolution, cameras, centers,...), low and variable contrast, alterations in vessels and background caused by different pathologies or the vessel central reflex. Moreover, precise segmentation algorithms are time-consuming, making them useless for clinical practice.

In this section a brief review of some approaches proposed in the literature is provided. After that, the proposed method to width measurement is described. This algorithm is fast and precise. It takes as input the vessel centerline segments detected in the previous phase. From these lines the entire vessel segment is demarcated and its width measured.

3.1.1 Literature review

Numerous algorithms have been presented in the literature to segment the retinal vascular tree. However, not many of them calculate the retinal vessel width. Among them, Brinchmann-Hansen and Heier [63] presented in 1986 the Half-Height Full-Width (HHFW) algorithm which defines the width as the distance between the "half height points" on the left and right sides of the initial midpoint of the profile. To locate the two points, the minimum and maximum intensity levels are computed at each side, and the points are located where the profile crosses the midpoint in intensity between the minimum and maximum. The Gregson's method [64] applies a thresholding to extract the vessels from the background and obtains the centerline by thinning. The vessel is measured in the centerline normal direction by fitting a rectangle to the vessel profile, estimating the area under the profile by the area under the rectangle. Zhou et al. proposed in 1994 a 1-D Gaussian method to fit the vessel profile [65]. Latter, in 2004, Lowell et al. [66] modeled the vessel profile as a 2-D Gaussian to take into account the light reflex. Mosquera et al. presented ART-VENA [67] a semiautomatic system to measure the retinal width. It detects as vessels the valleys in a gray level profile along a circumference centered on the optic disc whose height exceeds a specific threshold. Moreover, the valleys should have continuity in radial direction through several circumferences separated one pixel. Once the edges have been detected and fitted to a line, the vessel width is achieved by the line segment perpendicular to the edges. In Al-Diri's et al. method (ESP) [61], the tram-line algorithm is used to locate the vessel centerlines and two pairs of active contour models are used to detect the vessel boundaries. Xu et al. presented a graph-based method [68] in order to detect the two vessel boundaries simultaneously. Recently, Kumar et al. introduced the unsupervised linear discriminant analysis diameter measurement (ULDM)

[69]. This technique consists on locating the vessel edges first and then classifying the intensity profiles into background or vessel sections by means the LDA classifier.

3.1.2 Proposed method

The purpose of the method is obtain a precise measurement of the vessels widths from the centerline segments located in the previous step. The width measurement of each vessel segment detected in the previous step is achieved by a *snake*. First, the snake is initialized at the corresponding centerline segment and the snake energies are defined. Then, the snake deformation is performed until a minimum energy is achieved. Finally, once reached a stable configuration the width is measured. The algorithm is outlined in Figure 3.1.

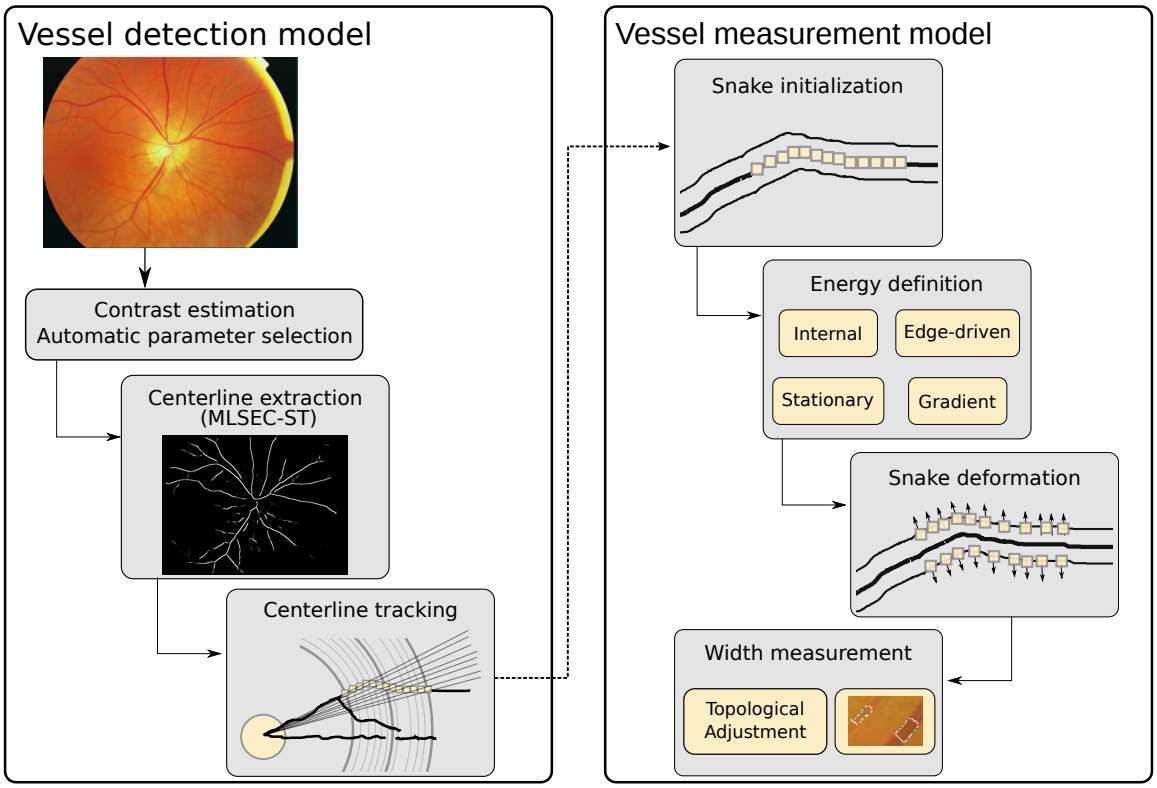

Figure 3.1: Schema of vessel width measurement approach.

Snake model

The method based on snakes used to measure the vessel widths was originally proposed in [62, 70]. A snake [71] is a contour defined within the image which evolves to fit some image features guided by internal and external forces. The internal force controls its flexibility and elasticity whereas the external force points it towards the feature edges. Its shape becomes stable achieving a minimum level of energy when the snake reaches the target feature edges. Thus, the snake can be defined by $\upsilon(s) = [x(s), y(s)]$, where $x(s), y(s)$ are the x and y coordinates along the contour and $s \in [0, 1]$ is the parameter domain. Discretizing the model a snake node with coordinates (x_i, y_i) can be referenced by υ_i.

Hence, the width of each vessel segment is determined by a specific snake. Adapting the snake model to the specific domain includes to define the snake shape, its energy terms and the seed, that is, its initial contour points. In this case, the vessel centerline segment result of the vessel location step constitutes the snake seed. In particular, the initial snake contour consist of two chains of nodes initialized at the points of the centerline segment, as Figure 3.2 shows. The advance direction of both chains of nodes is normal to the vessel centerline but with opposite senses to reach the two vessel boundaries. There are two kind of nodes: *common nodes* and *corner nodes*. The former fit the vessel edges, whereas the latter are adjusted to the corners of the vessel segment to be measured.

Snake energies

The snake energy to be minimized is described as follows

$$\int_0^1 E_{snake}(\upsilon(s))ds = \int_0^1 E_{int}(\upsilon(s))ds + \int_0^1 E_{ext}(\upsilon(s))ds \tag{3.1}$$

where E_{int} and E_{ext} represent the internal and external energy respectively.

The internal energy for this model can be written as

$$E_{int}(\upsilon(s)) = \alpha(s)\left|\frac{\partial \upsilon_s(s)}{\partial s}\right| + \beta(s)\left|\frac{\partial^2 \upsilon_s(s)}{\partial s^2}\right| \tag{3.2}$$

where the first and second term represent the first and second order derivatives, respectively. The parameters $\alpha(s)$ and $\beta(s)$ control the snake shape. Large values of $\alpha(s)$

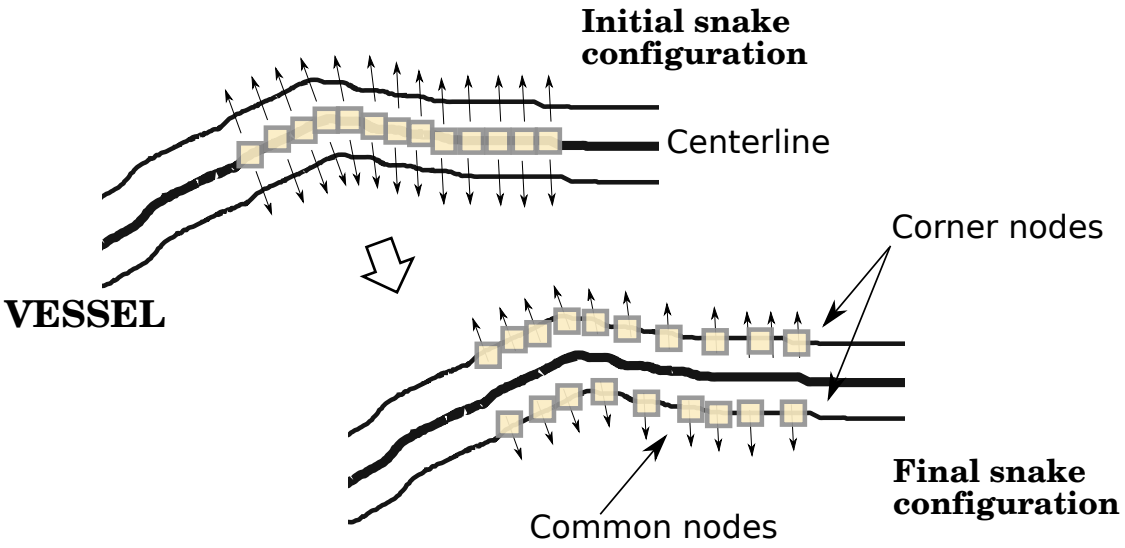

Figure 3.2: Evolution of snake nodes.

makes the snake stretch more and more, whereas large values of $\beta(s)$ makes the snake bend. These values are constant for common nodes, specifically we have used $\alpha(s) = 0.25$ and $\beta(s) = 0.01$. This $\alpha(s)$ value causes neighboring nodes tend to be closed since this is the configuration which minimizes the energy but avoiding entanglement, whereas $\beta(s)$ generates continuous and smooth curves. The corner nodes have null internal energy ($\alpha(s) = \beta(s) = 0$) which implies the presence of discontinuities in the corners. Thus, these nodes interact individually guided only by the external forces without any bonding force between them.

The derivatives in each node v_i are estimated using the technique of the finite differences as follows

$$\left|\frac{\partial v_i(s)}{\partial s}\right| = v_i - v_{i-1} = (x_i - x_{i-1})^2 + (y_i - y_{i-1})^2 \tag{3.3}$$

$$\begin{aligned}\left|\frac{\partial^2 v_i(s)}{\partial s^2}\right| &= v_{i-1} - 2v_i + v_{i+1} \\ &= (x_{i-1} - 2x_i + x_{i+1})^2 + (y_{i-1} - 2y_i + y_{i+1})^2\end{aligned} \tag{3.4}$$

The external energy which attracts the snake to the target shape can be expressed by

the following equation

$$E_{ext}(\upsilon(s)) = \gamma\bar{\eta} + \delta E_{dist}(\upsilon(s)) + \epsilon E_{grad}(\upsilon(s)) + \omega E_{stat}(\upsilon(s)) \tag{3.5}$$

where $\bar{\eta}$ is the dilation pressure, $E_{dist}(\upsilon(s))$ is the edge-driven energy, $E_{grad}(\upsilon(s))$ is the gradient energy, $E_{stat}(\upsilon(s))$ is the stationary energy and γ,δ,ϵ and ω are the energy weights whose values have been established to 1.0, 2.0,1.5 and 0.4, respectively.

The dilation pressure, $\bar{\eta}$ is a vectorial magnitude which adjusts the direction and sense of advance of each snake node.

The edge-driven energy of a node, $E_{dist}(\upsilon_i)$ is given by the distance to the nearest vessel edge. The vessel edges are computed by the Canny operator [72]. Thus, the edge-driven energy is defined by

$$E_{dist}(\upsilon_i) = dist(\upsilon_i, I_{canny}) \tag{3.6}$$

where I_{canny} is the edge image and $dist$ represents the euclidean distance.

These two terms are responsible for reaching the vessel edges. On the contrary, the two latter terms are stooping forces which have been introduced in the model to compensate the image noise and the imprecisions of the edge detector. The gradient energy, $E_{grad}(\upsilon(s))$ stops a node if its gradient is negative, that is, contrary to the advance direction. For a node, υ_i, the gradient is computed as the gray level difference in two positions of the node in the input image as it is shown below

$$grad(\upsilon_i) = I(\hat{\upsilon}_i) - I(\upsilon_i) \tag{3.7}$$

where $\hat{\upsilon}_i$ is a possible new position of the node according to the advance direction and υ_i is its current position.

Thus, the gradient energy is defined as follows

$$E_{grad}(\upsilon_i) = \begin{cases} 0 & \text{if } grad(\upsilon_i) \geq 0 \\ grad(\upsilon_i)^2 & \text{otherwise} \end{cases} \tag{3.8}$$

Finally, the stationary energy is based on the idea that probably a node should stop (keep on moving) if their adjacent nodes stopped (kept on moving). In this manner, it

prevents that a node moves without control when its neighboring nodes have stopped or that a node stops in a local minimum when its neighboring nodes keep on moving. Being m the number of adjacent nodes, the stationary energy is described by the following equation

$$E_{stat}(v_i) = 1 - exp\left(\frac{-1}{2m}\sum_{j=i-m}^{i+m} E_{ext}(v_j)\right) \tag{3.9}$$

Snake deformation

The snake deformation is performed by a greedy algorithm. Thus, at each step of the algorithm, each non stable snake node is moved to its optimum energy level as Algorithm 1 describes. This process is repeated until all nodes are stable, that is, they achieved their minimum energy, or the maximum number of iterations has been reached. In order to locate the new position of each node, the snake energy at three adjacent positions in an eight neighborhood is computed. The three adjacent positions correspond to the position given by the direction and sense of the dilation pressure $\bar{\eta}$ and its two neighbor positions which form angles of $-45°$ and $45°$ with the dilation pressure vector.

In addition, once the positions and energies of all snake nodes have been updated, we check if the distance between two consecutive common nodes exceeds a certain threshold. If this happened, a new node is inserted in the middle point of the two nodes as Algorithm 2 describes. However, if the maximum number of nodes allowed in each snake is exceeded, the insertion fails and the snake is invalidated.

Topological check

After the energy minimization, the snake contour should have a parallelogram shape and the nodes should be positioned in the vessel edges. However, image noise and discontinuities in the edge image may cause some nodes are placed outside or inside the edges. Hence an adjustment of snake contour is needed to correct the wrong nodes. First, the wrong nodes are identified and after that a regression correction model is applied to reorganize

Algorithm 1 Snake deformation algorithm

Definitions:

- $v_i(t) = (x, y)$: snake node v_i in the current position at the step t
- $v_i(t+1)$: snake node v_i in the position at the step $t+1$, $v_i(t+1) \in \aleph(3)$, where $\aleph(3)$ is 3×3 neighborhood centered on $v_i(t)$
- $\bar{\eta}_{v_i}$: dilation pressure which gives the direction and sense of advance of the node v_i
- $\alpha = angle(\bar{\eta}_{v_i})$: angle which forms the dilation pressure vector with the abscissa axis
- $(x_\alpha, y_\alpha) \in \aleph(3)$: the position in the neighborhood $\aleph(3)$ given by the angle α
- $E_{snake}(v_i(t))$: the current energy of node v_i
- E_{min} and (x_{min}, y_{min}): minimum energy and position where E_{min} is obtained, respectively
- $iter$: current number of iterations, and $maxIter$: maximum number of iterations

Initialization:

- Set $maxIter$ to be 100, and set $iter$ to be 0

Body:

- While a snake node is unstable and $iter$ is less than $maxIter$
  - For each $v_i(t) = (x, y) \in snake$
    - Compute $E_{snake}(x_\alpha, y_\alpha)$, $E_{snake}(x_{\alpha-45^\circ}, y_{\alpha-45^\circ})$ and $E_{snake}(x_{\alpha+45^\circ}, y_{\alpha+45^\circ})$
    - Set E_{min} to $min(E_{snake}(x_\alpha, y_\alpha), E_{snake}(x_{\alpha-45^\circ}, y_{\alpha-45^\circ}), E_{snake}(x_{\alpha+45^\circ}, y_{\alpha+45^\circ}))$
    - Set (x_{min}, y_{min}) to the position with energy equal to E_{min}
    - If E_{min} is greater than or equal to $E_{snake}(v_i(t))$
      - Set v_i to stable
    - Else
      - Set $E_{snake}(v_i(t+1))$ to E_{min}
      - Move the node v_i to (x_{min}, y_{min}), $v_i(t+1) = (x_{min}, y_{min})$
  - Add one to $iter$ and Add new snake nodes if it was necessary (Algorithm 2)

Algorithm 2 Algorithm for addition of new nodes in a snake

Definitions:

- $\upsilon_i = (x_i, y_i)$: snake node
- $\upsilon_{i+1} = (x_{i+1}, y_{i+1})$: snake node consecutive to the node υ_i
- $\upsilon_j = (x_j, y_j)$: new node
- $\bar{\eta}_{\upsilon_i}$: dilation pressure which gives the direction and sense of advance of the node υ_i
- $\bar{\eta}_{\upsilon_j}$: dilation pressure which gives the direction and sense of advance of the new node υ_j
- $E_{snake}(\upsilon_j)$: energy of the new node υ_j
- $maxDist$: maximum allowable distance between nodes

Initialization:

- Set $maxDist$ to be 10

Body:

- For each $\upsilon_i = (x_i, y_i) \in snake$ and $\upsilon_i \in common\ nodes$
  - If $distance(\upsilon_i, \upsilon_{i+1})$ is greater than $maxDist$
    - Add new node $\upsilon_j = (x_j, y_j)$ to $snake$
    - Update x_j to $\frac{x_i + x_{i+1}}{2}$ and y_j to $\frac{y_i + y_{i+1}}{2}$
    - Update $\bar{\eta}_{\upsilon_j}$ to $\bar{\eta}_{\upsilon_i}$
    - Compute $E_{snake}(\upsilon_j)$

them. If the correction is not possible, the snake is ruled out since it is inappropriate to be measured.

A node, v_i, is considered as wrong if it satisfies any of the next conditions:

- The minimum distance between v_i and the snake seed is greater than the largest allowed vessel width, λ_{dist}, which depends on the image resolution.
- As edges are parallel to the centerline, the angles that form each with the abscissa axis should be similar. Thus, v_i is a wrong node if the angle formed by the seed and abscissa axis, and the angle formed by v_i, its next node and the abscissa axis differ more than a threshold $\lambda_{ang} = 0.081$ rad.
- The number of iterations needed for v_i to reach its final position and the average of the iterations needed by the nodes of the same edge differ more than a threshold $\lambda_{iter} = 4$.

Mathematically, these conditions can be expressed as follows

$$v_i \in \{\text{Wrong nodes}\} \Leftrightarrow \begin{cases} dist(v_i, seed) > \lambda_{dist} \\ |ang(v_i, v_{i+1}) - ang(seed)| > \lambda_{ang} \\ \left| iter(v_i) - \frac{1}{k}\sum_{j=1}^{k-1} v_j \right| > \lambda_{iter} \end{cases} \tag{3.10}$$

where *dist* is the euclidean distance, *ang* is the angle with respect to abscissa axis, *iter* represents the number of iterations and k is the number of nodes in the same snake edge of v_i.

Once the wrong nodes are detected, a simple linear regression model is applied to the right nodes from left and right edge independently, achieving two regression lines. For each line, the explanatory variable is selected depending on what is the dominant axis, abscissa or ordinate axis, according to the next equations

$$\begin{aligned} y - \bar{y} &= \frac{\sigma_{xy}}{\sigma_x^2}(x - \bar{x}) \\ x - \bar{x} &= \frac{\sigma_{xy}}{\sigma_y^2}(y - \bar{y}) \end{aligned} \tag{3.11}$$

where $\sigma_x y$ is the covariance and σ_x^2, σ_y^2 are the X and Y variances, respectively. A minimum percentage of right nodes (75%) is required in order to apply the regression model, otherwise, the snake is discarded. Moreover, the adjustment quality of the regression model is measured by the *coefficient of determination*, R^2, which in case of the simple linear regression, is equal to the squared of the *correlation coefficient*. The adjustment is good enough when $R^2 > 0.75$, or else the snake is ruled out.

$$R^2 = \rho_{x,y}^2 = \left(\frac{\sigma_{xy}}{\sigma_x \sigma_y} \right)^2 \tag{3.12}$$

Vessel measurements

Having the final configuration of the snake, the next goal is to estimate the vessel width from it. The euclidean distance between the vessel edges can be used to obtain the vessel width. However, in order to remove noise, the input image has been smoothed by a convolution with a Gaussian mask in the edge detection. Thus, the measurement of the vessel width using a simple distance measure can be imprecise since the standard deviation of Gaussian smoothing often shifts the real edges. Hence, a parabolic regression model has been implemented and combined with the euclidean distance to obtain an accurate vessel width.

Seven profiles perpendicular to the centerline are considered within each snake. At each profile, j, two distance measures are computed: the euclidean distance between the profile end points (Figure 3.3), $\hat{\omega}_{j\_euc}$, and a distance based on the parabolic regression model, $\hat{\omega}_{j\_par}$. Thus, the profile gray levels are fitted to a parabola. To this end, only five points in the profile are taken into account: the end points, the point located at the vessel centerline segment and the two points with the maximum gray level placed on either side of the latter. The parabola is generated using these five points, being the dependent variable the gray level and the explanatory variable the euclidean distance to the centerline point. The width of each profile is compute as the average of both measures as follows

$$\hat{\omega}_j = \frac{\hat{\omega}_{j\_euc} + \hat{\omega}_{j\_par}}{2} \tag{3.13}$$

The final vessel width, $\hat{\omega}$, is estimated by the average of the three central values of the seven profiles widths. Assuming that the widths have been ordered, this can be expressed as follows

$$\hat{\omega} = \frac{\hat{\omega}_3 + \hat{\omega}_4 + \hat{\omega}_5}{3} \tag{3.14}$$

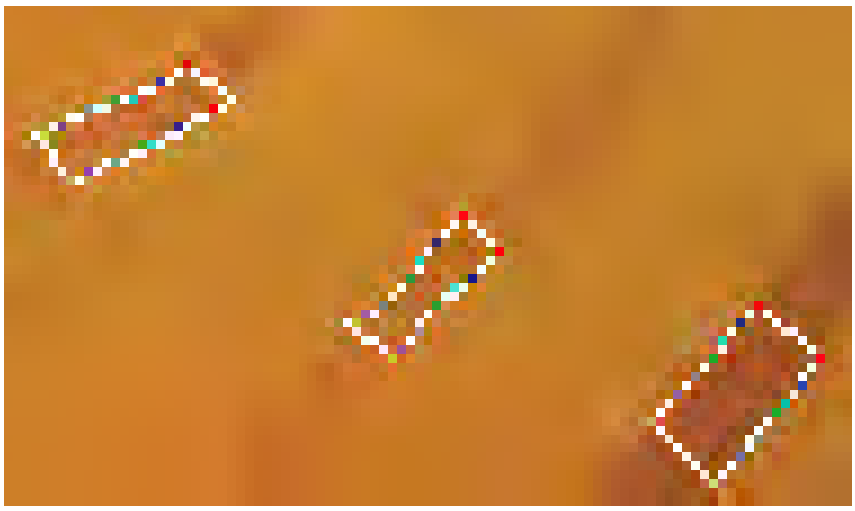

Figure 3.3: Seven end points perpendicular to the vessel centerline considered for the width measurement (color points). White points depict the snake parallelogram.

3.2 Vessel classification

This section tackles the characterization of retinal vessels into arteries and veins. Despite the efforts made in the last years by several authors to solve this problem, a precise characterization remains an open issue. According to medical experts, most of the proposed approaches use color information to separate the two types of vessels automatically, since arteries and lighter than veins. However, this difference in color is practically imperceptible in small vessels. Furthermore, other peculiarities of retina images hinders the classification task. On one hand, the lack of intra-image color homogeneity due mainly to low quality image acquisition processes and the spherical surface of the eye exposed to a non-uniform illumination. On the other hand, the inter-image variation in color and lightness related to biological characteristics, such as skin pigmentation [73] or caused

by different devices and agents involved in the capturing process. Thus, considering alternatives to mitigate the influence of the lightness variability is a mandatory question. Between these, the lightness and contrast normalization, and performing the classification in local areas, are the alternatives considered in this work.

3.2.1 Literature review

Even though numerous works on vessel segmentation have appeared in the literature, the classification of vessels has not gained momentum until recently. The techniques found in the literature to discriminate between arteries and veins can be divided in two categories: tracking-based and color-based methods. The former are mostly semiautomatic since are based on spreading the manual classification made by a medical expert along the vessel tree [74, 75, 76]. To this end, an algorithm to track the vessels and identify the crossovers and bifurcations is needed. Their capacity to classify the entire vascular tree is their main advantage. On the contrary, the latter ones do not require user interaction and they base the classification mainly on color features [77, 78, 79, 73, 80]. Among these methods, Simó and de Ves proposed in 1999 [77] the first automatic method, a Bayesian pixel classifier which distinguished between background, fovea, veins and arteries. Li et al. [78] based their approach on the fact that central light reflex is more apparent in arteries. To this end, the vessel profiles, represented by two Gaussian functions, are the input of a supervised minimum distance classifier. Grisan and Ruggeri [79] identified arteries and veins using a Fuzzy C-means clustering. To resolve the lightness and contrast variability problem, they proposed to apply a contrast normalization and divide the retinal image into four quadrants which are classified independently. The mean of H in HSL color space and the variance of R in RGB are used as classification features. An error rate of 12.4% was obtained in a dataset of 24 images. Jelinek et al. [73] tested 13 different classifier algorithms implemented in the Weka toolbox [81] in a set of 8 images. The best results were achieved with the Naïve-Bayes, the Decision Table and the J48 classifiers, obtaining an error of 30% at the test phases. Niemeijer et al. [80] distinguished between artery and vein centerline pixels using a supervised method over a set of 12 features. An area of

0.88 under a ROC curve has been achieved in a dataset composed of 20 images. Recently, Zamperini et al. [82] performed several tests using different supervised classifiers along with color and contrast features located inside and outside the vessels. They reported interesting findings: the same features achieved best results with a small resolution image whereas the most discriminant feature was the contrast between vessels and background. However, despite these results, a high accuracy in the classification in large data sets is still a pending challenge.

3.2.2 Proposed method

The methodology proposed to classify the retinal vessels combines color and tracking based methods [83, 84, 85]. The former involves a local clustering of the vessel segments measured in the previous section. The latter one, based on the *minimal path* approach [86] (Appendix C), connects the vessel segments which belong to the same retinal vessel and combines the local clusterings to ensure the classification. In this way, the local clustering avoids the influence of color variability in the classification whereas the tracking strategy prevents a high reliance on local color information. Figure 3.4 summarizes the main stages of the proposed methodology.

Local clustering

The aim of the local vessel clustering [87, 83, 84, 88] is to classify the vessel segments detected in the circumferences of analysis minimizing the influence of the lightness and contrast variability. To this end, each circumference is classified separately and the vessel segments found are grouped into overlapping subsets which are classified independently.

The color features used to classify the vessels are obtained from the *profiles*, a 1-pixel thick lines perpendicular to the vessels within the snake parallelogram (Figure 3.5). To this end, we determine first the snake contour points that lie on the right and left edges. After that, each set of contour points is fitted to a line by the *linear least square algorithm*. Then, we calculate the line perpendicular to the right edge line which intersects the left

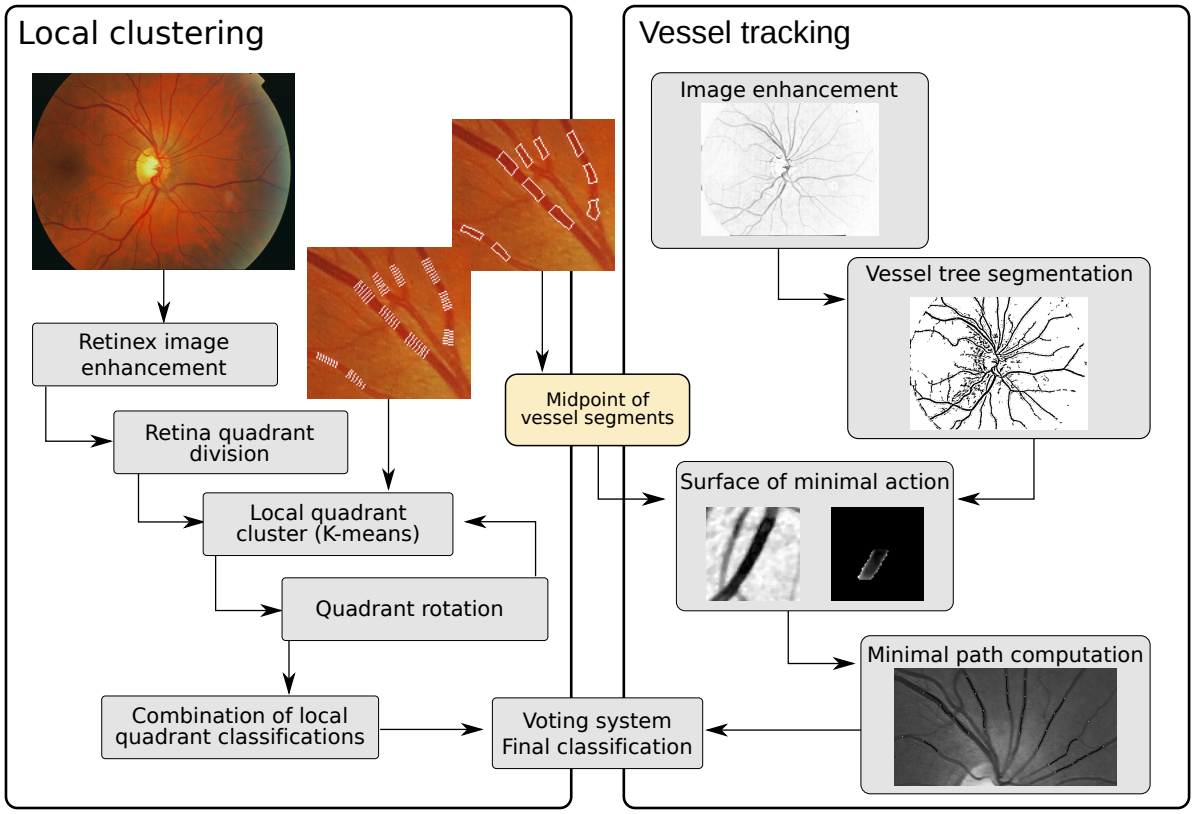

Figure 3.4: Main stages of the vessel classification methodology.

edge line. The profile is the line segment delimited by both edges. The pixels that belong to the profile line are determined by the *Bresenham's line algorithm*. The number of profiles traced in each vessel segment depends on the parallelogram size.

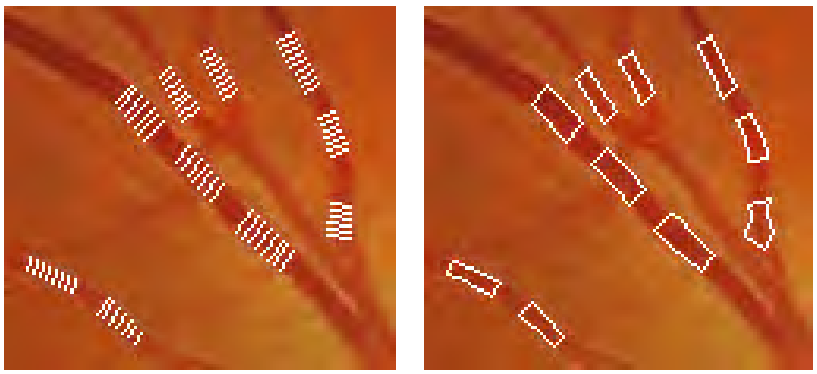

(a) (b)

Figure 3.5: (a) Sample of several profiles extracted from the vessel segments shown in (b).

Several types of color features over different color spaces have been analyzed. We have tested the red (R) and green (G) channels of the RGB color model , the hue component (H) of HSL color space and a gray scale image obtained by means of $I = 0.299R + 0.587G + 0.114B$. We can define three types of features from the vessel segments regarding the involved pixels:

- Features based on the whole vessel segment, e.g. the mean of the vessel segment pixels in a given color component.
- Features based on each profile pixel. We have considered the pixel value in a color component or the combination of pixel values in several color components for all pixels in each profile.
- Features based on groups of pixels. We have considered features based in each profile, such as the mean or the median, or we can select several values to represent the profile, e.g., the n most repeated color values in the profile pixels.

The features based on the whole vessel segments are ruled out due to the variation within a class. Moreover of the features mentioned above, we have analyzed another feature vector proposed by Grisan and Ruggeri [79] which consists of two components, the mean of the H component and the variance of the R component in the profile. The following list summarizes the feature vectors that we have finally used:

- Pixel based features
  - One single value: (R), (G), (H), I
  - Combination of values: (G, R)
- Profile based features
  - One single value:
    - Mean: $(\mu(X))$ where $X \in \{R, G, H, I\}$
    - Median: $(\tilde{\mathrm{x}}(X))$ where $X \in \{R, G, H, I\}$

  - $*$ n most repeated values: (X_1), (X_2) $\ldots$ (X_n) where $X \in \{R, G, H, I\}$
  - $*$ Mean of n most repeated values: (μ(n most repeated values(X)) where $X \in \{R, G, H, I\}$
- Combination of values:
  - $*$ n most repeated values: (G_1, R_1), (G_2, R_2) $\ldots$ (G_n, R_n)
  - $*$ Mean of n most repeated values: $(\mu$(n most repeated values(G)), μ(n most repeated values(R)))
  - $*$ Mean of H and variance of R (Grisan et al.'s features): $(\mu(H), \sigma(R))$

Moreover, since the lack of color constancy influences the classification results, color features extracted from the normalized image obtained by the *Retinex* techniques [84] (Appendix B) are also analyzed. The tests performed using the different features are detailed in the Results (Chapter 6).

In order to group the feature vectors into local subsets, the retina image is divided into four quadrants centered at the optic disc and the *K-means* clustering algorithm is applied to the vessel feature vectors found in that quadrant. The number of clusters used is two, one for veins and another for arteries. The classification results in the four quadrants are stored and the quadrants are rotated an angle $\theta = 20°$. These two steps are repeated from 0° to 180° (Figure 3.6). In this manner, a vessel segment can be classified several times in different quadrants with different neighboring vessel segments. In each quadrant, the K-means algorithm classifies each feature vector into artery or vein. Then, the cluster of the vessel segment is determined by probabilities according to the number of vessel feature vectors labeled in each class. The empirical probability P of the vessel segment, v_j, to be a vein or an artery is computed as follows

$$\begin{aligned} P[v_j \in \text{Artery in } q] &= \frac{n_{a_j}}{n_{a_j} + n_{v_j}} \\ P[v_j \in \text{Vein in } q] &= \frac{n_{v_j}}{n_{a_j} + n_{v_j}} \end{aligned} \tag{3.15}$$

where q is the current quadrant, n_{a_j} and n_{v_j} are the number of feature vectors from the vessel segment j that were classified as artery and vein, respectively.

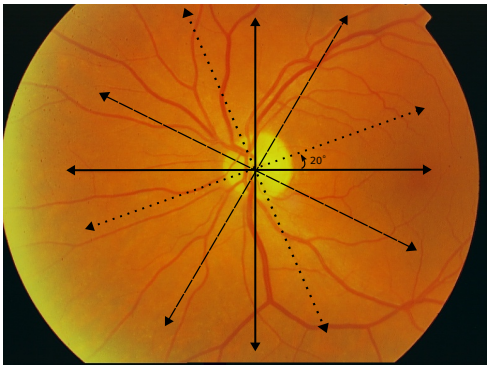

Figure 3.6: Quadrant rotation for local clustering.

Finally, the final artery and vein probabilities are computed as the mean of the probabilities in all the quadrants, m, where the vessel segment was classified. This can be expressed as follows

$$\begin{aligned} P[v_j \in \text{Artery}] &= \sum_{q=1}^{m} P[v_j \in \text{Artery in } q] \\ P[v_j \in \text{Vein}] &= \sum_{q=1}^{m} P[v_j \in \text{Vein in } q] \end{aligned} \tag{3.16}$$

Then, the vessel segment is assigned to the cluster of the highest probability. If both vein and artery probabilities are equal, the vessel segment is not classified.

Vessel tracking

A vessel tracking procedure [89, 85] was developed in order to combine the local classifications obtained for the same retinal vessel in the different circumferences and increase the certainty of the labeling. The algorithm involves to find the minimal path [86] (Appendix C) between the vessel segments in consecutive circumferences given the optic disc center and the middle points of the vessel parallelograms.

The searching of minimal path, $\mathcal{P}min$, between two points, p_0 and p_1, involves the computation of the surface of minimal action, $\mathcal{U}$, between the initial and final point. The minimal action, $\mathcal{U}$ represents the necessary cost to reach one point from the other. After

that, the path of minimal cost is found from the surface $\mathcal{U}$ using gradient descent.

The calculation of the minimal action involves defining the potential, P, that is, the relation between the image features and the cost of the path. In this case, the path between the vessel segments should follow the vessels, so the potential has to be define based on the vascular tree and it should be low inside the vessels. Hence, in order to compute the surface of the minimal action, a vessel tree enhancement is necessary to remove the lightness and tone variability as well as the central reflexes along the vessels. Moreover, in this case, the unique acceptable paths are those that run through the vascular tree, so a vessel tree segmentation is necessary as well.

Vessel tree enhancement First, a morphological 25×25 black-hat top-hat filter is applied in order to reduce the variance of the background and increase the difference between the background and the vessel tree. The result of the top-hat filter is defined by

$$T = G - G \bullet b \tag{3.17}$$

where G represents the G channel of the RGB input image, b is a square structuring element and $\bullet$ represents the closing morphological operation.

Then, the central vessel reflexes are smoothed or removed by a 3×3 median filter. Hence the enhanced image can be defined as follows

$$I_{Enh} = f_{median}(T) \tag{3.18}$$

The enhanced image can be seen in Figure 3.7(b).

Vessel tree segmentation Two alternatives have been considered to segment the retinal vessel tree. The first one is simpler and further but it gets approximate results, whereas, the second one is more precise. The first algorithm determines the likelihood that a vessel is present according to the mean and standard deviation values in a neighborhood, while the second is through Hessian eigenvalues.

First algorithm Each pixel in the enhanced image is considered belonging to the vessel tree if its gray level is darker than the mean computed in a neighborhood centered in the pixel and the standard deviation in the same neighborhood is higher than a threshold. Otherwise, the pixel is marked as background. Formally, this can be expressed by

$$p = (x, y) \in \text{Vessel tree} \Leftrightarrow \begin{cases} G(x, y) < \mu(G(i, j)) \, , (i, j) \in \aleph(\sigma_1) \\ \sigma(G(i, j)) > t_\sigma \, , (i, j) \in \aleph(\sigma_1) \end{cases} \tag{3.19}$$

where G represents the G channel of the RGB input image, $t_\sigma = 3$ is a threshold and $\aleph(\sigma_1)$ represents the neighborhood centered in the point (x, y) with size $\sigma_1 = 11$. As Figure 3.7(c) shows, this algorithm produces a rough segmentation, but it has a really useful property: the segmentation clearly delimits vessel boundaries and fills the intersections between vessels.

Second algorithm This algorithm is based on the approach proposed by Condurache and Ach [90]. In this case, a second enhancement process [91] is applied. This performs a multi-scale analysis of the Hessian eigenvalues to determine the likelihood that a vessel is present. So for each pixel, this measure was calculated at three different scales. After that, a hysteresis thresholding is performed using two thresholds computed by a percentile based rule [91], specifying the percentages of the image surface certainly occupied by background and vessel pixels. After that, a recursive procedure to remove pixels that do not belong to the vessel tree is applied. Finally, the isolated pixels that are not connected to a minimum number of neighbors are marked as background. Figure 3.7(d) shows the output of the vessel tree segmentation using this algorithm. This algorithm reduces the noise, but it has two drawbacks: it is time-consuming and many vessels can disappear if the selected parameters are inadequate.

Initial and final point sets The goal is obtain the minimal path, $\mathcal{P}min$, between the vessel segments in consecutive circumferences. Therefore, in each circumference of analysis with radius r_i, the initial and final points will be the mid-points of the vessel segments at the circumferences r_i and r_{i+1}, respectively. However, it could happen that vessel

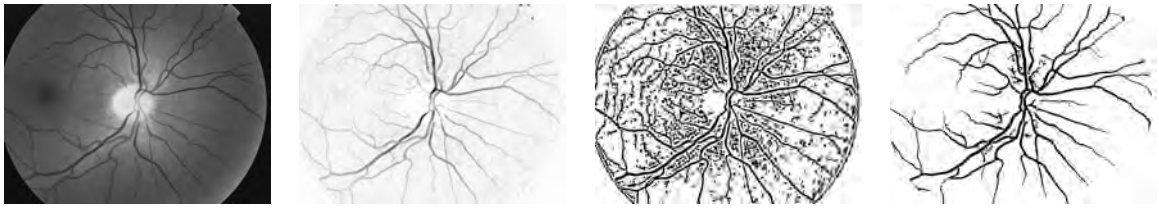

(a) (b) (c) (d)

Figure 3.7: Image enhancement and vessel tree segmentation. (a) Green channel of input image. (b) Enhanced image result of the top-hat and median filter. (c) Vessel tree segmentation with the first algorithm. (d) Vessel tree segmentation using the second algorithm.

segments from the same vessel were not detected in all circumferences. For this reason, auxiliary points are included in the tracking algorithm. These points are the intersection points between a circumference image mask and the segmented vessel tree as shown in the following equation

$$P_{aux} = \{p = (x, y)/I_C(x, y) = 1 \wedge I_{tree}(x, y) = 1\} \tag{3.20}$$

where I_C is the mask of the circumference and I_{tree} is the segmented vessel tree.

In addition, other intermediate vessel points can be included in the tracking in order to improve the performance. Thus, we include the intersections points between the segmented vessel tree and all the circumferences of radius $\frac{r_i+r_{i+1}}{2}$.

Figure 3.8 shows all points taken into account in the algorithm for five initial circumferences.

Minimal path computation The path between the vessel segments should follow the vessels, so the potential has to be define based on the vascular tree and it should be low inside the vessels. Specifically, it should be low in points with similar gray level values to the path starting point. This way, the potential function is defined as

$$P = |I_{Enh} - I_{Enh}(p_0)| + w, \tag{3.21}$$

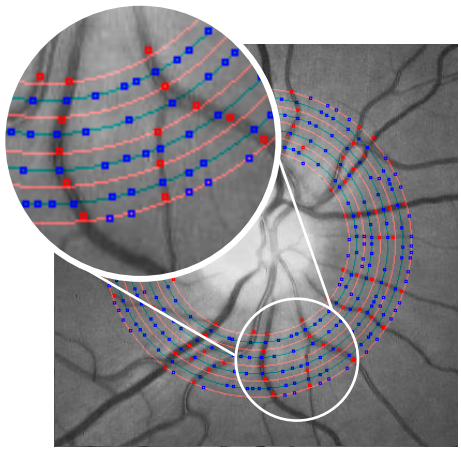

Figure 3.8: Initial and final point sets for the minimal path algorithm. In red, points detected with the snake segmentation algorithm, that is, the mid-points of the vessel segments to track. In blue, points detected by the intersection of each circumference with the vessel tree segmentation. The intermediate circumferences are also shown in blue.

where I_{Enh} is the enhanced image, $I_{Enh}(p_0)$ is the intensity value at the starting point, and w is the regularization parameter. The value of $w = 1$ controls the path roughness, thus, to decrease the path curvature, we have to increase this parameter or smooth the potential image.

Thus, to find the points connected to a starting point, p_0, the front is propagated from the circumference where p_0 is located to the next circumference along the vessel tree, calculating the potential and the surface of minimal action, $\mathcal{U}$, centered on the point. The front starts always at the input vessel segments, that is, the starting point, p_0 can not be an auxiliary point since these points can not belong actually to the vascular tree. As the vessels are propagated from the optic disc outwards, a vessel point cannot be connected to other ones in the same circumference. Therefore, only connections between a point and other points in outermost circumferences are accepted.

The classic minimal path approach presented by Cohen and Kimmel allows the front propagation in any direction. However, in this case, paths which run outside the vessels are not suitable. So, some restrictions are added to the minimal action computation. This way, we allow the propagation over a reached point p_r if it satisfies the following rules

- The point $p_r = (x_r, y_r)$ is marked as part of the vessel tree. That is, $I_{tree}(x_r, y_r) = 1$.
- The point $p_r = (x_r, y_r)$ is placed on the ring delimited by the starting circumference with radius r_s and the candidate circumference with radius r_c. Thus, given c the optic disc center and $dist$ the euclidean distance, this can be expressed by $r_s < dist(p_r, c) < r_c$.

These restrictions make that a point p_0 can only reach points located in the same vessel or in a vessel that crosses it. Since the possible reached points are limited, the surface of minimal action $\mathcal{U}$ for a point p_0 can be calculated in a small window centered on it (Figure 3.8). The window size depends on the gap between the circumference that contains p_0 and the candidate circumference. Specifically, if this gap value is g, the window size is $g + 2n + 1$, where $2n + 1$ is the maximum length of the centerline segments considered as snake seeds. This ensures that potential candidate points are within the window and can be reached by the front since the final vessel midpoints can not over the circumference due to snake deformation.

Figure 3.9 shows three potential images for different starting points and the corresponding surfaces of minimal action whose intensity values represent the minimal cost necessary to reach each point from the starting point. Note, in some cases, the points are not exactly over the circumference because the deformation process of the snakes can move its center.

In the propagation from a point p_0, the front can reach vessel points in the same circumference (conflicting points), $\mathcal{C}onf_{p_0}$ or in the next circumference (candidate points), $\mathcal{C}and_{p_0}$. When the front propagation stops and the surface of minimal action was computed, three situations can occur

1. No conflicting points were found (Figure 3.9 first row). In this case, there can be several candidate points, but it does not imply that every candidate point should be linked with p_0 because some candidates can be noise or belong to another close vessel. However, points that belong to the same vessel have the same intensity. So, a threshold value, t_c, for the candidates' cost is taken into account. Then, the

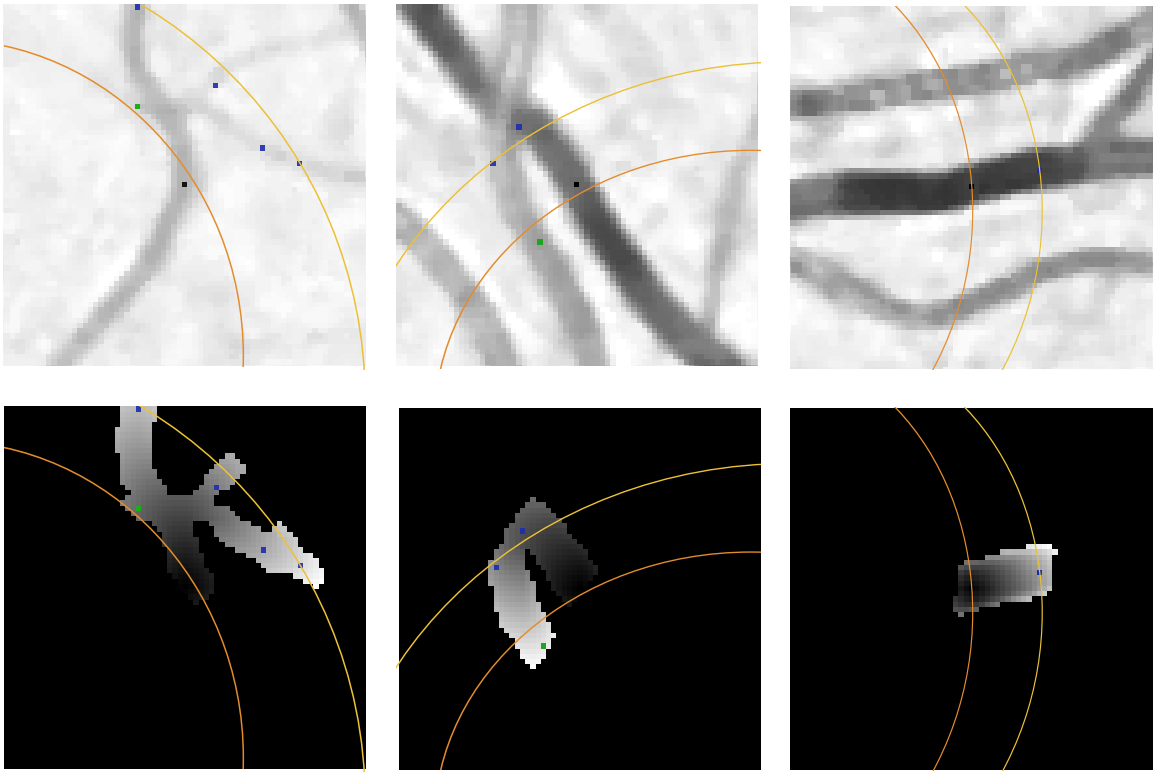

Figure 3.9: The first row shows some potential images computed in small windows centered at the starting point p_0, and, the second row, the corresponding surfaces of minimal action $\mathcal{U}$ between the starting point and the candidate points in the candidate circumference. The starting and candidate circumferences have been superimposed in orange and yellow, respectively, as well as, the initial point, p_0, in black, the candidate points in blue and the conflicting points in green.

candidate point with the lowest cost is selected and the other candidate points with a cost higher than β times the lowest cost are discarded. All the remaining candidate points are included in the list of points connected to the starting point p_0, $\mathcal{L}_{p_0}$. This can be expressed as follows

$$p_1 \in \mathcal{L}_{p_0} \Leftrightarrow \mathcal{U}(x_1, y_1) \leq t_c = \beta \cdot min\{\mathcal{U}(x_i, y_i),\ (x_i, y_i) \in \mathcal{C}and_{p_0}\} \tag{3.22}$$

where $p_1 = (x_1, y_1) \in \mathcal{C}and_{p_0}$.

2. There are several conflicting points and a single candidate point (Figure 3.10, second row). There are two subcases. This case is equal to the previous one when the conflicting points and p_0 have been reached by the propagation of the same starting point of a previous circumference (Figure 3.10 (e)). Otherwise, we discard the candidate point since it is over a vessel intersection and different vessels could be merged. In this case, we propagate the front to the next circumference and we repeat the point analysis. For example, in Figure 3.10(f), we can see a candidate point (p_1) with a starting point (p_0) and a conflicting point (p_2). Clearly, point p_1 may be linked with point p_0, but, since it is over an intersection, there is a high probability of errors. We remove the point p_1 and we propagate the solution from p_0 to the next circumference.

3. There are conflicting points and several candidate points (Figure 3.10, third row). This means that either there is an intersection between the circumferences (Figure 3.10(g)) or there are some noise points due to the vessel tree segmentation (Figs. 3.10(h) and 3.10(i)). In both cases, new fronts from the conflicting points to the candidate points are propagated in order to check if the candidate points are connected actually to the starting point p_0 or, conversely they can be connected to the conflicting points. Each candidate point, $p1 = (x_1, y_1) \in \mathcal{C}and_{p_0}$, is included in the list of points connected to p_0, $\mathcal{L}_{p_0}$, if it fulfills one of the next requirements for each conflicting point p_3

   - The cost from the conflicting point to the candidate point is higher than the threshold t_c

$$\mathcal{U}_{p_3}(x_1, y_1) > t_c \Rightarrow p_1 \in \mathcal{L}_{p_0} \tag{3.23}$$

where $\mathcal{U}_{p_3}$ is the surface of minimal action of the conflicting point p_3 and $t_c = \beta \cdot min\{\mathcal{U}_{p_0}(x_i, y_i),\ (x_i, y_i) \in \mathcal{C}and_{p_0}\}$.

- The costs are similar but the path curvature between the starting point is lower than the obtained with the conflicting point

$$\left.\begin{array}{c} \mathcal{U}_{p_3}(x_1, y_1)\beta > \mathcal{U}_{p_0}(x_1, y_1) \\ \wedge \\ \kappa(\mathcal{P}min_{p_0 \to p_1}) < \kappa(\mathcal{P}min_{p_3 \to p_1}) \end{array}\right\} \Rightarrow p_1 \in \mathcal{L}_{p_0} \tag{3.24}$$

  where $\mathcal{U}_{p_0}$ is the surface of the minimal action of the starting point p_0, κ represents the curvature whereas $\mathcal{P}min_{p_0 \to p_1}$ and $\mathcal{P}min_{p_3 \to p_1}$ are the minimal paths from the starting and conflicting point to the candidate point.

  Otherwise, the candidate point is not considered to be in the same vessel than the starting point. Probably it belongs to the same vessel as the conflicting point. After checking these cases, we also discard the candidate points which are far from the lowest cost, applying the threshold t_c. All the remaining points are linked to p_0. In Figure 3.10(g), point p_0 is linked with point p_1. Since vessel intensities are similar, we obtain the path curvature between (p_0, p_1), (p_0, p_2), (p_3, p_1) and (p_3, p_2). Obviously, the (p_0, p_1) curvature is lower than (p_3, p_1) curvature so the candidate point p_1 is connected to the starting point p_0.

The front propagation is repeated between two consecutive circumferences, from the optic disc outwards. Finally, the minimal paths are computed by the gradient descent from the outer to the inner circumferences. Thus, at each step, the point with the lowest cost in a four neighborhood within the surface of minimal action is included in the minimal path. This is repeated until achieving the global minimum, that is, the starting point where the cost is 1. If we reach a local minimum, this is not included in the minimal path and the search for the lowest cost point is performed backward. Thus, a point p_m is included in the minimal path to a starting point if it fulfill the next equation

$$p_m \in \mathcal{P}min \Leftrightarrow \left\{\begin{array}{ll} \mathcal{U}(x_m, y_m) < \mathcal{U}(x_i, y_i), & (x_i, y_i) \in \aleph_{(x_{m-1}, y_{m-1})}(4) \\ \mathcal{U}(x_m, y_m) > \mathcal{U}(x_i, y_i), & (x_i, y_i) \in \aleph_{(x_m, y_m)}(4) \end{array}\right. \tag{3.25}$$

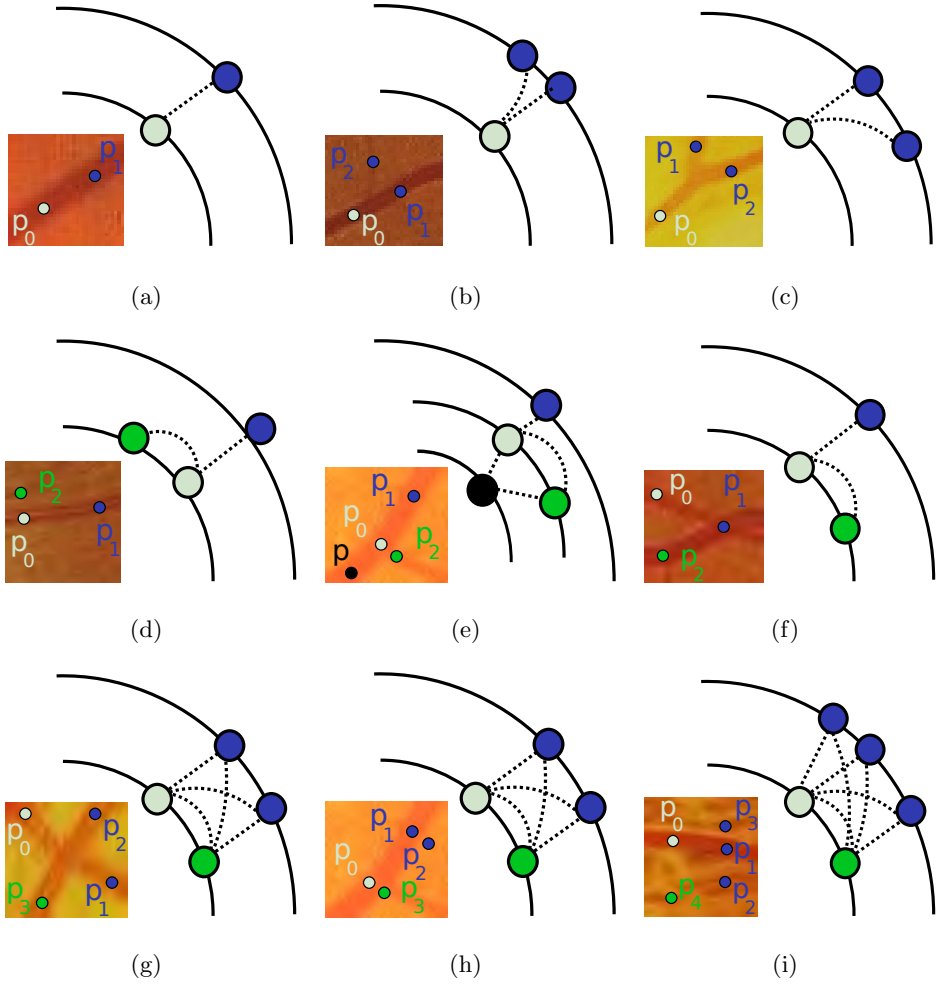

Figure 3.10: Propagation cases. First row: only candidate points; (a) a single candidate; (b) two candidates, one could be noise; (c) two candidates in a branch. Second row: only one candidate point and several conflicting points; (d) the conflicting point is noise, (e) the conflicting and starting point have been reached by the propagation of the same point p in a previous circumference; (f) the candidate point is over a crossing. Third row: several candidates and conflicting points; (g) there is a crossing between the circumferences; (h) and (i) no crossings, only noise or points in the same vessel.

where $p_m = (x_m, y_m)$ and $\aleph_{(x_{m-1},y_{m-1})}(4)$ and $\aleph_{(x_m,y_m)}(4)$ are the four neighborhood centered in the previous minimal path point $p_{m-1} = (x_{m-1}, y_{m-1})$ and in the current point $p_m = (x_m, y_m)$, respectively

Once we have obtained the list of connected vessel segments, a voting strategy decides the final category of each vessel, assigning the most voted label to the entire vessel. If a vessel contains the same number of vein and artery vessel segments, all its segments will not be classified.

Chapter 4

AVR computation

This chapter is focused on the *arteriovenous ratio* (AVR) computation. Its purposes are, first, to summarize the different methodologies presented in the literature to estimate the AVR, and second, to explain how the AVR is computed and integrated in our methodology.

Different formulas to estimate the AVR have been proposed in the literature: the Parr-Hubbard procedure [92, 2] and the revised Knudtson-Parr-Hubbard formula [4] who estimate the AVR as the quotient of the Central Retinal Artery and Vein Equivalents, as well as, the method of the quotient between the averages of artery and vein widths [93, 3]. The main problem in the AVR computation using these procedures is the lack of repeatability since each time it is computed from a patient's image, a different set of vessels, measured at different points is used. Thus, in this chapter, we propose to use a vessel registration procedure between different patient's images acquired from the same eye, in order to use the same set of vessels in all AVR measurements.

The chapter is structured as follows. The first section provides a brief review of the different approaches proposed in the literature to compute the AVR. The next section explains the procedure used in this methodology to select a suitable set of vessels to compute the AVR automatically in a sample patient's image. Finally, the last section describes the system to monitor the patient's AVR over time using the same set of vessels for the AVR calculus in all patient's images.

4.1 Introduction

The AVR is computed as the ratio between artery and vein widths measured in several circumferences centered at the optic disc. It was proposed by Stokoe and Turner in 1966 [1] as an average of width ratios between comparable pairs of arteries and veins. In the literature, several methods have been proposed to estimate this measure. In most of the approaches, the AVR is calculated in the region between the circumferences with radii $2r$ and $3r$, with r the optic disc radius [2, 4, 94, 95], in this manner, many crossovers between vessels are avoided. Although, in Hubbard et al. [2], the experts can move outside this region in order to measure the branches of an artery. On the contrary, Benavent et al. [96] considered the region between $1r$ and $3r$ and Pose et al. [3] take into account a region from $2r$ outwards.

Regarding the number of times which a vessel width is included in the AVR computation, there are also differences between authors. It seems that the manual method proposed by Hubbard et al. [2] takes into account only a measurement for each vessel found in the region $2r-3r$, except for arteries whose width is equal or greater than 80μm, in which case, the grader measures the artery branch segments as well. On the contrary, Benavent et al. [96] take three measurements in each vessel corresponding with the intersections between the vessels and the circumferences of analysis with radii $1r$, $2r$ and $3r$. Also, Pose et al. [3] consider several measurements for the same vessel over the analysis radii. All segments found in the tracking process from $2r$ to $3r$ are measured in the Li et al.'s approach [94], whereas, Niemeijer et al. [95] calculate an AVR in each analysis radius and after that they compute the final AVR as the average of these values.

Regarding the formulas used to estimate the AVR, there are also differences between the approaches found in the literature. In [93, 3], the AVR is computed as the quotient between the averages of arteriolar and venular widths as Equation 4.1 shows.

$$AVR = \frac{\sum_{i=1}^{n_{\mathcal{A}}} \omega_i / n_{\mathcal{A}}}{\sum_{j=1}^{n_{\mathcal{V}}} \omega_j / n_{\mathcal{V}}} \tag{4.1}$$

where $n_{\mathcal{A}}$ and $n_{\mathcal{V}}$ are the number of arteries and veins, and ω_i and ω_j represents an artery and vein width, respectively.

Parr and Spears [97, 92] and, subsequently Hubbard et al. [2] derived formulas widely used in popular studies [18] and in other methods for the AVR calculus [94, 95]. In these methods, the AVR is computed as the quotient of two variables, the *Central Retinal Artery Equivalent* (CRAE) and the *Central Retinal Vein Equivalent* (CRVE) as follows

$$AVR = \frac{CRAE}{CRVE} \tag{4.2}$$

The CRAE and CRVE equivalents represent the relation among a vessel trunk and its two branches. However, they are computed iteratively using all vessels without differentiating trunks from branches as Algorithm 3 summarizes. At each step of the algorithm, the smallest, $\omega_{\mathcal{A}s}$, $\omega_{\mathcal{V}s}$, and biggest, $\omega_{\mathcal{A}b}$, $\omega_{\mathcal{V}b}$, arteriolar and venular widths are replaced by the corresponding Parr-Hubbard's formulas shown below

$$\begin{aligned} \omega_{\mathcal{A}} &= \sqrt{0.87\omega_{\mathcal{A}s}^2 + 1.01\omega_{\mathcal{A}b}^2 - 0.22w_{\mathcal{A}s}\omega_{\mathcal{A}b} - 10.76} \\ \omega_{\mathcal{V}} &= \sqrt{0.72\omega_{\mathcal{V}s}^2 + 0.91\omega_{\mathcal{V}b}^2 + 450.05} \end{aligned} \tag{4.3}$$

The previous formulas to estimate the equivalents have been derived theoretically and empirically, observing a fixed data set, and some reformulations have been introduced. In fact, Knudtson et al. [4] realized that the Hubbard's formulas were dependent on the number of selected vessels and they propounded the following reformulation using only the six main arteries and veins.

$$\begin{aligned} \omega_{\mathcal{A}} &= \sqrt{0.88(\omega_{\mathcal{A}s}^2\omega_{\mathcal{A}b}^2)} \\ \omega_{\mathcal{V}} &= \sqrt{0.95(\omega_{\mathcal{V}s}^2 + \omega_{\mathcal{V}b}^2)} \end{aligned} \tag{4.4}$$

Recently, Patton et al. [98] proposed a revised CRAE formula, where the branching coefficient, BC, is not a constant as in the Knudtson's formula but a linear function dependent on the asymmetry index, AI, $BC = 0.78 + 0.63 * AI$, where the asymmetry index is the quotient between the width of the two branches.

Algorithm 3 Algorithm for CRAE and CRVE computations

Definitions:

- $\mathcal{A}$ set: list of arteriolar vessel widths
- $\mathcal{V}$ set: list of venular vessel widths
- $CRAE$: Central Retinal Artery Equivalent
- $CRVE$: Central Retinal Vein Equivalent

Initialization:

- Convert $\mathcal{A}$ and $\mathcal{V}$ to microns in case of using Parr-Hubbard's formulas

Loop:

- Remove from $\mathcal{A}$ the smallest, $\omega_{\mathcal{A}s}$, and biggest, $\omega_{\mathcal{A}b}$, arteriolar widths
- Remove from $\mathcal{V}$ the smallest, $\omega_{\mathcal{V}s}$, and biggest, $\omega_{\mathcal{V}b}$, venular widths
- Compute the new arteriolar width, $\omega_{\mathcal{A}}$, using $\omega_{\mathcal{A}s}$ and $\omega_{\mathcal{A}b}$ in the corresponding formula of Equations 4.3 or 4.4
- Insert $\omega_{\mathcal{A}}$ in $\mathcal{A}$
- Compute the new venular width, $\omega_{\mathcal{V}}$, using $\omega_{\mathcal{V}s}$ and $\omega_{\mathcal{V}b}$ in the corresponding formula of Equations 4.3 or 4.4
- Insert $\omega_{\mathcal{V}}$ in $\mathcal{V}$

Output:

- Set $CRAE$ to be the last width in $\mathcal{A}$
- Set $CRVE$ to be the last width in $\mathcal{V}$

4.2 Vessel selection for AVR computation

Once the optic disc was located and the vessel segments were measured and classified, the last step consists on selecting a suitable set of vessels to use in AVR computation.

In a semiautomatic procedure for the AVR computation [99, 100], once the medical expert had classified the vessels into arteries and veins, the AVR is computed as the quotient between the averages of the artery and vein widths selected by the expert. However, the medical experts do not classify all the detected vessels but only a subset of them. They follow some unwritten rules to select the most suitable vessels and, although two experts do not select exactly the same subset, the correlation between them is high [100]. For this reason, in [101] we analyzed the set of vessels selected by two medical experts in a large image data set trying to emulate the selection made by them. As a result, the following set of hypothesis about the selection rules used by experts has been derived

- H1: Experts rule out the vessels whose width has been over- or sub-estimated.
- H2: Experts do not take into account vessel segments found over a bifurcation or a crossover.
- H3: Experts do not select the same number of arteries and veins at each analysis radius.
- H4: Experts select the same global number of arteries and veins.
- H5: Experts do not take into account thin vessels, either because it is more difficult to know their classes or because it is more probable to overestimate their width.
- H6: Experts rule out false positive vessels detected in the background.

Taking into account the hypothesis cited above, an algorithm for the vessel selection has been implemented as follows:

- The H1 hypothesis has been implemented taking into account the result of the vessel tracking algorithm used in the classification stage, that is, the sets of connected vessel

segments which belong to the same retinal vessel. Thus, a vessel segment is over- or sub-estimated and therefore it is ruled out if its width is larger than the double or smaller than the half the median width of its list of connected segments which it belongs to. This can be formulated as follows.

$$\left(\hat{\omega}_{v_i} < \frac{1}{2}\tilde{x}(\Omega)\right) \vee (\hat{\omega}_{v_i} > 2\tilde{x}(\Omega)) \Rightarrow v_i \text{ is ruled out} \tag{4.5}$$

where $\hat{\omega}_{v_i}$ is the width of the vessel segment v_i, Ω represents the widths in a set of connected vessels segments and $\tilde{x}$ represents the median.

In addition, these extreme vessels can be also detected by means of percentiles, discarding the vessels whose widths are less than the p percentile or larger than the 100-p percentile.

- A method which detects bifurcation and crossovers [102] has been applied to implement the H2 hypothesis. In this case, we have two alternatives, since the vessel segments over a crossover or bifurcation can be discarded before or after the classification procedure. Removing them before the classification can be an advantage in case of crossovers because the snake parallelogram embraces the two vessels of different type and the classification can be altered with feature vectors which include color information of both classes, arteries and veins.

  Given p a crossover or bifurcation point and v_i the vessel segment whose snake parallelogram is delimited by the vertex points (u_1, u_2, u_3, u_4), the vessel v_i is ruled out if the parallelogram contains the point p. This was implemented as follows

$$\sum_{i=1}^{3} angle((p, u_i), (p, u_{i+1})) > 360^\circ \quad \Rightarrow v_i \text{ is ruled out} \tag{4.6}$$

  where (p, u_i) denotes the vector formed by the point p and the vertex u_i.

- Hypothesis H3 and H4 were carried out excluding, iteratively, the smallest arteries and veins while the number of vessel segments in both classes is distinct globally, or in each circumference, respectively.

- Hypothesis H5 is implemented by three different ways. On one hand, thin vessels are detected by percentiles, ruling out those segments whose width is smaller than

p percentile. In the first manner, a single percentile is computed for both classes, whereas, in the second, a percentile for veins, and another for arteries are calculated. The values p=5 and p=10 were used. On the other hand, thin vessels are discarded when more restrictive parameters in the MLSEC-ST operator are used.

- For the H6 hypothesis, we have also two possible implementations. The first one consists on using the vessel tracking output to remove all the isolated vessel segments which are not connected to any other. The second way to reduce the number of false positives implies the use of more restrictive MLSEC-ST parameters.

In addition, according to some authors, we try another selection method which just consists on taking into account the six main arteries and six main veins to estimate the AVR. In this case, we only consider the 12 main vessels with the largest median width along the vessel.

After the vessel selection, the AVR is computed applying the appropriate formulas.

4.3 AVR monitoring system

The main problem of the previous proposal is the high dependency of the AVR value on the selected set of vessels and the area where they are measured. We showed this influence in [101] when the AVR is computed as an average width ratio. The same problem occurs with the Parr-Hubbard's formulas. In fact, Knudtson et al. proposed a revision of these due to their dependency on the vessels. The same issue could happen using the Knudtson's formulas when, for example, it is not possible the detection of six veins or arteries in the image or the measurement area varies significantly between different patient's images. In addition, in many cases the AVR values estimated by an expert and an automatic system are similar in average but the correlation is not so high, even, when the correlation was calculated between the AVR values achieved by medical experts using semiautomatic tools [95, 101]. Thus, reliable AVR computations should involve the measurement of the same set of vessels at the same points for each patient's eye.

In [103], we propose an AVR monitoring system to compute the patient's AVR over time by means of a two-stage methodology. The end of this method is to provide a reliable and repeatable way to calculate the AVR not influenced by the set of selected vessels.

The methodology consists on computing automatically the AVR in a new sample patient's image acquired at time t_i from a stored AVR result. This reference value was calculated in a sample image of the same patient's eye acquired at time t_0, the so-called reference image.

The reference AVR is computed by means of the methodology proposed in the previous section, being the output supervised by an user. Figure 4.1 shows a schema of the monitoring process.

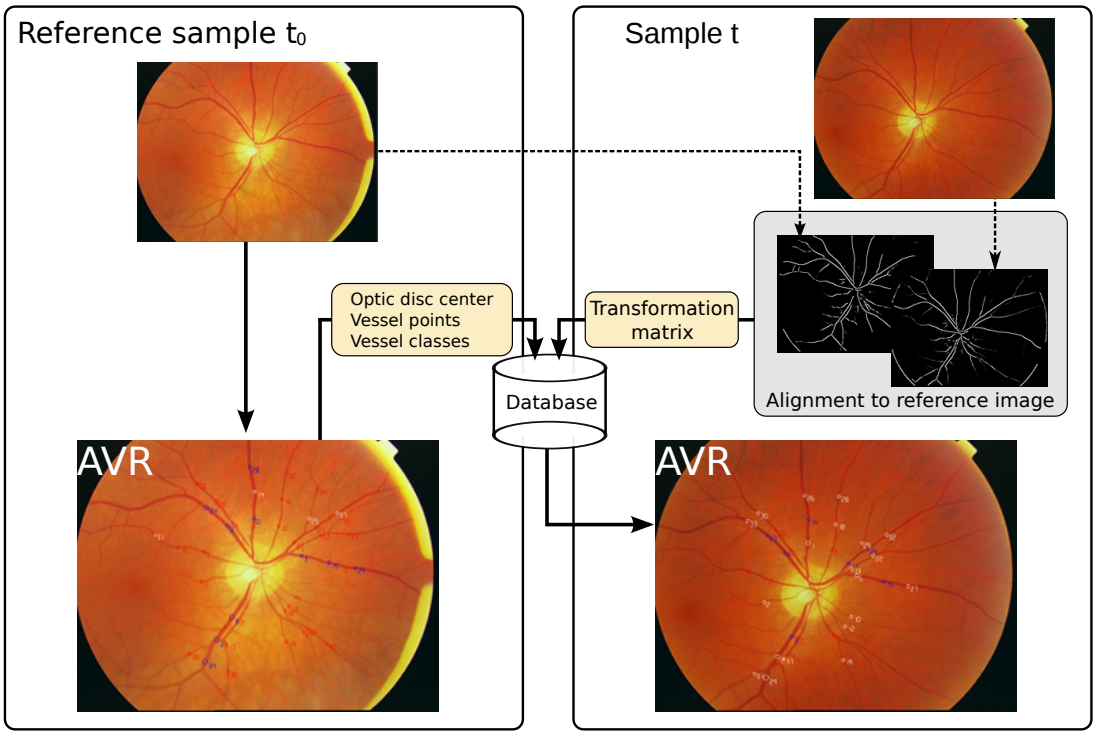

Figure 4.1: Schema of the AVR monitoring process

The method to estimate the non reference AVR results is based on a vessel registration approach since it allows to measure the vessel widths at the same points from different sample images taken at different dates. Thus, the new AVR results are computed by registering the vessel segments used in the reference AVR. To this end, some useful data

must be stored after any AVR calculus, in particular, the optic disc center, the class of each vessel segment and the intersection points between each analysis circumference and the vessel centerlines, that is, the middle points of the snake centerline seeds.

Thus, in the first step of the vessel registration, the new image is registered to the reference image by means of crease alignment (Appendix D). Once a suitable transformation matrix, τ, between the two images has been obtained and the transformation quality has been proved, we can measure the vessel widths in the new image at the same points considered in the reference image. To this end, first, the stored reference optic disc and intersection points are transformed into the new sample image (Figure 4.2). For each transformed intersection point, p_t, we determine the centerline vessel segment centered in p_t by the crease tracking algorithm described in the Chapter 2. To this end, the euclidean distance, d, from the point p_t to the transformed optic disc center is calculated. And, then, taking d as analysis radius, and the crease image previously computed to make the registration, the crease tracking is performed in $2n+1$ circumferences in the interval $[d-n, d+n]$. $n = 10$ was used like in the reference AVR computation.

Once obtained the centerline vessel segment, the vessel segment width can be measured by a snake, following the procedure explained in the Chapter 3.

The vessel classification is obtained from the corresponding vessel segment in the reference image. Finally, the AVR is computed as the ratio between the average artery and vein vessel widths.

Note that, we use the middle point of the snake initialization for the vessel registration and not the middle point in the final snake configuration. This is due to the fact that the middle point of the final snake could be slightly displaced from the initial position because of its deformation. If the snakes evolve from the same starting points in both images, there is a higher probability of similar deformations and, as a consequence, a measurement exactly in the same area.

Thus, the AVR computed in this way is not influenced by set of vessels and the area where they were measured, providing a reliable monitoring system of the patient's AVR

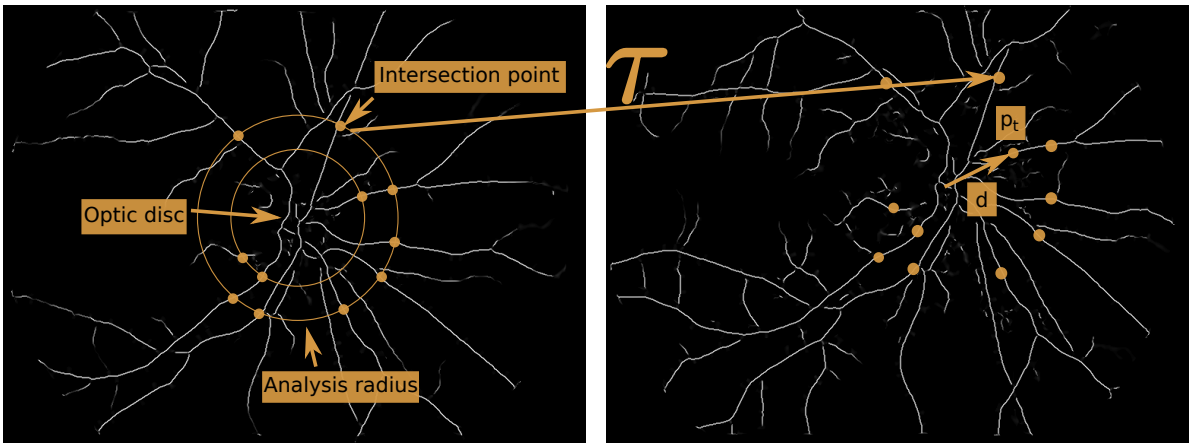

Figure 4.2: Schema of the vessel registration procedure. In the new image (right), the vessel widths are measured at the intersection points registered from the reference image (left). Note that the same set of vessel segments is used to estimate the AVR.

over time.

Chapter 5

SIRIUS web application

This chapter is devoted to explain the SIRIUS (System for the Integration of Retinal Images Understanding Services) system for retinal image analysis. SIRIUS is a web application designed to join several services in the field of retinal image processing [99]. Among these services are the detection of red dots, the semiautomatic computation of the AVR or the vessel tortuosity measurement. Moreover, the system includes user and patient management. Additional services have been included on SIRIUS as well as more patient's information related to pathologies such as, hypertension and diabetes or the automatic computation of the AVR.

In this chapter, we will give an overview of the system, its architecture and the implementation details focusing on the use cases related to the AVR computation services.

5.1 Introduction

Fundamentally, SIRIUS appeared as a tool for physicians and researchers to study the relation between signs in the retina with different pathologies and their evolution after a specific treatment. To this end, it is not enough analyze only the evolution of the retina signs but also much more patient's information, such as, habits, many laboratory test results and medical findings in different screening visits. Thus, these diagnostic or

research studies require assess large amount of data from many patients generated in different health care centers. In addition, collaborations between centers are established, overall in research studies.

Hence, the main objectives of the SIRIUS system are, firstly, to provide physicians and researchers from different locations or medical health centers, a collaborative environment which makes the patient and retinal image management easier. Second, the system have to supply fast and reliable semi or automatic procedures to analyze different variables or features in the field of retina imaging.

5.1.1 Similar applications

The use of telecommunication and information technologies in the clinical health care at distance is known as telemedicine. Telemedicine systems offer to physicians and patients an environment to store, transfer and share clinical data. Moreover, these services are improved when the distribution of the information is done in a standard manner through the Web.

Handels et al. [104] presented KAMEDIN, a telemedicine system to exchange, share and analyze remotely digital images in radiology. Magrabi et al. [105] proposed WebECG, a web-based service to collect, analyze and store a longitudinal ECG record from the patient's home. Lundberg et al. [106] demonstrated that telemedicine systems can be useful in studies of the tympanic membrane by evaluating the agreement between different graders assessing inflammatory disease in endoscopy images. Azar et al. [107] presented a telemedicine web system which allow diabetic patients communicate their blood glucose levels via glucometer uploads and receive the medication adjustments from the caregivers. Mahmoudi et al. [108] presented a web-based system to visualize and process 2D/3D medical images. A wide variety of general preprocessing, segmentation and registration algorithms from ITK library are available for the users via ASP.Net and AJAX. Other recent work is the biomedical image-mining framework proposed by Goudas et al. [109] which allow defining dynamic workflows for image processing and analysis. In the work,

the system was applied to the classification of microscopic kidney biopsies.

Regarding content-based image retrieval (CBIR), many specific systems for medical applications have appeared, since global image descriptors of color, texture and shape are insufficient to characterize and annote medical images. Among those, [110] presented SPIRS (Spine Pathology & Image Retrieval System) which allows explore large databases of spine X-ray and uterine cervix images by textual and visual queries. The Assert system [111] classifies high resolution tomographies of the lung. IRMA system [112, 113] which classifies varied medical images regardless of anatomical area, image modality, body orientation, and biological system. In [114] there is a review of these systems.

Regarding retinal analysis, except the recent works of Yaqin et al. [115] and Tramontan et al. [116], no telemedicine systems have been proposed. The first one is TRIAD, a telemedical system for diagnosis diabetic retinopathy. It focuses on the detection of two major lesions associated with DR: microaneurysms and exudates in retinal images and compare the detected features with past diagnosed images through a CBIR engine. The second one is AVRnet, a web application which computes the AVR automatically for a loaded image, however it do not include a patient's data management. Nevertheless, many standalone applications have been developed lately for assessment of retinal vessels in a semiautomatic way. Examples of these tools are IVAN [2], RISA [117], ROPtool [118], IDx [119], CAIAR [120], ROPnet [121] or VAMPIRE [122]. In addition, SIVA [18] includes automatic retinal vasculature tracing, vessel classification, and optic disc detection.

5.2 Analysis

The most important goal of the system is provide a collaborative environment among different medical centers. To this end, the system was designed as a web application employing an client-server architecture as Figure 5.1 shows.

A three-tier architecture is proposed in order to make the business logic independent of the client and make easier its integration on other clients than browsers in the future.

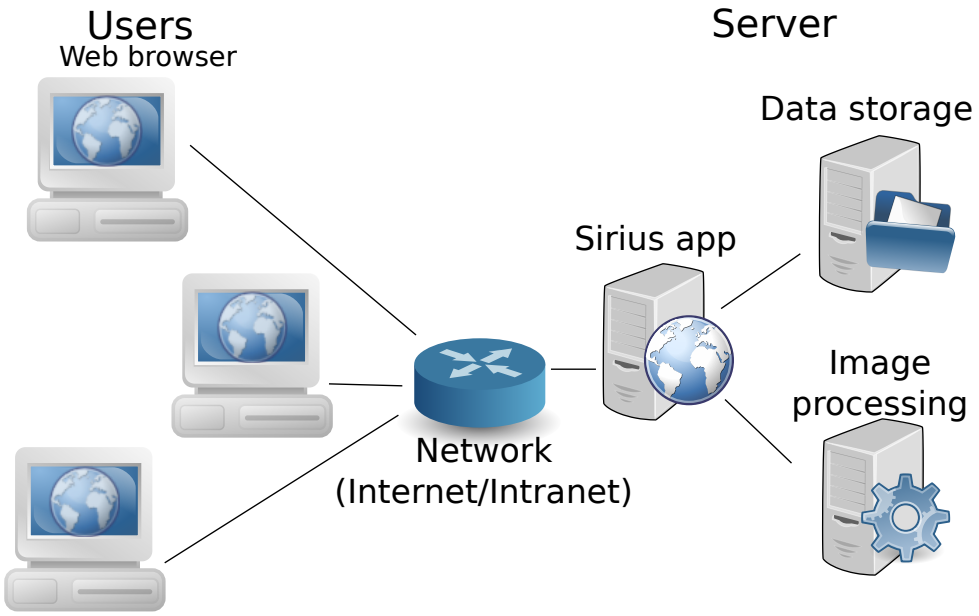

Figure 5.1: SIRIUS client-server architecture.

- *Tier 1: Data Access Layer.* It is the layer which controls the data access, it handles the requests and the responses.
- *Tier 2: Application Layer.* It is where the business logic lives. This layer is subdivided into the following sub-layers:
  - *Image Service Layer.* It encloses all parts of the logic related to the image processing and analysis. This layer do not query the data, it just processes the given data and returns results.
  - *Business Layer.* The remaining business logic lives here, including the queries for the data.
  - *Facade Layer.* It constitutes the interconnection layer between the Application Layer and the Presentation Layer. It provides a simple interface to make the presentation independent of the business logic.
- *Tier 3: Presentation Layer.* This layer is the responsible of presenting the data in a format readable by the client, in this case, HTML.

Three different actors or roles can interact with the system:

- *Doctor.* He/She is a regular user which represents a physician in a specific medical center. The actions or use cases which can be performed by this user are related to the management of his/her patients, and the analysis of their retinal images. Some of the most important actions are the following:
  - **Patient management:** Create, Read, Update and Delete (CRUD) actions for patients, their checkups and the retinal images acquired in a specific checkup. Other examples are: View a patient report or Export a patient report to Excel.
  - **Image analysis:** Compute the AVR, Modify/Save AVR result, Monitor AVR from a template result.
- *Supervisor.* He/She is a special doctor which can view the patients of other doctors, supervise the AVR results computed by these doctors and obtain new AVR results for these patients. But, he/she can have also his/her own patients. His/Her use cases are the cited above but for his/her patients and for other doctor's patients.
- *Administrator or superuser.* He/She is the administrator of the application who is the responsible of management of medical centers and users. The main use cases are the following:
  - **Center management:** (CRUD) actions for centers.
  - **User management:** (CRUD) actions for users.

Figure 5.2 shows a diagram with some of the most important use cases cited above.

5.3 Design

The system has been designed according to the *Model-View-Controller* (MVC) architectural pattern which allow to decouple the presentation or graphic interface (View) from the business logic (Model) through a Controller. Moreover, each of these parts is structured as well in layers using the architectural pattern *Layers* to hide the technology used on each one from the others. The View is the Presentation Layer cited in the analysis,

whereas the Model corresponds to the Application Layer which implements the entire business logic of the SIRIUS system.

In order to store and manage the data, we use a relational database. In Figure 5.2 the entity-relationship model is shown.

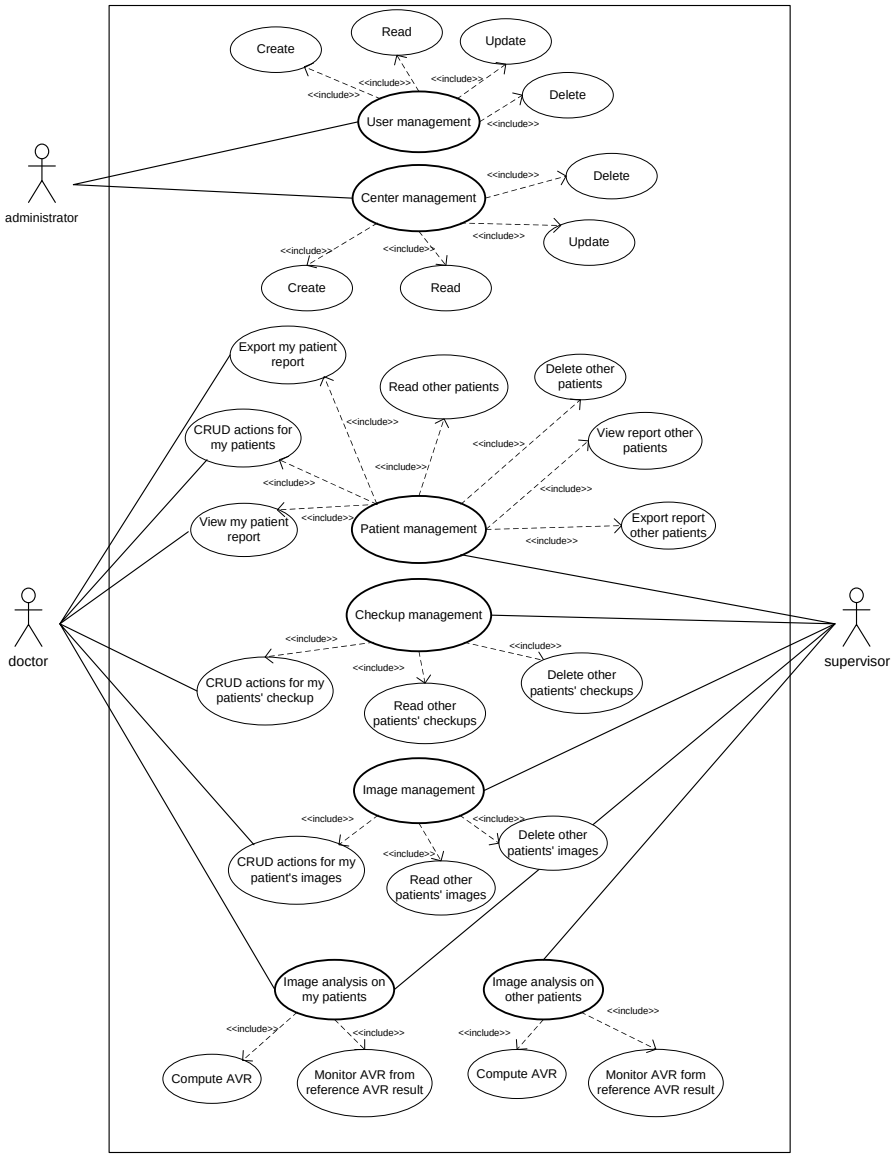

Figure 5.2: Diagram of the main use cases.

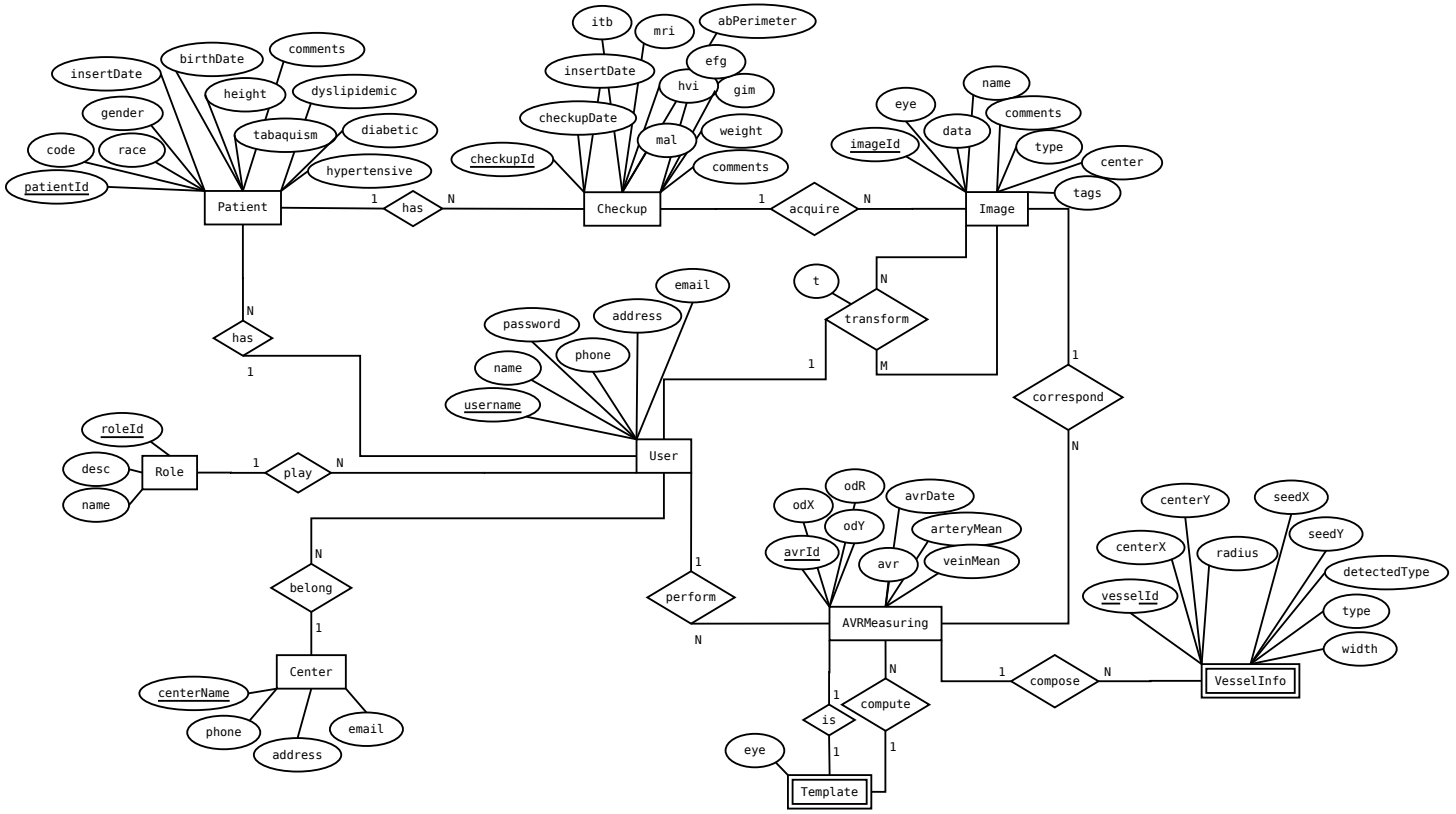

Figure 5.3: Schema entity-relationship.

Each entity mapped to a database table corresponds to an object which implements the *Transfer Object* (TO) or *Data Transfer Object* design pattern. Thus, the transfer of messages intra and inter layers is minimized since this pattern groups several attributes or fields belonging to one o several tables in a unique object. Moreover, to encapsulate the data access making the rest of the application independent on it, and to provide a uniform interface for different data sources, the design pattern *Data Access Object* (DAO) was used. Hence, each TO has the corresponding DAO which implements the data access. As several DAO can coexist to implement different data sources, the pattern *Abstract Factory* is used to select the appropriate DAO as Figure 5.4 shows.

To provide to the presentation layer a simple and unified interface, we use the pattern *Facade*. Each method of this object includes the workflow between DAOs to implement an use case. To hide the technology of the model, the Facade implements, in addition, the pattern *Business Delegate*. Figure 5.5 shows an example of the Facade. As in the DAO pattern case, an Abstract Factory is used to implement the appropriate facade. In order to visualize the results (list of patients, checkups or images) by blocks, the design pattern *Page by Page Iterator* is used.

5.4 Implementation

The implementation of the system is performed using two different programming languages. Thus, the image service layer was implemented in GNU C++, whereas the remaining layers corresponding to the web application itself were implemented in JAVA, specifically the J2EE API was used. This choice is due to C++ is faster and there are several efficient libraries for image processing such as Opencv which was the library used to implement the image service layer. Whereas, the existence of many web servers, frameworks and libraries makes JAVA more appropriate for the web development.

The integration between the two heterogeneous parts is performed by the XML-RPC protocol. The main advantage of this technology compared to others such as Common Object Request Broker Architecture (CORBA) is the simplicity of implementation. In

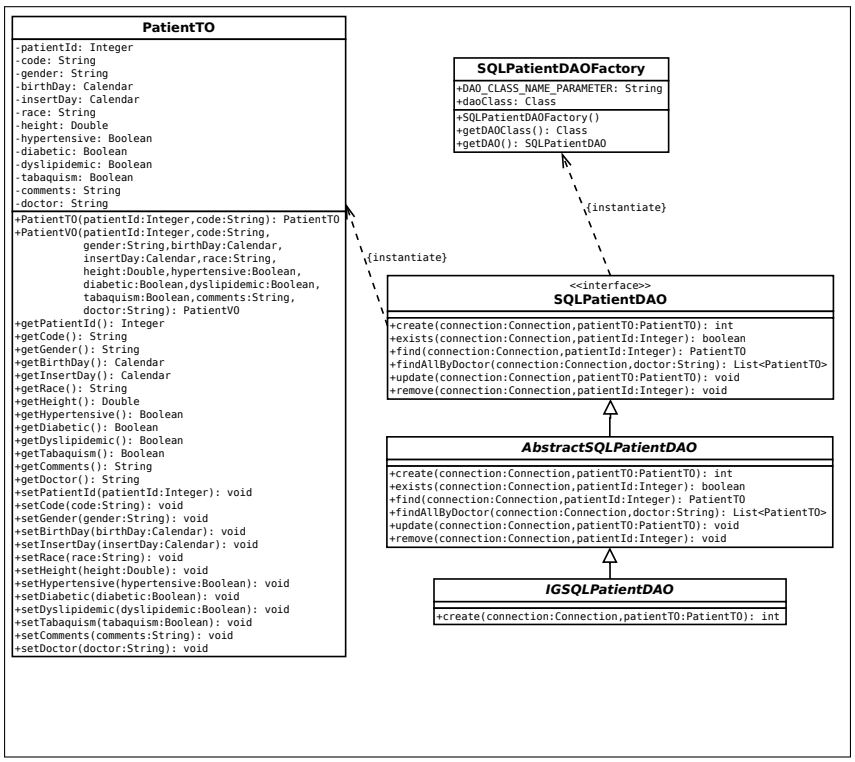

Figure 5.4: Examples of Transfer Object and Data Access Object design patterns for the patient.

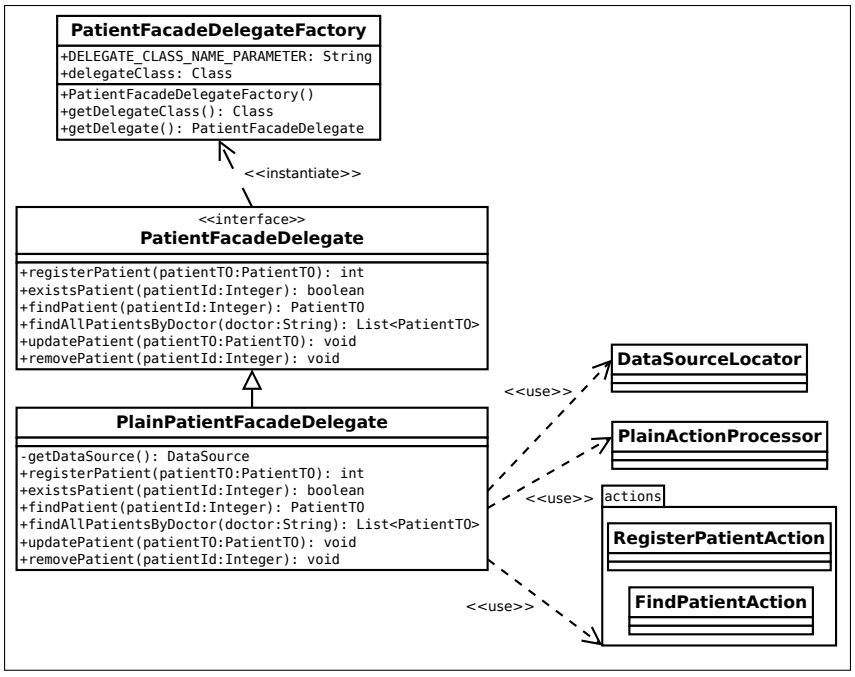

Figure 5.5: Examples of Facade and Abstract Factory design patterns.

addition, this protocol allows to connect applications written in different programing languages local or remotely, whereas other technologies such as Java Native Interface (JNI) do not allow remote connection.

The library used to implement the XML-RCP specification, xmlrpc-c, uses the HTTP protocol for the communication whereas the transmitted data are encoding using XML. Thus, the server which implements the XML-RPC protocol is included in the image service layer, whereas the xmlrpc client is created by the corresponding DAO object involved in a request from a facade. Before calling the server, the request in XML format with the appropriate data must be created. The response are given also in XML format. The communication between the two parts can be observed in the Figure 5.6 which shows a sequence diagram for the use case of automatic AVR calculus.

Regarding the other components, the API of J2SE, JDBC, is used for the access to the relational database. The database management system selected was PostgreSQL. For the controller and view layers, we use the framework Jakarta Struts which gives the support to the MVC pattern. Moreover, it provides a complete tag library for the Java Serves Pages (JSP) to implement the graphic interface. In the JSP pages, we use, additionally, the JSP Standard Tag Library (JSTL) offered by J2EE. Furthermore, some use case such as, *View/Edit an AVR result* use AJAX techniques to incorporate new data in a page already loaded into the browser. The data are passed in JavaScript Object Notation (JSON) format. Other JavaScript libraries such as JQuery are used in the view. Regarding the image management in the web application, we use JMagick library, a Java interface for ImageMagick.

Figure 5.7 shows screenshots from the SIRIUS system where the main use cases of the Administrator user can be seen. Also samples of the patient and checkup managements are displayed in Figures 5.8 and 5.9. Figure 5.10 includes two screenshots which show the integration of the AVR monitoring system in the SIRIUS web application.

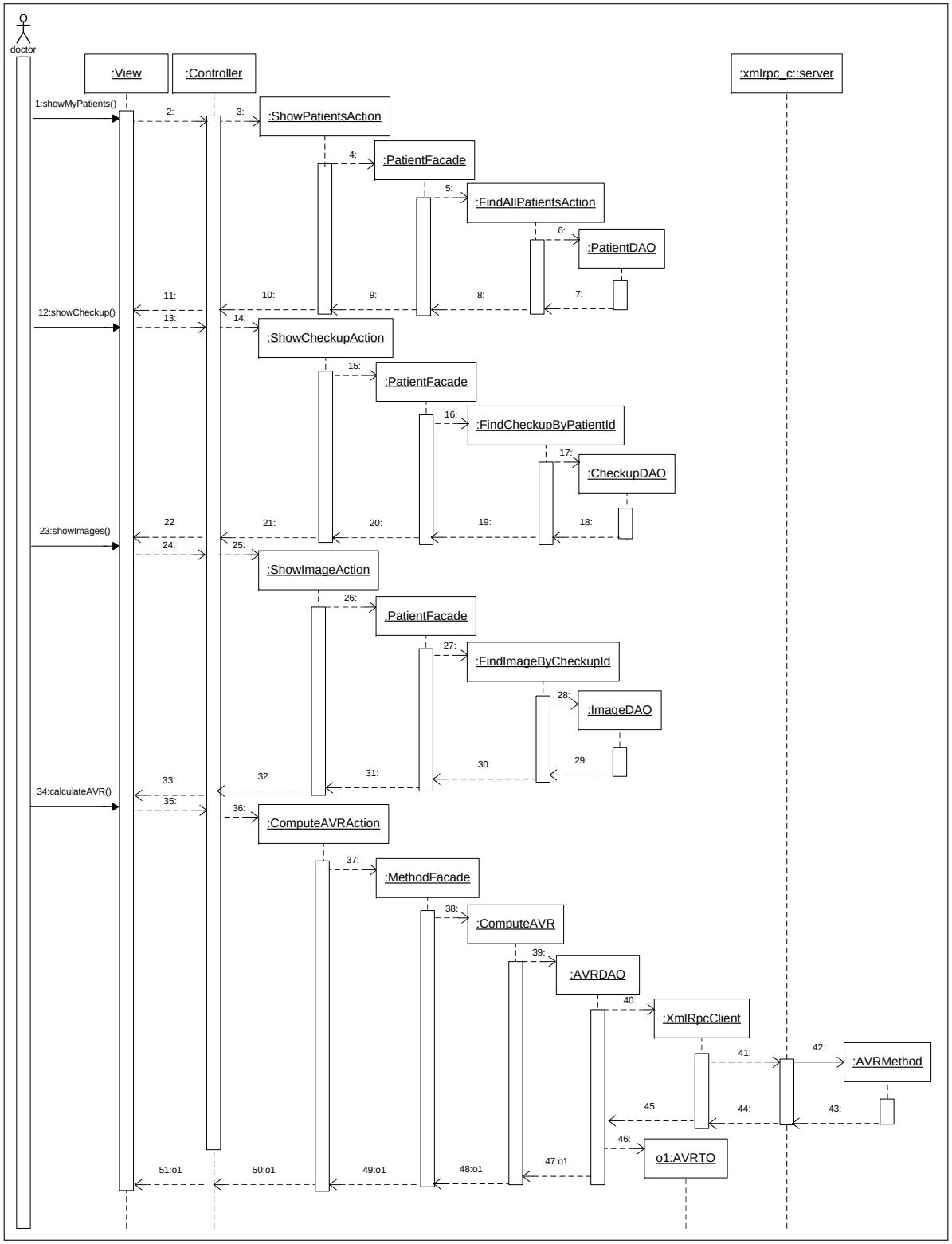

Figure 5.6: Sequence diagram for the use case of automatic AVR calculus.

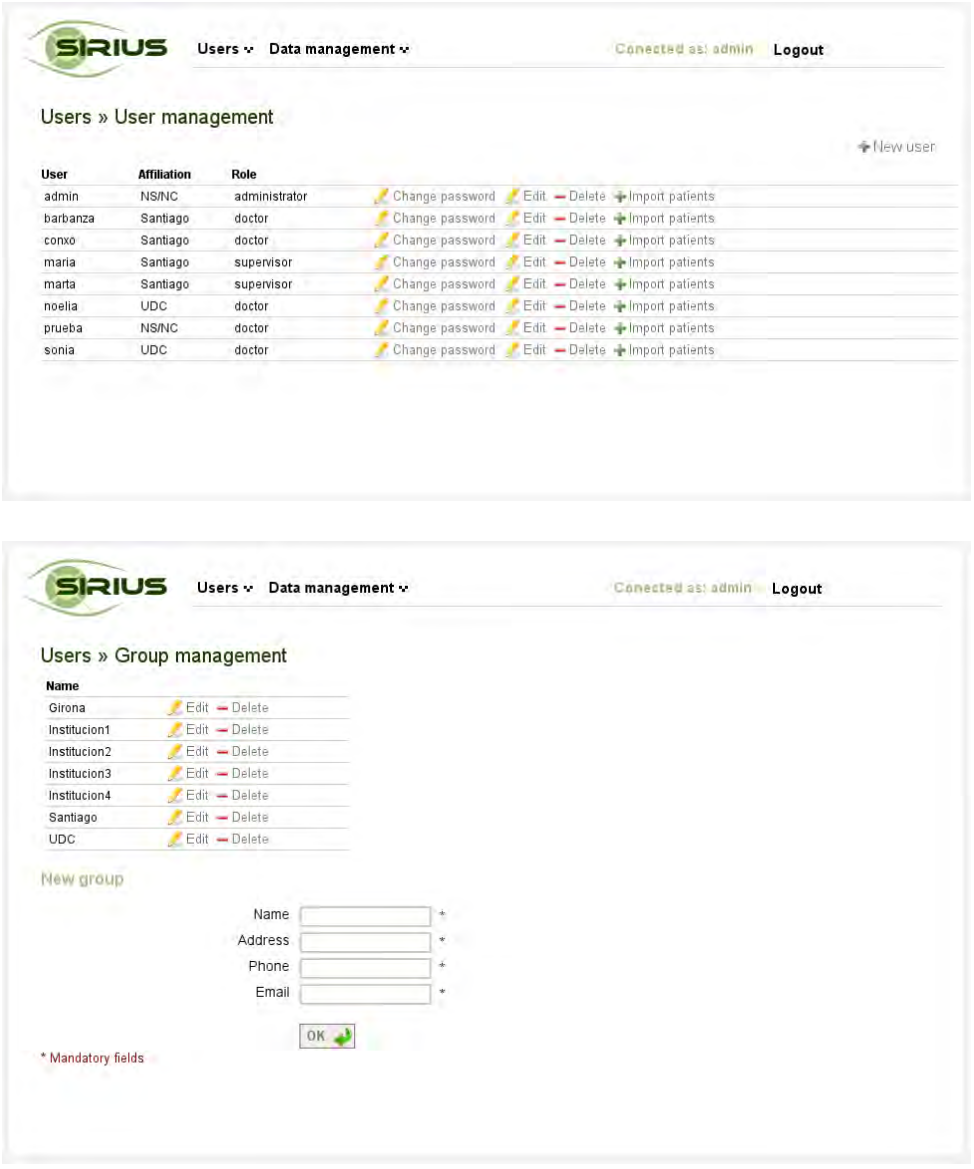

Figure 5.7: Screenshots of samples of the user and center management in SIRIUS system.

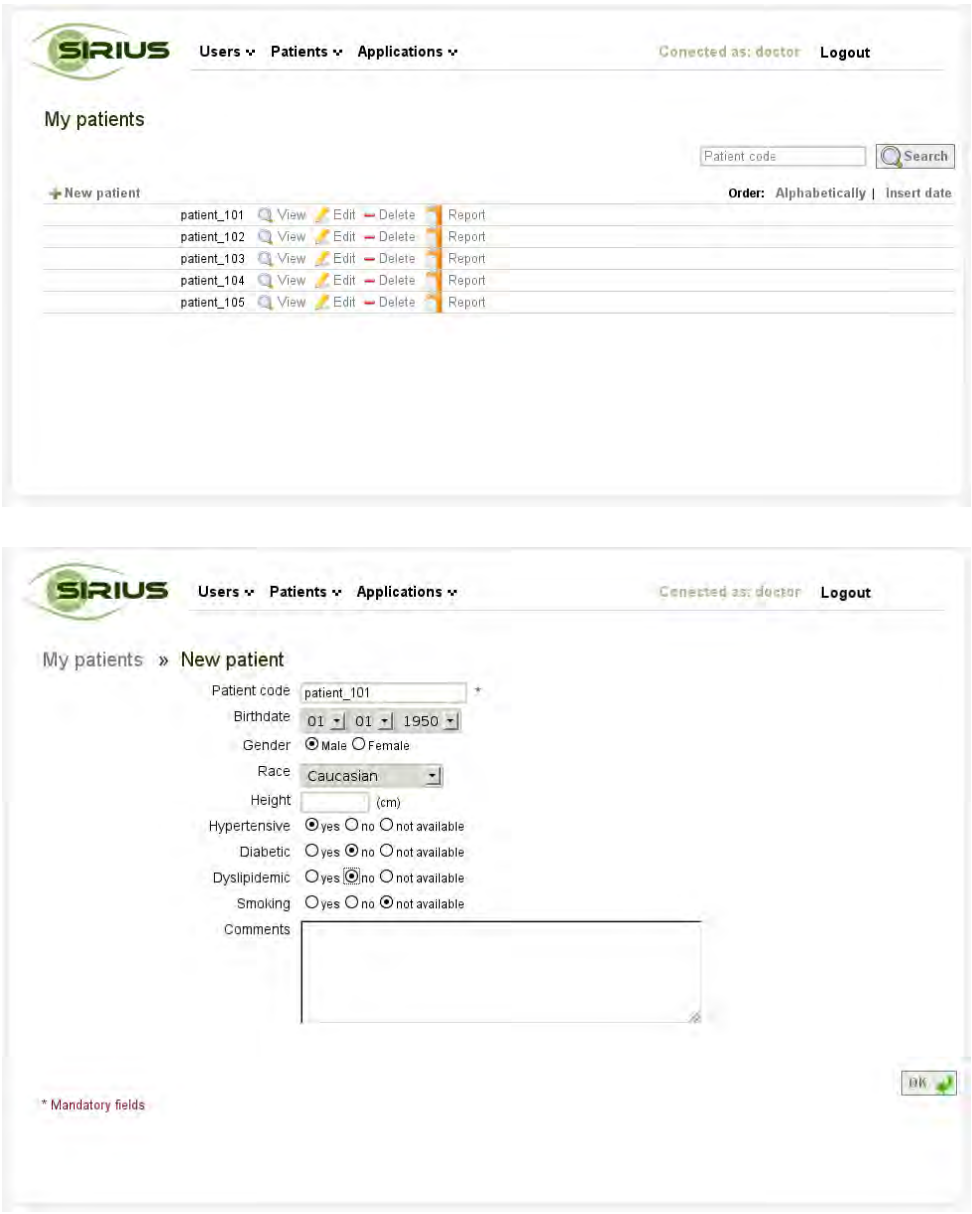

Figure 5.8: Screenshots of samples of the patient management in SIRIUS system.

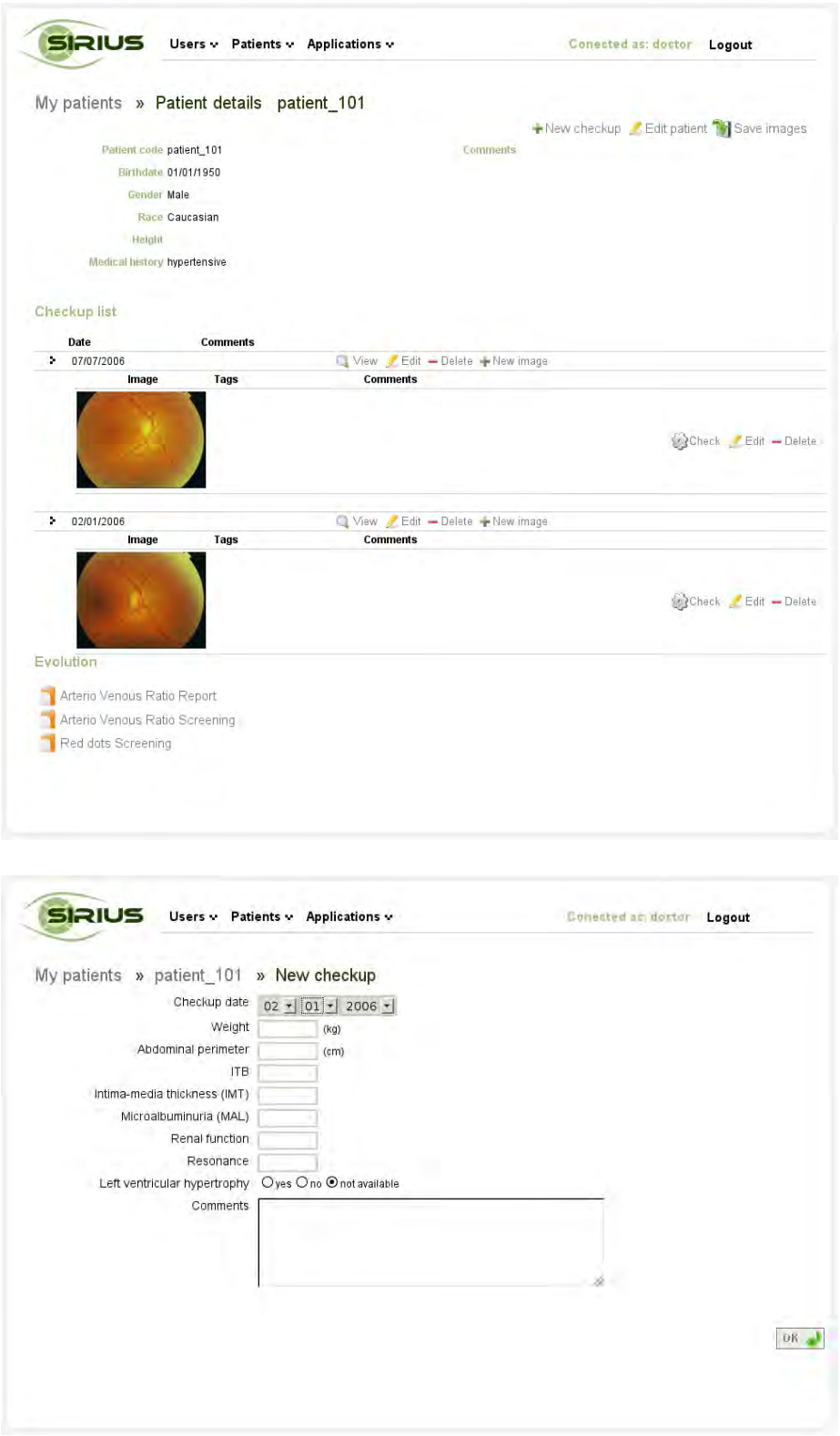

Figure 5.9: Screenshots of samples of the checkup management in SIRIUS system.

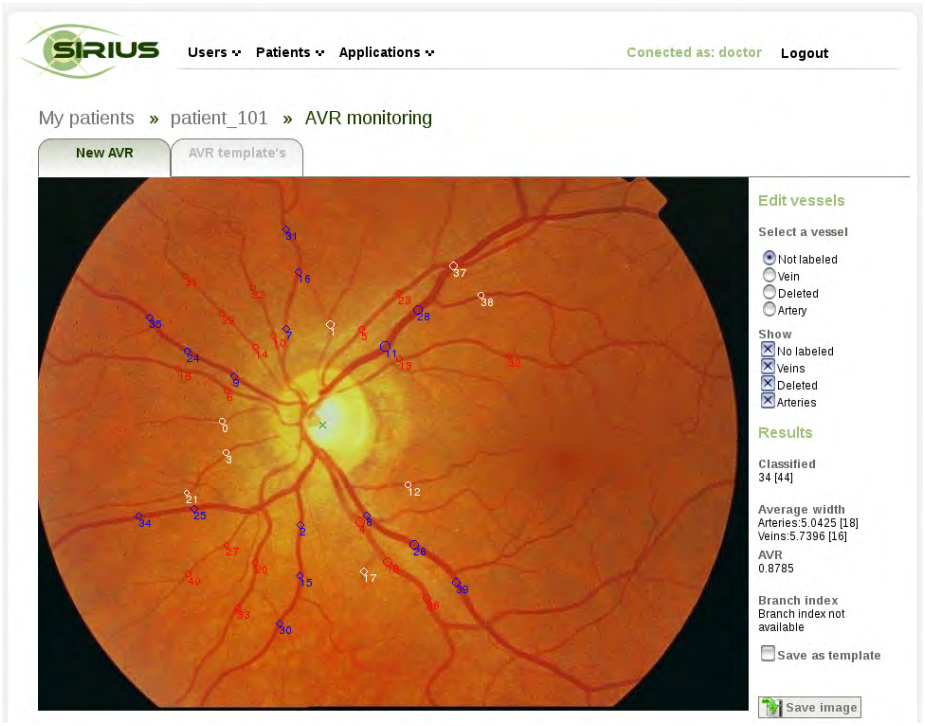

(a)

(b)

Figure 5.10: Screenshot of the AVR monitoring system in the SIRIUS web application. (a) The interface for visualization and edition the AVR in a new sample image (first tab) and in the reference image (second tab). (a) Interface which shows at right the list of the AVR measurements computed in new sample images using the reference AVR displayed at left side.

Chapter 6

Results

In this chapter, the experiments performed to test the methodology for the AVR computation are described, summarizing the main obtained results. Each step of the methodology is analyzed using different public retinal image databases. Our results are compared with other methods found in the literature. Furthermore clinical results are reported.

This chapter is structured as follows. Section 6.1 describes the different databases used in the performed experiments, Section 6.2 focuses on the evaluation of the methodology, whereas Section 6.3 is directed to the clinical validation.

6.1 Materials

This section describes the fundus image datasets used in the diverse experiments. These databases were created in several laboratories and research groups in order to test different algorithms of retinal image analysis. They are publicly accessible on the Internet.

6.1.1 DRIVE database

DRIVE [123] is a public database widely used for retinal blood vessels segmentation. It is make up of forty images randomly selected from 400 diabetic subjects between 25-90

years of age; 33 images do not show diabetic signs, whereas 7 reveal signs of mild early diabetic retinopathy. The images have been taken using a Cannon CR5 non-mydriatic 3CCD camera with a 45 degree field of view. Each image has 8 bits per color channel and a resolution of 768×584 pixels. The images have been grouped in a training and a test set of 20 images each. For the training set, there is a manual segmentation available, whereas for the test set there are two.

6.1.2 REVIEW database

It was published recently [124] and it constitutes the unique publicly available database which includes ground truth vessel width measurements. Three observers have marked the vessel boundaries using a graphical user interface.

REVIEW is composed of sixteen heterogeneous images grouped in four different subsets: CLRIS, HRIS, VDIS, and KPIS. CLRIS contains two retinal images which present early atherosclerotic changes such as stiffness and strong central light reflex. In this set, the image resolution is 2160×1440 and the observers have marked 285 vessel profiles. The HRIS subset consist of four high resolution images of 3584×2438 pixels which present alterations related to different grades of diabetic retinopathy. In this set, 2368 profiles have been measured by the observers. The images of both subsets are centered in the macula. The VDIS subset is made up of eight nasal and temporal noisy images with a resolution of 1360×1024 pixels. These images are affected by pathologies like diabetic retinopathy. The set contains 2249 vessel profiles. The last subset, KPIS, contains 164 profiles in two small resolution images (288×119 and 170×92 pixels). Each image is the result of cropping a 3300×2600 pixel image around a big vessel segment.

In total, the database contains 5066 vessel profiles marked by the three observers. For each profile, the Cartesian coordinates of the two end points, (x_1, y_1) and (x_2, y_2), marked by the each observer are given, being the vessel width the euclidean distance between these points.

6.1.3 POSTEL database

POSTEL database [125] was created in the POSTEL project developed by the VARPA group and the Service of the Internal Medicine of the Conxo Hospital in Santiago de Compostela, Spain. The project was funded by Boehringer Ingelheim España, S.A. and it lied in the clinical validation of the semiautomatic method for the AVR computation integrated in the SIRIUS system.

The database is composed of images acquired from 96 hypertensive patients. The images have been acquired centered on the optic disc in the service of internal medicine of the Conxo Hospital in Santiago de Compostela, Spain and the Abente Lago Hospital in A Coruña, Spain. Two images, one per eye, have been acquired with a Cannon CR6-45NM non-mydriatic retinal camera for almost all patients. The images were stored with a resolution of 768×576 pixels in JPEG format and 8 bits per color channel.

Each patient, after a basal assessment and an image acquisition, started an anti-hypertensive treatment. After 6 months, a new image was acquired.

Two ophthalmologists with many years of experience in the study of the hypertensive retinopathy as well as, its evolution and treatment, have computed the AVR with the SIRIUS application in a semiautomatic mode. That is, each expert selected manually the optic disc position and the set of vessel segments to compute the AVR, classifying them into arteries and veins.

6.1.4 VICAVR database

This database is a subset of 58 images taken randomly from the POSTEL dataset. Three experts have computed the AVR using five circumferences concentric to the optic disc. The radii of the circumferences are equally spaced and they range from $1.5r$ to $2.5r$, where r is the optic disc radius. From 3816 vessel segments, the experts classified into artery and vein classes 2471, 2778, and 2943 vessels, respectively. The classification agreement among experts is considerably high as Table 6.1 shows. The agreement is computed as

the quotient between the number of vessels that were classified in the same class by all experts and the number of vessels that were simultaneously labeled by them.

	Expert$_1$	**Expert$_2$**	**Expert$_3$**
Expert$_1$	-	98.12%	96.69%
Expert$_2$	-	-	97.37%
Expert$_3$	-	-	-
Three-agreement		96.53%	

Table 6.1: Percentage of the artery/vein classification agreement among the three experts in the VICAVR database.

VICAVR database has been published [126, 83], including the ground truth of the vessel widths measured at different analysis radii as well as the vessel type (artery/vein) labeled by the three experts.

The dataset was enlarged to 100 images constituting the VICAVR-2 database [127, 85]. In this case, each image was manually labeled by two different medical experts who focused on the vessel classification of all known vessel segments instead of selecting and classifying just a suitable set of vessels for the AVR computation. The medical experts have classified the vessels found within seven analysis radii equally spaced from $1.5r$ to $3.0r$, where r is the optic disc radius.

6.1.5 VAMPAHICA database

This dataset was created in the VAMPAHICA study (acronym in Spanish for Assessment of the self monitoring of blood pressure in the diagnosis of isolated clinical hypertension) [128]. This study was a multi-center prospective study which involved 14 primary care centers in the Healthcare Region of Girona (Spain). Patients involved in this study were untreated, and recently diagnosed hypertensive patients recruited from 2003 to 2006.

For each patient, two fundus images, one per eye, have been acquired using a retinograph equipped with a non-mydriatic fundus camera (Canon CR6-45NM, Camera EOS D30). After one year of treatment, two new retinal images have been taken for each

patient.

Each image was captured centered at macula using 8 bits per color plane at 2160×1440 pixels with JPEG compression.

6.2 Evaluation of the AVR computation methodology

The experiments carried out to evaluate the performance of each step of the proposed methodology are summarized in the following sections. An outline of the experiments is given in the Table 6.2.

Experiment	Description	Database
Optic disc	The performance of the optic disc location method is tested	POSTEL, DRIVE
Vessel width	The vessel width measurement approach is compared with manual assessments	REVIEW
Vessel classification	The characterization of vessels in arteries and veins is compared with manual labelings	VICAVR, VICAVR-2
AVR	The AVR computation methodology and the AVR monitoring system are tested	POSTEL

Table 6.2: Outline of the experiments carried out to evaluate the AVR computation methodology.

6.2.1 Optic disc location

In this section the methodology for the OD location is tested in the DRIVE and POSTEL databases. The main aim is to minimize the distance between the detected center and the true center. To validate our methodology and according to Hoover et al. [38], we considered that an OD location is correct if the distance from its center to the real center is lower or equal to 60 pixels. Table 6.3 shows our success rates for both databases, as well as, the results achieved by other techniques proposed in the literature. The results indicate the method is satisfactory in these datasets however it needs an improvement in

retinas with diseases. The main drawback of the proposed method in unhealthy images is that it is based fundamentally on detecting the brightest region on the image where there is high presence of centerline vessels. However, in these images, there are other regions brighter than the OD due to big hard exudates or due to an inappropriate capture process where the false positive vessels are more likely.

Figures 6.1 and 6.2 show some examples of the OD location in DRIVE and POSTEL databases.

	Success rate (%)	
Method	**POSTEL**	**DRIVE**
Our method	94.30	95
Youssif et al. [39]	-	100
Mendonça et al. [41]	-	100

Table 6.3: Optic disc location accuracy in DRIVE and POSTEL databases.

Figure 6.1: Examples of optic disc location in DRIVE database, including the two images where the method failed.

6.2.2 Vessel width measurement

The aim of this section is to check the performance of the method proposed for the vessel width measurement regarding the manual estimation made by human experts. To this end, we use the REVIEW database.

Figure 6.2: Examples of optic disc location in POSTEL database.

The REVIEW images are not centered in the optic disc and the published gold standards measured by the three observers are scattered over the vascular tree. However, our method does not segment the whole vascular tree, it just measures the widths in the vessel segments found in a few analysis radii around the optic disc. Hence, to get high sensitivity and to compare our measurements with the largest number of profiles measured by the observers, many radii as necessary to cover the entire retina surface were taken into account. Thus, the method was applied in all circumferences spaced a distance $0.1r$ with analysis radii from $1.5r$ up to the image boundaries, being r the optic disc radius manually determined (Figure 6.3).

In order to maximize the sensitivity, for each vessel segment, we consider the seven assessments obtained in the seven profiles instead of taking into account only the average of the three profile central values. Moreover, the images of the high resolution sets, HRIS and CLRIS, are resized to half their size before applying the method in order to prevent wrong edge detection at the central light reflexes.

The average between the coordinates of the three observers is established as the reference standard. Then, a profile, P, detected and measured by the proposed method is considered a success measurement, that is, it is included in the evaluation, if it matches a profile S in the reference standard. The matching is successful if the distance between the middle points of both profiles is less than 3 pixels as follows

$$P \text{ matches } S \Leftrightarrow dist(m_P, m_S) < 3 \tag{6.1}$$

where $m_P = \left(\frac{p1_x+p2_x}{2}, \frac{p1_y+p2_y}{2}\right)$ is the middle point of profile P, being p_1 and p_2 the profile

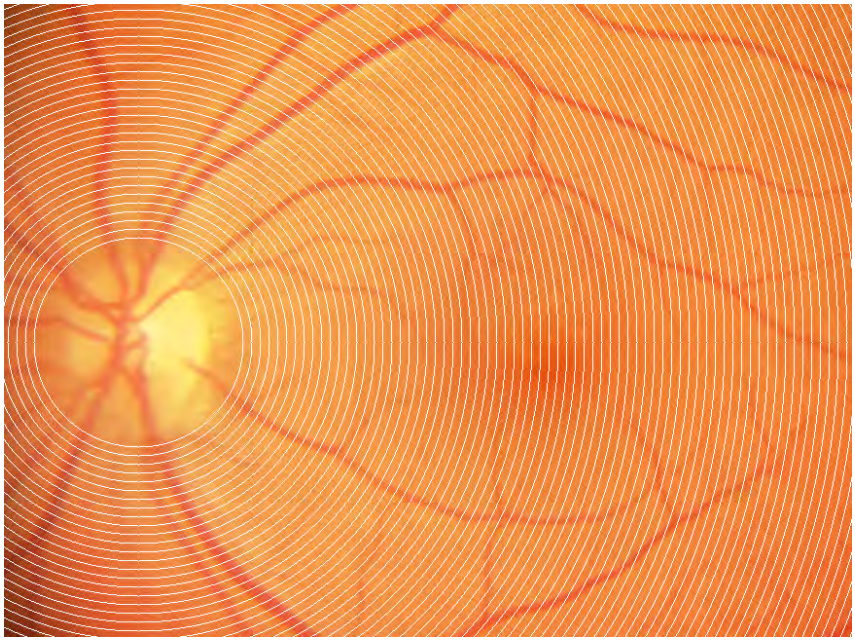

Figure 6.3: Analysis radii used to test the vessel width measurement in a sample image of VDIS subset from the REVIEW database

end points, whereas $m_S = \left(\frac{s1_x+s2_x}{2}, \frac{s1_y+s2_y}{2}\right)$ is the middle point of profile S with s_1 and s_2 the end points.

The influence of different image color spaces in the vessel measurement has been evaluated. We have tested the green channel of the RGB color model (G), the lightness from the Lab color space (L) and two gray transformations. The first one obtains a light gray scale image and is obtained by means of $I = 0.299R + 0.587G + 0.114B$. The second gray transformation (J) produces a darker image in order to remove background noise and small vessels. It is computed as follows:

$$\begin{cases} \underset{\in\{R,G,B\}}{X} = \begin{cases} \frac{X}{12.92} & \text{if } X \leq 0.03928 \\ \left(\frac{(X+0.055)}{1.055}\right)^{2.4} & \text{otherwise} \end{cases} \\ J = 0.2126R + 0.7152G + 0.0722B \end{cases} \tag{6.2}$$

Tables 6.4 and 6.5 show the accuracy of the proposed method in the four REVIEW subsets as well as the performance obtained by other techniques: the Gregson's [64],

HHFW [63], 1D Gaussian [65], 2D Gaussian [66], ESP [61], the Graph-based [68] and ULDM [69] methods. The first row block shows the observer's results. The accuracy of the proposed method using different images is provided in the second one. Finally, the last block of the table shows the accuracy obtained for other algorithms provided in [61, 68, 69]. In addition, the rate of profiles included in the test is shown in the first column. The next two columns contain the mean and the standard deviation of the vessel width measurement. Finally, the last columns show the mean and the standard deviation of the differences respect to the reference standard point by point.

In general, the results reflect the proposed method underestimates the vessel widths respect to the reference standard like other techniques. In the case of KPIS subset, this underestimation is greater than a pixel. This fact can be appreciated in Figure 6.4 which shows a sample KPIS image. However, in this image, it seems the observers overestimate the real vessel width.

The CLRIS subset constitutes the exception of the vessel width underestimation. The boundary returned by the Canny edge detector has an offset in some vessel segments as Figure 6.5 shows. The reason for this performance could be the JPEG compression applied to this set of images. In fact, in the figure, we can see a phenomenon that causes diffuse edges, specially in arteries, hindering the location of these even for the observers.

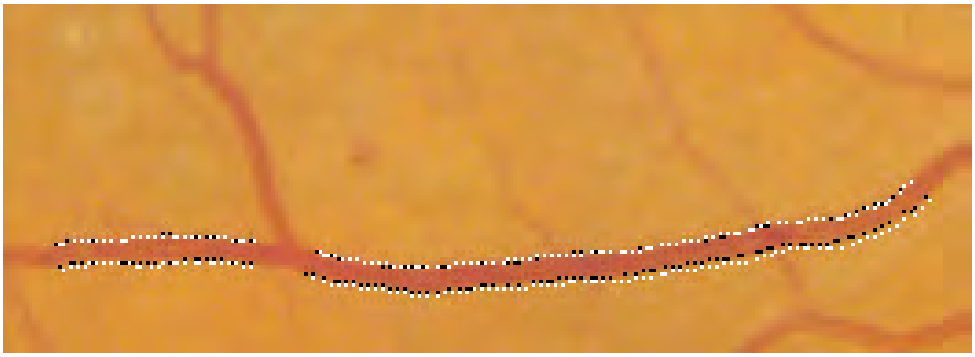

Figure 6.4: Vessel width measurement in a sample image of KPIS dataset from REVIEW database. White points correspond to the reference standard obtained from the three observers, whereas black points depict the segmentation of the proposed method.

Regarding the color spaces, the maximal sensitivity is achieved using the G image

	KPIS					CLRIS				
Method	Profiles	Measurement		Difference		Profiles	Measurement		Difference	
Name	%	μ	σ	μ	σ	%	μ	σ	μ	σ
Observer 1	100	6.99	0.52	-0.51	0.23	100	13.19	4.00	-0.59	0.56
Observer 2	100	7.60	0.42	0.09	0.21	100	13.68	4.22	-0.10	0.69
Observer 3	100	7.97	0.47	0.46	0.23	100	14.52	4.25	0.72	0.56
Standard	100	7.51	0.41	0	0	100	13.79	4.11	0	0
Sirius G	100	6.20	0.63	-1.28	0.76	91.58	14.69	3.69	0.83	2.17
Sirius L	100	6.15	0.61	-1.33	0.74	74.39	16.10	4.74	1.20	4.26
Sirius J	100	6.44	0.63	-1.05	0.73	80.35	16.04	3.61	1.52	2.30
Sirius I	100	6.23	0.63	-1.26	0.75	75.79	15.85	3.52	1.27	2.51
Gregson's	100	7.29	-	-0.23	0.60	100	12.8	-	-1.0	2.84
HHFW	96.3	6.47	-	-1.05	0.38	-	-	-	-	-
1D Gaussian	100	4.95	-	-2.57	0.39	98.6	6.3	-	-7.5	4.13
2D Gaussian	100	5.87	-	-1.65	0.33	26.7	7.0	-	-6.8	6.01
ESP	100	6.56	-	-0.96	0.32	93.0	15.7	-	-1.90	1.46
Graph-based	99.4	6.38	0.59	-1.14	0.67	94.1	14.05	4.47	0.08	1.78
ULDM	100	7.02	0.67	-0.50	0.60	98.2	13.23	3.55	-0.55	1.79

Table 6.4: Vessel width measurement accuracy in KPIS (164 profiles) and CLRIS (285 profiles) sets from REVIEW database.

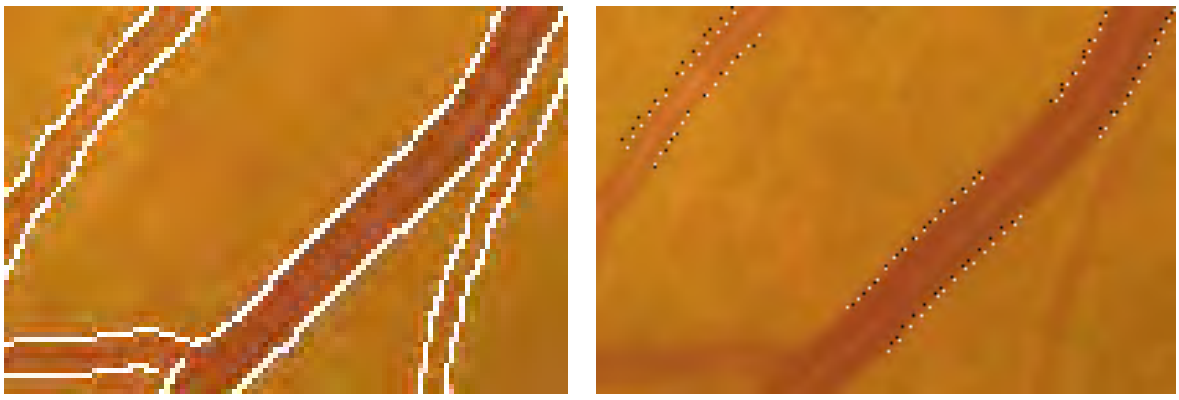

(a) (b)

Figure 6.5: Vessel width measurement in a sample image of CLRIS dataset from REVIEW database. (a) Canny output superimposed on the resized image. (b) the boundary points corresponding to the reference standard (in white) and detected by the method (in black), superimposed on the original image.

which presents the highest contrast, whereas in the J image less profiles are detected. The mean width and standard deviation indicate that G and L widths are the smallest, whereas J width tends to be the largest one. In fact, the L width has always the smallest deviation, except in CLRIS subset where the less sensitivity and some atypical values could produce the largest deviation. These results are also reflected in the differences point to point where the smallest difference respect to the observers is achieved with J, except for the CLRIS subset where the method overestimates the width. In this case, G width is the closest to the observers. However, despite these differences the widths achieved with the different components are very similar.

Moreover, it should be noted that in all sets except CLRIS, the standard deviation of the differences point to point is small, less than or around 1.

	VDIS					**HRIS**				
Method	Profiles	Measurement		Difference		Profiles	Measurement		Difference	
Name	%	μ	σ	μ	σ	%	μ	σ	μ	σ
Observer 1	100	8.49	2.54	-0.33	0.54	100	4.11	1.25	-0.22	0.26
Observer 2	100	8.90	2.69	0.072	0.62	100	4.35	1.34	0.007	0.27
Observer 3	100	9.14	2.67	0.31	0.67	100	4.58	1.25	0.23	0.30
Standard	100	8.83	2.5	0	0	100	4.34	1.25	0	0
Sirius G	78.70	8.13	2.45	-0.95	1.11	78.89	4.26	1.10	-0.13	0.85
Sirius L	69.68	8.17	2.19	-1.29	1.08	81.71	4.16	1.07	-0.22	0.88
Sirius J	57.80	8.44	2.39	-0.84	1.19	73.86	4.35	1.12	0.08	0.80
Sirius I	74.34	8.18	2.36	-1.17	1.12	83.36	4.25	1.17	-0.14	0.96
Gregson's	100	10.07	-	1.22	1.49	100	7.64	-	3.29	2.84
HHFW	78.4	7.94	-	-0.91	0.87	88.3	4.97	-	0.62	0.92
1D Gaussian	99.9	5.78	-	-3.07	2.11	99.6	3.81	-	-0.54	4.13
2D Gaussian	77.2	6.59	-	-2.26	1.32	98.9	4.18	-	-0.17	6.01
ESP	99.6	8.80	-	-0.05	0.76	99.7	4.63	-	0.28	0.42
Graph-based	96.0	8.35	3.00	-0.53	1.43	100	4.56	1.30	0.21	0.56
ULDM	96.3	8.68	2.82	-0.64	1.18	99.6	4.19	1.35	0.21	0.79

Table 6.5: Vessel width measurement accuracy in VDIS (2249 profiles) and HRIS (2368 profiles) sets from REVIEW database.

6.2.3 Vessel classification

This section is devoted to test the proposed characterization of retinal vessels into arteries and veins. The aim is to minimize the classification error rate taking into account the grading made by medical experts. To assess the validity of the classification, we have considered several statistical measures: The *sensitivity* and *specificity* of the method for detecting artery ($\text{Sens}_{\mathcal{A}}$,$\text{Spec}_{\mathcal{A}}$) and vein ($\text{Sens}_{\mathcal{V}}$,$\text{Spec}_{\mathcal{V}}$) vessels segments. The sensitivity measures the proportion of actual positives which are correctly identified, whereas, the specificity measures the proportion of negatives which are classified properly. They are computed as follows

$$\begin{aligned} \text{Sens}_{\mathcal{A}} &= \frac{\text{TP}_{\mathcal{A}}}{\text{TP}_{\mathcal{A}} + \text{FN}_{\mathcal{A}}} \quad \text{Sens}_{\mathcal{V}} = \frac{\text{TP}_{\mathcal{V}}}{\text{TP}_{\mathcal{V}} + \text{FN}_{\mathcal{V}}} \\ \text{Spec}_{\mathcal{A}} &= \frac{\text{TN}_{\mathcal{A}}}{\text{TN}_{\mathcal{A}} + \text{FP}_{\mathcal{A}}} \quad \text{Spec}_{\mathcal{V}} = \frac{\text{TN}_{\mathcal{V}}}{\text{TN}_{\mathcal{V}} + \text{FP}_{\mathcal{V}}} \end{aligned} \tag{6.3}$$

where TP, FP represent the proportion of true and false positives, respectively, whereas TN and FN depict the proportion of true and false negatives. A vessel segment is considered as a positive vein (artery) if its probability to be vein (artery) is greater than 0.5.

Moreover, we calculate also global measures, the *accuracy rate* (AR), that is, the percentage of the vessel segments which have been correctly classified to the total of vessels segments detected by the system, as well as the *error rate* (ER), the percentage of miss-classifications without taking into account the vessels which are classified by the system as not labeled.

$$\begin{aligned} \text{AR} &= \frac{n_{\text{correct}}}{n_{\text{vessels}}} \cdot 100 = \frac{\text{TP}_{\mathcal{A}} + \text{TP}_{\mathcal{V}}}{n_{\text{vessels}}} \cdot 100 \\ \text{ER} &= \frac{n_{\text{incorrect}}}{n_{\text{labeled vessels}}} \cdot 100 = \frac{\text{FP}_{\mathcal{A}} + \text{FP}_{\mathcal{V}}}{n_{\text{labeled vessels}}} \cdot 100 \end{aligned} \tag{6.4}$$

where n_{correct} and $n_{\text{incorrect}}$ are the number of vessel segments, veins and arteries, correctly and incorrectly classified, respectively, and n_{vessels} is the total number of detected vessel segments that includes the number of vessel segments which have not been able to classify whereas $n_{\text{labeled vessels}}$ does not take into account the no labeled vessels.

Local clustering

The proposed local classification was tested in the VICAVR dataset as well as in a subset of 20 images taken randomly from this database.

The first experiment presented focuses on comparing the proposed rotating quadrant procedure with two other strategies in the subset of 20 images using different feature vectors. Both strategies classify the vessel segments found in each analysis radius separately as the rotating quadrant method does. However, the first strategy performs an unique classification for all vessel segments found in each analysis radius, whereas in the second one, the retina image is divided into four quadrants and the clustering is applying at each quadrant. Three circumferences of analysis with radii $2r$, $2.5r$ and $3r$ were considered, being r the optic disc radius. Table 6.6 shows the sensitivity, specificity and the accuracy rate for the three strategies using different pixel based feature vectors described in Chapter 3. In order to make the tables more readable, only the results obtained respect to the agreement among the three experts are shown. In the three strategies, the best results were achieved with the H, G and the union of G and R components, whereas the worst results were obtained with the R component and the union of the mean of H and variance of R. Regarding the strategies, the rotating quadrant method obtains the highest accuracy. It is worth to point out that the low accuracy rate in the quadrant division strategy is mainly due to the high number of unclassified vessels mainly since a minimum of three vessel segments is required to perform the classification in a quadrant.

In a second experiment, we try to minimize the error committed with the rotating quadrant strategy. To this end, instead of considering the image component values in all points of the profiles, we analyze different statistical measures to minimize the effect of both noise and outliers in the profile color information. So, we test the average (μ) and the median ($\tilde{x}$) of all the values in the profile as well as the five most repeated values in the profile and the mean of these five values. The classification performance using these profile based feature vectors in the analysis radius $2.5r$ is shown in the Table 6.7. The median of the G component turned out to be the most discriminant feature.

		2r					**2.5r**					**3r**				
Strategy	**Features**	$\text{Sens}_{\mathcal{V}}$	$\text{Spec}_{\mathcal{V}}$	$\text{Sens}_{\mathcal{A}}$	$\text{Spec}_{\mathcal{A}}$	AR	$\text{Sens}_{\mathcal{A}}$	$\text{Spec}_{\mathcal{A}}$	$\text{Sens}_{\mathcal{V}}$	$\text{Spec}_{\mathcal{V}}$	AR	$\text{Sens}_{\mathcal{A}}$	$\text{Spec}_{\mathcal{A}}$	$\text{Sens}_{\mathcal{V}}$	$\text{Spec}_{\mathcal{V}}$	AR
No division	H	87.88	68.09	68.09	87.88	78.24	81.37	74.26	74.26	81.37	77.83	82.24	69.70	68.69	82.24	75.73
	R	71.72	64.89	64.89	73.74	68.39	69.61	71.29	71.29	69.61	70.44	65.42	72.73	72.73	65.42	68.93
	G	83.84	69.15	69.15	83.84	76.68	85.29	70.30	70.30	85.29	77.83	85.05	60.61	59.60	85.05	72.82
	I	83.84	69.15	69.15	83.84	76.68	84.31	68.32	68.32	84.31	76.35	82.24	59.60	59.60	82.24	71.36
	G, R	83.84	70.21	70.21	83.84	77.20	82.35	70.30	70.30	82.35	76.35	82.24	66.67	65.66	82.24	74.27
	μ_H, σ_R	79.80	63.83	63.83	79.80	72.02	76.47	63.37	61.39	78.43	68.97	85.05	50.51	50.51	85.05	68.45
Quadrant division	H	72.73	84.04	68.09	91.92	70.47	78.43	79.21	70.30	90.20	74.38	71.03	74.75	69.70	84.11	70.39
	R	64.65	70.21	54.26	83.84	59.59	70.59	76.24	66.34	82.35	68.47	66.36	77.78	71.72	79.44	68.93
	G	73.74	79.79	63.83	92.93	68.91	78.43	79.21	70.30	90.20	74.38	74.77	74.75	67.68	89.72	71.36
	I	73.74	75.53	59.57	92.93	66.84	78.43	73.27	61.39	90.20	69.95	76.64	76.77	71.72	89.72	74.27
	G, R	71.72	77.66	60.64	90.91	66.32	77.45	81.19	72.28	89.22	74.88	69.16	80.81	75.76	83.18	72.33
	μ_H, σ_R	63.64	76.60	60.64	84.85	62.18	59.80	65.35	55.45	72.55	57.64	63.55	65.66	59.60	79.44	61.65
Quadrant rotation	H	90.91	79.79	79.79	90.91	85.49	86.27	82.18	82.18	86.27	84.24	82.24	77.78	77.78	82.24	80.10
	R	79.80	64.89	64.89	79.80	72.54	80.39	73.27	73.27	80.39	76.85	79.44	74.75	74.75	79.44	77.18
	G	91.92	78.72	78.72	91.92	85.49	90.20	80.20	80.20	90.20	85.22	88.79	71.72	71.72	88.79	80.58
	I	90.91	74.47	74.47	90.91	82.90	90.20	74.26	74.26	90.20	82.27	88.79	71.72	71.72	88.79	80.58
	G, R	89.90	78.72	78.72	89.90	84.46	88.24	81.19	81.19	88.24	84.73	85.98	78.79	78.79	85.98	82.52
	μ_H, σ_R	81.82	73.40	73.40	81.82	77.72	77.45	63.37	63.37	78.43	70.44	77.57	63.64	63.64	77.57	70.87

Table 6.6: Vessel classification accuracy in a subset of 20 images from VICAVR database using different strategies and pixel based feature vectors.

Features		$\text{Sens}_{\mathcal{V}}$	$\text{Spec}_{\mathcal{V}}$	$\text{Sens}_{\mathcal{A}}$	$\text{Spec}_{\mathcal{A}}$	AR
μ	H	84.31	85.15	84.16	84.31	84.24
	R	78.43	83.17	83.17	78.43	80.79
	G	86.27	87.13	87.13	87.25	86.70
	I	85.29	86.14	86.14	85.29	85.71
	G, R	85.29	87.13	87.13	85.29	86.21
$\tilde{\mathrm{x}}$	H	81.37	85.15	85.15	81.37	83.25
	R	80.39	81.19	80.20	80.39	80.30
	G	87.25	87.13	87.13	88.24	87.19
	I	87.25	85.15	85.15	87.25	86.21
	G, R	86.27	86.14	85.15	86.27	85.71
5 frequent values	H	86.27	83.17	83.17	86.27	84.73
	R	82.35	72.28	72.28	82.35	77.34
	G	90.20	77.23	77.23	90.20	83.74
	I	89.22	72.28	72.28	89.22	80.79
	G, R	89.22	80.20	80.20	89.22	84.73
$\mu_{5 \text{ frequent values}}$	H	83.33	85.15	84.16	83.33	83.74
	R	78.43	84.16	84.16	78.43	81.28
	G	84.31	87.13	87.13	87.25	85.71
	I	86.27	87.13	87.13	86.27	86.70
	G, R	85.29	87.13	87.13	85.29	86.21

Table 6.7: Vessel classification accuracy in a subset of 20 images from VICAVR database using the rotating quadrant strategy and profile based feature vectors in an analysis radius of $2.5r$.

To confirm the previous results, we have tested the different strategies and feature vectors in a larger dataset, the VICAVR database. We have considered the five analysis radii equally spaced from $1.5r$ to $2.5r$ with r the optic disc radius. The best accuracy rate taking the agreement among the three experts as the gold standard was 86.34% achieved with the rotating quadrant strategy and the median of the G component of each profile. An area under the ROC curve of 0.93 indicates that the classification accuracy is good (Figure 6.6). In addition, the ROC curves show that the best thresholds to balance sensitivity and specificity in this set are 0.7 for veins and 0.3 for arteries. However, it may be interesting using other values in order to increase the specificity, in our case, considering probabilities higher than 0.5 as positives gives good specificities, 80.30 for veins and 93.81 for arteries.

The next experiment is devoted to test the local classification incorporating a light-

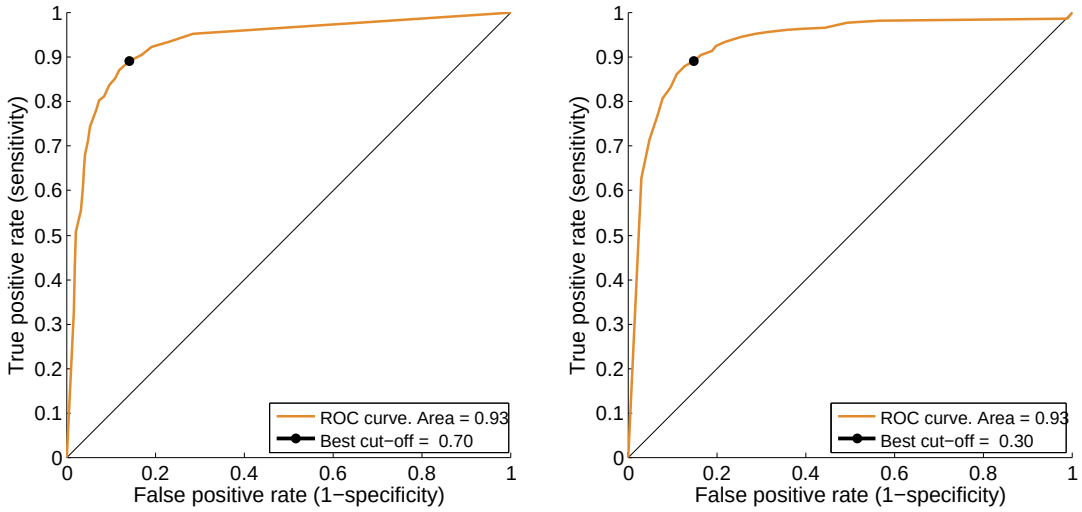

(a) (b)

Figure 6.6: ROC curves for the local clustering in the VICAVR database taking as positives the arteries (a) and the veins (b). It was computed using different threshold probability values and considering the agreement among the three experts as the gold standard.

ness and contrast normalization, the Retinex image enhancement B, in order to avoid the influence of the non color constancy. In this manner, the feature vectors used in the classification are selected from the retinex output image. We have applied the *Simple Scale Retinex* (SSR) and *Multi-Scale Retinex* (MSR) techniques to the VICAVR database, testing different scales in function of the image size. The scales are defined as $\sigma_d = min(\text{height}, \text{width})/d$, with $d \in \{1, 2, 4, 8, 16\}$. Since the VICAVR images have a resolution of 768×576 pixels, the scales were $\sigma_1 = 576$, $\sigma_2 = 288$, $\sigma_4 = 144$, $\sigma_8 = 72$, and $\sigma_{16} = 36$ pixels. Table 6.8 summarizes the best results obtained with the different retinex configurations applying quadrant rotation or without performing any division in the retinal image. There is not much difference between SSR and MSR results for the scales shown in the table. Nevertheless, with the smallest scales, the image loses tonal rendition and the number of miss-classifications increases. For the no division strategy, the table shows an increment in the accuracy rate over 8% using retinex. Thus, the inclusion of the normalization using retinex techniques offers the possibility of classifying the whole set of vessel segments together, without performing any partition. However, the rotating

quadrant strategy carries on minimizing the miss-classifications. It is worth pointing out as well that applying retinex, the feature formed by the G component value in each profile point, G, discriminates better than the median of G in the profile in most of cases. This could be due to the fact that retinex behaves as the median function removing outliers. If we consider only the miss-classifications, the best error percentages obtained applying the retinex technique were 9.49% and 8.38% for $\tilde{x}(G)$ and G, respectively. On the contrary, before applying retinex these values were 12.63% and 13.95%, respectively.

		No division					**Quadrant rotation**				
Retinex	**Features**	$\text{Sens}_{\mathcal{V}}$	$\text{Spec}_{\mathcal{V}}$	$\text{Sens}_{\mathcal{A}}$	$\text{Spec}_{\mathcal{A}}$	AR	$\text{Sens}_{\mathcal{V}}$	$\text{Spec}_{\mathcal{V}}$	$\text{Sens}_{\mathcal{A}}$	$\text{Spec}_{\mathcal{A}}$	AR
Before retinex	$\tilde{x}(G)$	91.25	71.68	70.36	91.60	81.52	92.66	80.30	79.09	93.81	86.34
	G	93.55	65.48	64.77	93.72	80.15	95.14	74.62	74.31	96.20	85.44
$\boldsymbol{MSR_{\sigma_1\sigma_2\sigma_8}}$	$\tilde{x}(G)$	89.12	87.82	87.01	89.57	88.14	91.25	88.63	88.02	92.31	89.74
	G	89.83	87.92	87.61	90.27	88.80	92.22	87.51	87.11	93.37	89.84
$\boldsymbol{MSR_{\sigma_2\sigma_4\sigma_8}}$	$\tilde{x}(G)$	87.80	89.44	88.73	88.95	88.23	91.07	88.32	87.51	92.22	89.41
	G	88.77	89.34	88.83	89.30	88.80	92.75	88.02	87.51	93.90	90.31
$\boldsymbol{SSR_{\sigma_2}}$	$\tilde{x}(G)$	86.56	88.73	88.53	87.00	87.48	90.10	88.93	88.22	91.42	89.22
	G	86.56	90.46	90.15	87.00	88.23	90.72	90.25	89.95	91.78	90.36
$\boldsymbol{SSR_{\sigma_4}}$	$\tilde{x}(G)$	87.71	88.63	87.71	88.63	87.81	90.63	87.51	87.01	91.87	88.94
	G	87.44	89.64	89.34	88.15	88.33	91.78	87.51	87.11	93.10	89.60
$\boldsymbol{SSR_{\sigma_3}}$	$\tilde{x}(G)$	86.91	90.05	89.44	87.71	88.09	90.45	89.34	88.63	91.60	89.60
	G	86.03	92.18	91.88	86.47	88.75	91.25	90.86	90.46	92.40	90.88

Table 6.8: Vessel classification accuracy in VICAVR database using Retinex image enhancement and different strategies of classification.

Vessel tracking

The presented results focus mainly in the evaluation of the vessel tracking procedure in the VICAVR-2 database which has been labeled specifically for testing the classification, and more secondary vessels than in VICAVR have been classified by the experts. The aim is to analyze different configurations of the algorithm. Thus, we evaluated the two proposed segmentation algorithms, different values for the β parameter, that is, the factor which multiplies the cost of the less costly candidate path used to discard other candidate

paths, as well as the use of intermediate circumferences. Moreover, different number of analysis radii and gap between them are tested. The different configurations, the number of vessel segments labeled for each expert and the classification agreement among them in each one are shown in Table 6.9.

Configuration	**Total segments**	**Expert$_1$**	**Expert$_2$**	**Expert agreement**(%)
A: 7 radii labeled by the experts	9383	9042	8599	97.82
B: 3 radii (1.5r, 2.25r and 3r)	6894	6654	6353	98.03
C: 4 radii (1.5r, 2r, 2.5r and 3r)	3926	3779	3587	97.49
D: the first 5 radii	5283	5091	4841	97.81
E: the last 5 radii	6610	6370	6038	97.61

Table 6.9: Number of detected vessel segments, number of the vessel segments that have been labeled by Expert$_1$ and Expert$_2$ and percentage of agreement among the experts in the different radius configurations in VICAVR-2 database.

- *β parameter.* At first glance, β parameter seems quite influential on the classification results because high values of this parameter allow us to join more vessels in branches. At the same time, this fact increases the probability of joining points that do not belong to the same vessel (compare Figures 6.7(a) obtained with $\beta = 1.8$ and Figure 6.7(b) with $\beta = 1.2$). Nevertheless, the experiments conducted in the whole dataset revealed a small influence of β. This can be observed in the Figure 6.8 where almost all ROC curves computed using different β values are overlapped. The best value for the β parameter for all configurations was 1.10. Therefore, we fixed this value for β and we analyzed the remaining parameters. Table 6.10 shows the classification accuracy for the different configurations.

- *Vessel tree segmentation algorithm.* The two vessel tree segmentation algorithms obtain similar results. Hence, we choose the first algorithm since it is faster, simpler and requires no parameter tuning.

- *Intermediate circumferences.* An increment of the error rate is observed in the most of cases with the inclusion of intermediate circumferences. This could be due to the fact that artificial points which can not belong to vessel tree are added and these

points can be the union points between vessel points from different vessels. However, they could increase the performance in case of larger gaps between the analysis radius, but, in this case, considering intermediate circumferences just increases the complexity of the problem.

- *Radius configuration.* Concerning the radius configurations, there are no significant differences in the accuracy, hence, the method is robust to distinct analysis radius. The C configuration is the most specific, although it identifies correctly fewer actual positives. In this case, this is the most appropriate configuration because it is preferable to label fewer vessels and produce fewer misclassifications. The number of radii used (four) and the analysis of distant segments can make that C obtains better results than other configurations, such as A or B. That is, selecting many close segments can decrease the performance due to the high variation of color along the vessel and the existence of large vessel pieces where the color is totally different from the rest of vessel.

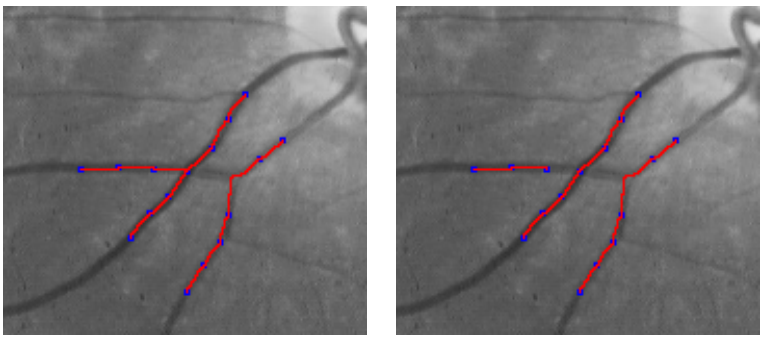

(a) (b)

Figure 6.7: Tracking results with $\beta = 1.8$ (a) and $\beta = 1.2$ (b). In both cases, the first segmentation algorithm was used together with radius configuration A and without intermediate circumferences.

Figure 6.9 shows the ROC curves achieved by the local clustering and including the vessel tracking with the first vessel tree segmentation algorithm, the C configuration and without intermediate circumferences. The vessel tracking post-processing increases the area under the ROC curve from 0.87 to 0.89 when arteries are considered the positives,

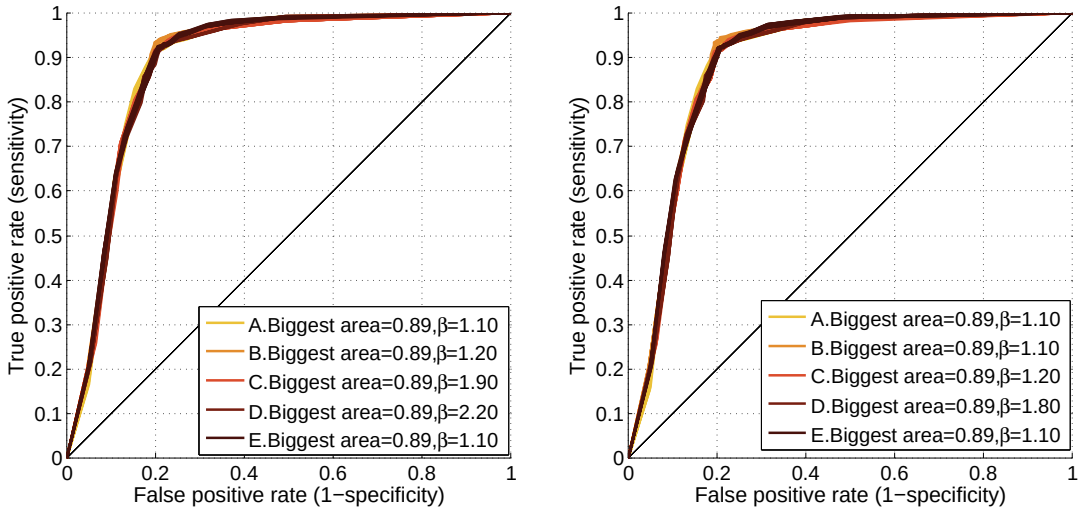

(a) (b)

Figure 6.8: ROC curves for vessel tracking classifier using different β values, radius configurations, the first segmentation algorithm, and including (a) or not (b) intermediate circumferences. The curves have been computed taking arteries as positives.

		No intermediate circ.						**Intermediate circ.**					
Config.	**Segment.**	$\text{Sens}_{\mathcal{V}}$	$\text{Spec}_{\mathcal{V}}$	$\text{Sens}_{\mathcal{A}}$	$\text{Spec}_{\mathcal{A}}$	AR	ER	$\text{Sens}_{\mathcal{V}}$	$\text{Spec}_{\mathcal{V}}$	$\text{Sens}_{\mathcal{A}}$	$\text{Spec}_{\mathcal{A}}$	AR	ER
A	I	76.76	93.56	89.48	80.15	83.50	13.24	76.86	93.23	89.12	80.05	83.36	13.46
	II	77.11	93.54	89.97	79.99	83.93	13.26	76.68	93.27	89.97	79.64	83.73	13.56
B	I	75.20	92.34	86.47	81.23	81.13	13.74	74.65	92.28	86.47	80.63	80.87	14.07
	II	74.23	92.77	85.65	80.81	80.24	13.85	74.47	92.50	86.09	80.02	80.58	14.27
C	I	73.70	94.52	87.27	82.07	80.87	12.32	73.70	94.20	87.64	81.66	81.06	12.63
	II	74.02	94.68	87.07	81.48	80.91	12.49	74.24	94.24	87.56	81.17	81.27	12.80
D	I	76.49	92.65	88.88	79.68	83.09	13.89	76.35	92.32	88.67	79.51	82.92	14.15
	II	76.83	92.62	88.94	79.44	83.29	13.98	76.49	92.32	89.15	79.48	83.24	14.12
E	I	76.71	92.90	89.08	79.91	83.31	13.65	76.89	92.78	89.18	79.87	83.44	13.70
	II	76.67	93.06	89.59	79.29	83.56	13.79	76.85	92.97	90.10	79.32	83.92	13.77

Table 6.10: Vessel classification accuracy in VICAVR-2 database using vessel tracking with different configurations of analysis radii, vessel tree segmentation algorithms and using or not intermediate circumferences.

or from 0.88 to 0.89 if the positives are the veins.

Table 6.11 summarizes the classification performance in VICAVR and VICAVR-2 databases obtained by the local clustering and including the vessel tracking procedure. In both cases, the median of the G component in the profile from the $MSR_{\sigma_1\sigma_2\sigma_8}$ output was utilized as classification feature. It is worth to point out that the difference in the accuracy between the databases are possibly related with the fact that a higher number of secondary vessels were classified by the experts in VICAVR-2. The color information of secondary veins is more similar to color of arteries than the color values of the main veins. In fact, in VICAVR, the specificity for arteries is high, whereas this value decreases in VICAVR-2. It is also worth noting that the accuracy rate is reduced using the vessel tracking post-processing since in case of tie in the number of vessel segments labeled as arteries and veins in the same vessel, all segments are not classified. Moreover, the error rate and the specificity are increased.

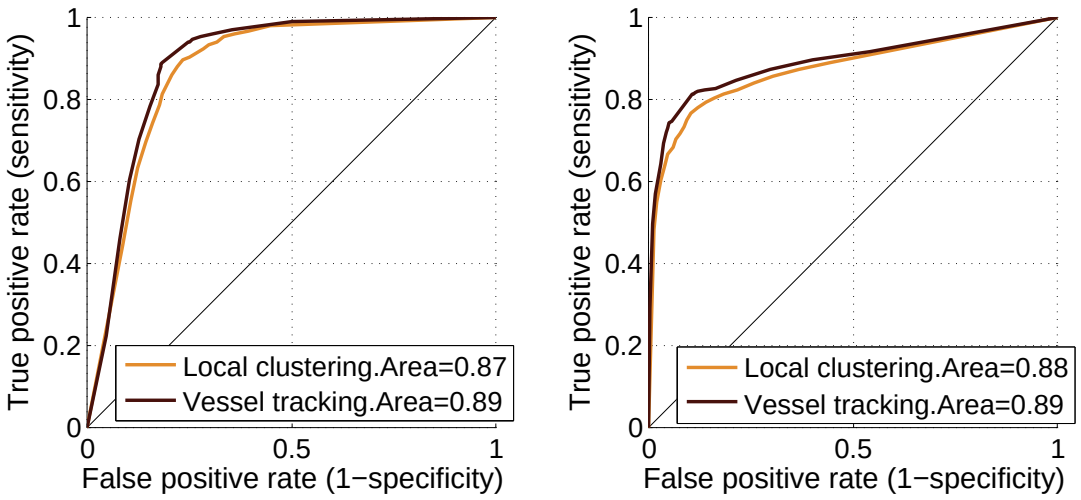

(a) (b)

Figure 6.9: ROC curves of Local clustering vs Vessel tracking in VICAVR-2 database taking as positives the arteries (a) and the veins (b). It was computed using different threshold probability values and considering the agreement among the two experts as the gold standard.

	Local clustering						Vessel tracking					
Database	$Sens_{\mathcal{V}}$	$Spec_{\mathcal{V}}$	$Sens_{\mathcal{A}}$	$Spec_{\mathcal{A}}$	AR	ER	$Sens_{\mathcal{V}}$	$Spec_{\mathcal{V}}$	$Sens_{\mathcal{A}}$	$Spec_{\mathcal{A}}$	AR	ER
VICAVR	91.25	88.63	88.02	92.31	89.74	9.49	93.46	90.76	89.95	95.58	91.82	6.77
VICAVR-2	75.13	89.80	89.00	77.15	82.45	16.40	73.70	94.52	87.27	82.07	80.87	12.32

Table 6.11: Accuracy rate using local clustering and vessel tracking in VICAVR and VICAVR-2 databases considering as gold standard the agreement among all experts.

Comparison with other techniques

It is difficult to make a comparison between the techniques of vessel classification found in the literature due to mainly different retinal databases are used. Table 6.12 summarizes the results obtained with our methodology and the results achieved by other techniques. Grisan and Ruggeri's method [79] gets a low percentage of miss-classifications, 12.4%, in 24 images, however the strict division in quadrants forces to unclassify a high number of vessels, 7.70%, and makes the labeling of a vessel very dependent on the vessel neighbors. The error rates obtained by Jelinek et al. [73] are high, around the 30% in a set of 8 images. Niemeijer et al. [80] achieved an area under the ROC curve of 0.88 in a set of 20 images, however the results are not comparable because they only take into account the main vessels whereas the problems arise with thinner vessels.

Technique	**Classification algorithm**	***ER***
Grisan and Ruggeri [79]	Fuzzy C-means	12.4%
H.F. Jelinek et al. [73]	Naïve-Bayes	31%
	Decision Table	30%
	J48	30%
Niemeijer et al. [80]	K-Nearest Neighbor	0.88 (ROC curve area)
Our method	Local clustering & Tracking	6.77% (VICAVR)
		12.32% (VICAVR-2)

Table 6.12: Vessel classification performance comparative among techniques found in the literature.

To make a more precise comparison with the methods above mentioned, we have analyzed these approaches in the VICAVR dataset. First, the method proposed by Grisan

et al. [79] is similar to the quadrant division strategy analyzed in this work using the feature vector made up of the mean of the H component and the variance of the R component in the profile. The error rate obtained in the VICAVR dataset using this configuration was 35.79% with a 16.16% of unclassified vessels.

We have also applied the methodology proposed by Jelinek et al. [73] to the VICAVR dataset. First, we applied a gross median filter to estimate the background of each channel and then we subtracted this estimation from the channel. Then, we use the normalized images to compute the features proposed by the authors, the mean and standard deviation of H, G, R and B color components in the profiles. The Correlation-based Feature Subset Evaluation method of Weka software [81] was applied to select the features. The features selected by this method in the VICAVR dataset were the mean and standard deviation of G, the standard deviation of R, and the standard deviation of H. These features, as well as the features selected in the Jelinek's et al. dataset have been tested with the proposed classifiers: Naïve Bayes, DecisionTable and J48 implemented in Weka using a 10-fold cross-validation. The classification error rate for our features was 34.85% with Naïve Bayes, 26.20% with the Decision Table and 22.81% using J48. The results using the features selected by the Correlation-based Feature Subset Evaluation method in authors' dataset, the mean of G and the mean and the standard deviation of H, were 35.18%, 32.37%, and 31.855% respectively. These results are similar to those achieved by Jelinek et al. in both cases.

Niemeijer et al. [80] tried Support Vector Machine (SVM) and k-Nearest Neighbor (kNN) classifiers. They found that the kNN provided the best performance. We only tested the SVM using a 5-5 fold cross-validation in VICAVR. To this end, we have analyzed a big set of features similar to those used by the authors except for the steerable filters. These features consist of color features (the mean and the median of profile values in each component of the RBG and HSL color spaces, the central value of the profile, the mean and the median of centerline values, the percentiles 10, 20, 90 and 80 in the profile...), contrast features (the standard deviation of the profile and centerline values for the mentioned color components), shape features (skewness and kurtosis of the profiles) and quality features

(the caliber of the vessel, the features previously mentioned normalized by their value in the image or normalized by the caliber of the vessel). Before classifying the feature vectors with SVM, several feature selection methods of the Weka toolbox as well as the library mRMR for Matlab which combines the Max-Relevance and Min-Redundancy criteria have been applied. The best classification error rate was 21.46% and it was achieved with 12 features selected by the Correlation-based Feature Subset Evaluation method. We also tried the retinex image enhancement with SVM. In this case, the lower error rates were achieved with 14 features selected by Correlation-based Feature Subset Evaluation method, 19.21%, and with 10 features obtained by the mRMR, 20.63. In addition, in order to improve the results, we applied a voting system for vector features which belong to the same vessel segment, in the same manner that in the proposed method. This improves the performance, obtaining an error rate of 17.62% using retinex and the 3 features selected by mRMR from the retinex output image.

As a conclusion, the best performance in VICAVR database was obtained with the approach proposed in this thesis.

6.2.4 AVR computation methodology

The aim of this section is to compare the AVR measurements achieved automatically with the proposed methodology and with the AVR monitoring system regarding the AVR estimations supervised by medical experts. In this manner, first, we show the experiments carried out to obtain the rules which emulate the vessel selection made by medical experts. Second, the proposed AVR monitoring system is tested. In both cases, the AVR is computed by the ratio between the averages of artery and vein vessel widths.

Vessel selection

The hypothesis made in Chapter 4 about the vessel selection rules employed by the medical experts are evaluated in this section using a subset of 86 images randomly selected from POSTEL database. To this end, we compare the AVR computed with different vessel

selection methods respect the the AVR gold standard obtained using the automatic mode of the SIRIUS system under the supervision of two ophthalmologists. The SIRIUS system estimated the AVR taking into account all detected vessel segments, however the experts could remove the vessel segments which they consider unsuitable for the computation. Moreover, they could also change an incorrect location of the optic disc or correct wrong artery/vein classifications.

In order to find the best vessel selection method, all possible combinations of hypothesis with all their implementations were considered to compute the the AVR automatically. This involved testing 649 combinations of hypothesis. A statistical analysis has been performed to compare the AVR values obtained by each expert, denoted by $Expert_1$ and $Expert_2$, with the value computed by the system using a specific combination of hypothesis C, $System_C$. Moreover, the agreement among the experts is also analyzed. Thus, a two-sided hypothesis test on Pearson's correlation coefficient as well as, a two-sided Welch's t-test have been conducted.

A Pearson's correlation coefficient of 0.7981, as well as, a significant test with null hypothesis in the form $H_0 : \rho_{Expert_1,Expert2} = 0$ indicate satisfactory correlation among experts (Table 6.13). This correlation increases if only the 6 main arteries and veins are taken into account. Moreover, the p-value of the Welch's t-test ($H_0 : \mu_{Expert_1} - \mu_{Expert_2} = 0$) reveals the AVR's supervised by the experts are equal in average.

Regarding the comparative between each expert and the system, only the most significant values are shown in Table 6.13. It shows the three highest Pearson's correlation coefficients when the Welch's t-test resulted non significant. Figures 6.10 and 6.11 show dispersion and boxplot graphs of the AVR estimated by the different experts, including the system. The results demonstrate that the system provides an estimation of the AVR close to the estimation measured by medical experts in a quite large data set.

In general, the best options for the vessel selection algorithm are those which implement the H1 (ruling out over- or sub-estimated vessel segments), H5 (deleting thin vessels), and H2 (removing vessel segments found over a bifurcation or a crossover) hy-

	Pearson's correlation coefficient	**Pearson's test p-value**	**Welch's t-test p-value**
Expert_1 vs Expert_2	0.7981	$< 2.2e-16$	0.2496
Expert_1 vs $\text{System}_{\text{H1H5}}$	0.7466	$< 2.2e-16$	0.8641
Expert_2 vs $\text{System}_{\text{H1H5H2}}$	0.7466	0	0.0138
Expert_2 vs $\text{System}_{\text{H1H5}}$	0.7860	0	0.34
6 main vessels			
Expert_1 vs Expert_2	0.8546	$< 2.2e-16$	$< 2.2e-16$
Expert_1 vs System	0.7472	$< 2.2e-16$	0.6036
Expert_2 vs System	0.7161	$9.104e-15$	0.3464

Table 6.13: Automatic AVR accuracy using different vessel selection options.

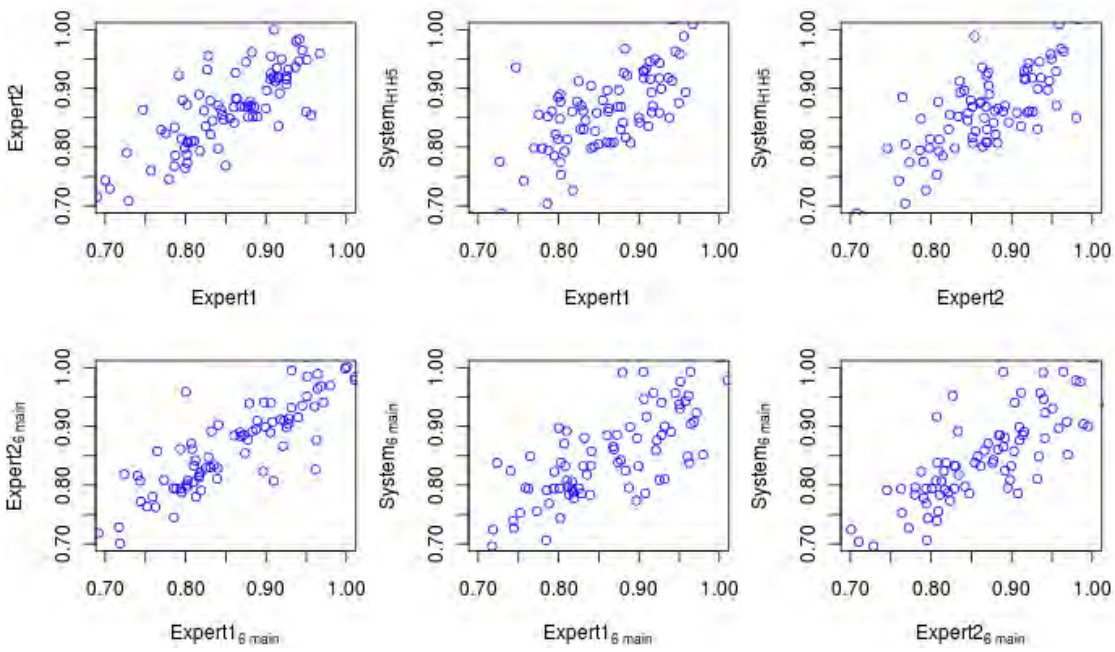

Figure 6.10: Dispersion graphs that show the dependence between the AVR measured by different experts.

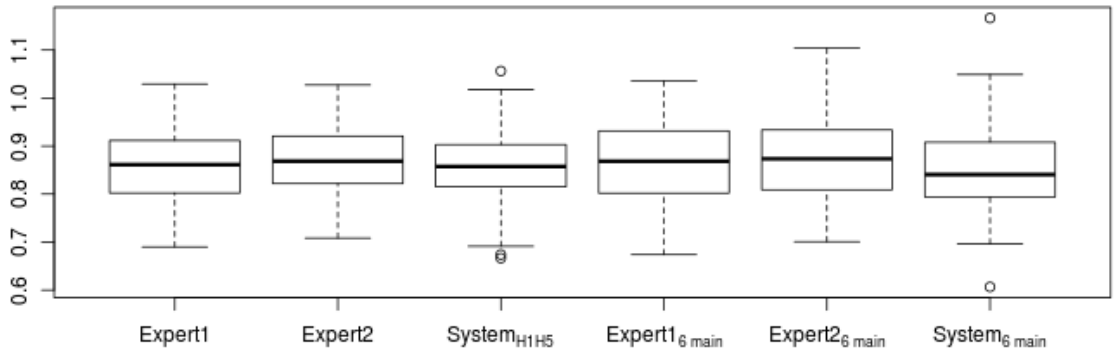

Figure 6.11: Boxplot of AVR values estimated by different experts. $System_{H1H5}$ denotes the most correlated AVR between both experts and the system.

pothesis. Hypothesis H5 has two different implementations but the correlation results were similar. The best results were obtained eliminating those arteries and veins whose width is smaller than the 10-percentiles computed for each class. In addition, if we only take into account the 6 main vessels, the correlation between each expert and the system is lower. Thus, this analysis shows that the vessel selection has a high influence on the AVR value.

AVR monitoring system

The monitoring system was tested in a subset of 89 patients taken from the 96 patients of the POSTEL database. The patients considered were those who have at least two images, the basal and the image acquired after six months of treatment. Hence, 158 pairs of images taken before and after treatment have been used in the experiment.

To evaluate the AVR monitoring system, each image taken at month 0 was considered the reference image and its AVR value graded by the expert represents the AVR reference. From this reference value, the system obtained the AVR in the image taken at month 6 and this result was compared with the AVR graded by the expert in the same image.

A statistical analysis has been performed to test if the monitoring system behaves like an human expert, that is, if the AVR values obtained by the expert and the monitoring system are similar, despite using different vessels for the estimation. The AVR obtained by the monitoring system in the images taken at month 6 is denoted by $AVR_{6MMonitoring}$, whereas, $AVR_{6MExpert}$ represents the value measured by the medical expert. A two-sided hypothesis test on Pearson's correlation coefficient ($H_0 : \rho_{AVR_{6MMonitoring},AVR_{6MExpert}} = 0$), as well as, a two-sided Welch's t-test ($H_0 : \mu_{AVR_{6MMonitoring}} - \mu_{AVR_{6MExpert}} = 0$) have been conducted. The first test provides evidence of correlation by means of a p-value less than $2.2e^{-16}$ and a Pearson's correlation coefficient of 0.61 as Table 6.13 shows. Moreover, the result of the second test with a p-value of 0.20 reveals the AVR values are equal in average. However, these values are increased to 0.92 and 0.89, respectively, in case of reducing the dataset to the 90 images with the lowest differences between the AVR values. This increment in the correlation can be also appreciated in the dispersion graphs of the Figure 6.12.

Images	**Configuration**	**Pearson's correlation coefficient**	**Pearson's test p-value**	**Welch's test p-value**
158	-	0.616	$< 2.2e^{-16}$	0.209
133	$\lvert AVR_{6MMonitoring} - AVR_{6MExpert}\rvert < 0.1$	0.796	$< 2.2e^{-16}$	0.833
90	$\lvert AVR_{6MMonitoring} - AVR_{6MExpert}\rvert < 0.05$	0.921	$< 2.2e^{-16}$	0.899

Table 6.14: AVR monitoring system accuracy. Hypothesis test results between the AVR values obtained by the medical expert and the system in the images taken after 6 months of treatment.

If we analyze the 25 images which present the highest AVR difference between expert and system ($\lvert AVR_{6MMonitoring} - AVR_{6MExpert}\rvert \geq 0.1$) we derive the following assumptions:

- The number of vessels taken into account to compute the AVR differs greatly from the image graded by the expert to the image measured by the monitoring system. This occurs mainly because the expert has selected a different number of vessels at months 0 and 6 as Figure 6.13 shows, or because the system does not detect some vessels at month 6 due to the image quality.

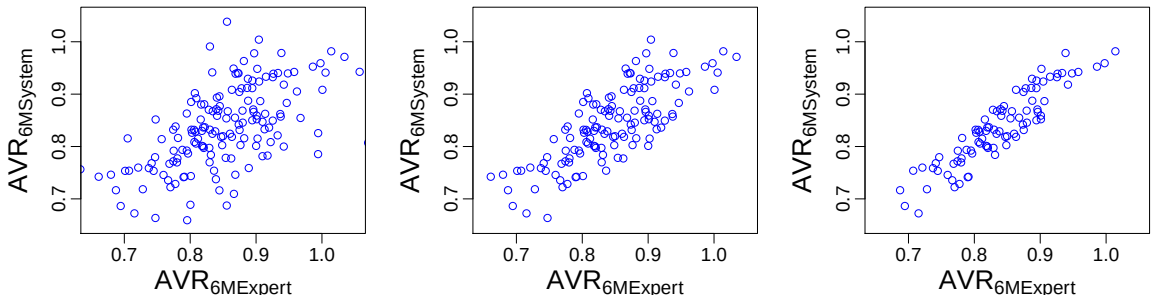

(a) (b) (c)

Figure 6.12: AVR monitoring system accuracy. Dispersion graphs which show the dependence between the AVR measured by the medical expert and the system in (a) the whole dataset of 158 images or in (b) 133 and (c) 90 images result of eliminating the images with AVR differences higher or equal to 0.1 and 0.05, respectively.

- In other cases, it seems that the AVR value is different because the expert has selected a very characteristic vessel (wide or narrow) with a huge influence in the AVR in only one of the images (Figure 6.13).

- Moreover, an incorrect snake deformation is also possible, resulting in an under- or overestimation of the vessel width in one image whereas the width was properly measured in the other image.

Improvement of vessel detection To prevent the removal, the measurement method is modified, so each time a snake is invalidated, it is thrown again, using as seed point a pixel located in the 8-neighborhood of the initial seed. In case of any of the 8 possible seeds produces an enclosed snake, the snake is definitely invalidated. Pearson's correlation coefficient in the 158 images increases slightly to 0.6329 while the p-value of the mean difference test remains the same, 0.209. At this point, this solution was incorporated in the method.

However, most of the missing vessels in the new sample image are lost because their centerlines are not detected because the image quality. In order to detect a greater number of vessels, the MLSEC-ST parameters are modified. These parameters are optimized to

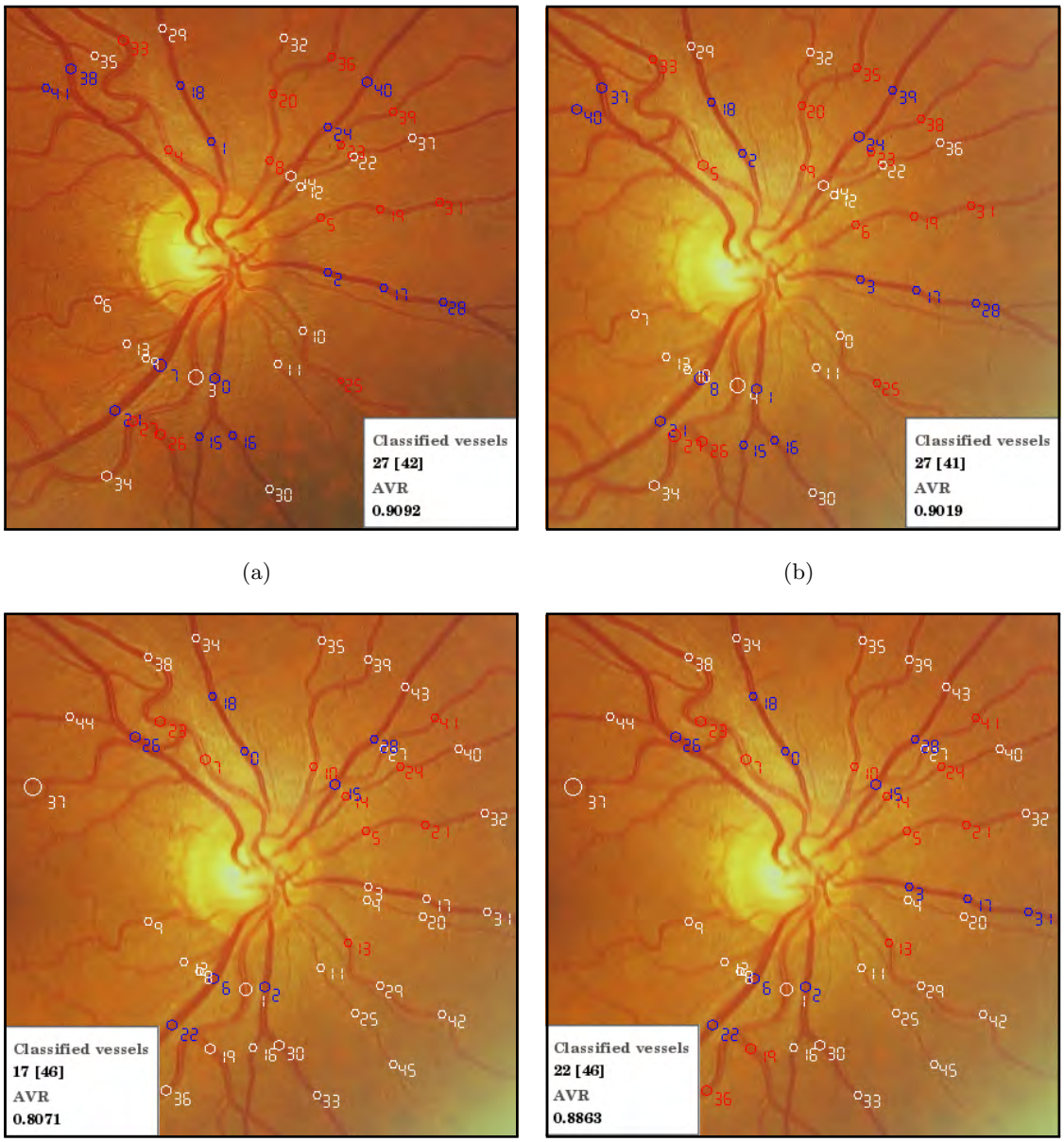

(a) (b)

(c) (d)

Figure 6.13: Influence of the vessel segments selected by the expert in the AVR obtained in POSTEL images. AVR computed (a) by the expert in the reference image at month 0, (b) by the monitoring system in the image taken at month 6 using the vessel segments selected in (a), (c) by the expert in the image taken at month 6 and, (d) using the result (c) but labeling two heavy vessels, one artery (19 and 36) and one vein (3, 17 and 31) which have not been considered by the expert in the image taken at month 6 but, they were selected in the reference image. Red points represent arteries, blue points are veins and white points, unclassified vessels.

avoid false positives, but, since the vessel positions are known in the new sample image, we can be less restrictive. Despite the change, the correlation value is reduced to 0.6325. This could happen because these parameters have a high influence on the vessel widths since the length of the vessel segments depends on them. Hence, the correlation can decrease because we compare widths obtained with different parameter values.

To test the influence of the third assumption, we remove from the new AVR the vessels whose widths differ more than 1/3 from them corresponding widths measured in the reference image. The Pearson's correlation coefficient increases a bit to 0.6389, but the results are more different in mean with a p-value of 0.127. This could be due to an increment of the difference between the vessel sets.

The influence of the vessels selected by the expert To test the influence of the vessels selected by the expert in the images at months 0 and 6, the AVR values at month 6 are recalculated taken into account only the vessel segments labeled in common by the expert at month 0 and 6. Both, the AVR system and the computed by the expert must be recalculated.

The matching of two vessel segments in the images at months 0 and 6 is successful if they belong to the same circumference and the angles formed by each vessel and the x-axis are similar. Thus, given the two lines connecting the middle point of each vessel segment with the optic disc center, we calculate the angle formed by each line and the x-axis. If the difference between the angles are smaller than a preestablished threshold, the vessel segments coincide. Moreover, we only take into account those pairs of images with, at least, 4 veins and 4 arteries selected by the expert in order to discard those cases with few vessel segments in common. Thus, in a dataset of 125 images, the Pearson's correlation coefficient was 0.87 and the p-value of the mean difference test was 0.85.

Computation times

The average computation times to calculate the reference AVR and a new AVR obtained with the vessel registration method were 6.57 and 7.42 seconds, respectively. We have performed the test in an Intel Pentium Core 2 Duo 2.4GHz and 4GB of RAM runnig GNU/Linux Debian, over the 158 pairs of images of the POSTEL database.

6.3 Clinical validation

The proposed AVR methodology included in the web-based Sirius system was used in the clinical studies POSTEL [125] and VAMPAHICA [128] related to the assessment and diagnosis of hypertension.

6.3.1 POSTEL study

Pose et al. [125] validated clinically the semiautomatic method for the AVR computation integrated in the SIRIUS system. The method was applied to the POSTEL database by the supervision of two graders.

The method was compared with a previous developed system validated clinically, the ART-VENA [67]. First, the sensitivity and the false positives in the vessel detection achieved with both methods were computed in a representative subset of 21 images from POSTEL dataset. The new method increases the sensitivity respect ART-VENA from 84.6% to 89.5% reducing also the false positives from 8% to 1%.

After that a statistical analysis has been carried out over the whole dataset, although separating into two groups according to the place of origin of the images, Santiago de Compostela, and Coruña. The average and standard deviation of AVR's were 0.7805 ± 0.0610 for the patients of Coruña and 0.7813 ± 0.0666 for the group of Santiago de Compostela. The Cronbach's α with the interclass correlation coefficient were 0.974 and 0.949 for the group of Santiago; whereas 0.9223 and 0.8557 are the values for Coruña. Thus, two

methods are highly correlated.

In other work related to POSTEL study, Pena-Seijo et al. [129] showed an AVR growth after six months of antihypertensive treatment with Telmisartan in 139 hypertensive patients the POSTEL database. In the right eye, the AVR increased from 0.7676 ± 0.0589 to 0.8149 ± 0.056, whereas the rise in the left eye was from 0.7748 ± 0.062 to 0.8143 ± 0.061. Moreover, considering the averages of the arteriolar and venular widths separately, they proved a significant increase ($p < 0.001$) of the arteriolar width in both eyes. On the contrary, the venular width did not suffer any variation.

6.3.2 VAMPAHICA study

Coll de Tuero et al. [130] analyzed if the AVR evolution in newly diagnosed hypertensive patients is associated with better or worse outcomes of target organ damage (TOD) during a one-year follow-up.

The VAMPAHICA patients included in this study were those who fulfill the following criteria: aged 15-75 years; hypertension defined as the average of blood pressure (BP) readings, separated by two minutes, taken in three different readings, with values $\geq$ 140mmHg and/or $\geq$ 90mmHg; recently diagnosed hypertensive patients who never received any treatment for hypertension and patients who provided corrected self-blood pressure measurement (SBPM) and ambulatory BP monitoring (ABPM).

Exclusion criteria were the following: inability, in the health professional's opinion, to perform SBPM; diabetes mellitus; secondary hypertension; previous cardiovascular disease; renal insufficiency (serum creatinine $>$ 2mg/dL); liver insufficiency; alcoholism or severe psychiatric disease; endocrine or severe hematological disease, or other severe diseases or limitations which, in the physician's opinion, were a reason for exclusion.

Hence, a total of 133 patients from VAMPAHICA database with 59% proportion of mens and ages in 57 ± 10.7 were analyzed.

Several variables were analyzed, among them: age, gender, systolic and diastolic clinic

blood pressure (CBP), systolic and diastolic self-blood pressure measurement (SBPM), systolic and diastolic ABPM-day, total cholesterol, left ventricular hypertrophy (LVH) by electrocardiographic criteria, urinary albumin excretion rate (UAER), glomerular filtration rate (GFR), advanced lesions in fundus occuli (FO) and antihypertensive treatment at each follow-up visit... Among these variables, LVH, advanced lesions in FO, low estimated GFR, and high UAER were considered TOD.

The AVR values in both eyes, at baseline and at 1-year follow up, were estimated using the SIRIUS system. Baseline AVR at each eye was computed automatically without user supervision, whereas the final AVR was computed from the baseline AVR using the AVR monitoring method. In this case, the AVR values were computed as the ratio between the arteriolar and venular median widths to avoid any influence of outliers. The final baseline and 1-year follow-up AVR values were obtained as the average of the two eye measurements. Due to image quality of several images in the VAMPAHICA database, the Foracchia et al's contrast image enhancement described in the Appendix B was applied before the vessel detection.

The baseline and final values of the variables in study were analyzed stratifying or not the AVR and the difference between final and baseline AVR (AVR_{dif}) by quartiles.

Several statistical tests have been conducted including a Chi-squared test to analyze the association between the good TOD evolution and the quartiles of the AVR and the AVR_{dif} values. Also the relationship between the fourth quartile of the AVR_{dif} and the good TOD evolution was adjusted by means of logistic regression. To this end, LVH, advanced lesion in FO, GFR and amount of TOD constituted the response variables.

The AVR baseline stratification in quartiles was: $Q_1 < 0.772$, $Q_2 : 0.772 - 0.833$, $Q_3 : 0.833 - 0.901$ and $Q_4 > 0.90$. On the contrary the quartile stratification for the AVR_{dif} was: $Q_1 < -0.068875$, $Q_2 : -0.068875 - 0.017$, $Q_3 : 0.017 - 0.081750$ and $Q_4 > 0.081750$.

The most promising results were the good evolution of TOD and the amount of TOD (the number of TOD remained unchanged (if pre-existing) or increased) respect the baseline AVR quartiles as Table 6.15 shows. Advanced lesions in the FO is inversely associated

with the higher baseline quartiles, whereas, there is a direct trend between the amount of TOD and the higher baseline quartiles.

No trend has been found between any TOD or amount of TOD and the AVR_{dif} quartiles, as it is shown in Table 6.16. However, there is a trend to a better evolution of LVH (p-value = 0.07) and the amount of TOD (p-value = 0.04) when the upper quartile (Q_4) is compared with the lower ones ($\leq Q_3$).

Moreover the results of multivariate analytical models to see the good evolution of TOD according to AVR_{dif} demonstrated that patients with an increase in the Q_4 quartile of AVR_{dif} show a good evolution of LVH and amount of TOD.

	Q_1 $n = 33$	Q_2 $n = 33$	Q_3 $n = 34$	Q_4 $n = 33$	p-value for trend	Q_4 vs $\leq Q_3$
High UAER n(%)	32 (97.0)	32 (97.0)	32 (94.1)	32 (97.0)	0.742	ns
LVH n(%)	25 (75.8)	23 (69.7)	24 (70.6)	27 (81.8)	0.562	ns
FO advanced lesions n(%)	32 (97.0)	31 (94.0)	31 (91.2)	29 (88.0)	< 0.001	< 0.001
Amount of TOD n(%)	32 (97.0)	31 (94.0)	31 (91.2)	29 (88.0)	< 0.001	< 0.001

Table 6.15: Evolution of TOD according to AVR baseline quartiles.

	Q_1 $n = 33$	Q_2 $n = 33$	Q_3 $n = 34$	Q_4 $n = 33$	p-value for trend	Q_4 vs $\leq Q_3$
High UAER n(%)	33 (100.0)	31 (91.2)	31 (93.9)	33 (100.0)	0.921	ns
LVH n(%)	24 (72.7)	26 (76.4)	20 (60.6)	29 (87.9)	0.658	0.07
FO advanced lesions n(%)	24 (72.7)	26 (76.4)	20 (60.6)	29 (87.9)	0.658	0.07
Amount of TOD n(%)	27 (81.8)	30 (88.2)	28 (84.8)	33 (100.0)	0.171	0.04

Table 6.16: Evolution of TOD according to the quartiles of difference between final and baseline AVR.

6.3.3 Current studies

Currently, several studies are underway to analyze the relation between the AVR and diverse pathologies making use the SIRIUS web application. Among them, it is worth mentioning the following projects:

- *Association between retinal microcirculation and macrocirculation.* A project funded by the Spanish Ministry of Science and Innovation to analyze the association between the microcirculation in the retina and the macrocirculation through an automatic processing of carotid images. This study is conducted by the VARPA group in collaboration with the Research Unit of the Institut d'Assistència Sanitària, IAS, Girona; the CIBER of Epidemiology and Public Health, CIBERESP; the Research Group on Statistics, Econometrics and Health (GRECS), University of Girona in Spain; the Service of Internal Medicine of Conxo Hospital, Santiago de Compostela in Spain and the Instituto de Engenharia Biomédica of the University of Porto in Portugal.

  Several steps have been already taken in this direction. An automatic method for the intima-media thickness measurement on carotid ultrasound as well as a semi-automatic method for the AVR computation, both developed by the Instituto de Engenharia Biomédica of the University of Porto, were translate to C++ programming language and incorporated to a web application similar to SIRIUS system in order to correlate both measurements with other patients' variables [131].

- *Association between retinal and cerebral microcirculations* Another study worth mentioning is the analysis of relation between the retinal and cerebral microcirculations, through the AVR measurements in Alzheimer patients. This study is conducted by the VARPA group in collaboration with the Research Unit of the Institut d'Assistència Sanitària, IAS, Girona; the CIBER of Epidemiology and Public Health, CIBERESP and the Research Group on Statistics, Econometrics and Health (GRECS), University of Girona in Spain.

Chapter 7

Conclusions

The aim of this work is to develop an automatic methodology to compute the *arterio-ovenous ratio* (AVR) in retinal images in order to assess the alterations in arteriolar and venular vessel widths caused by different diseases. The AVR has been related with several pathologies such as diabetes, metabolic syndrome, hypertension or heart failure.

This work focuses on analyzing the relation between the AVR and the hypertension. The primary response of the retinal vessels to systemic hypertension is the arteriolar narrowing which characterizes the grade I of hypertension retinopathy. However, the difficulty to obtain a precise and reliable quantitative measure of the generalized narrowing prevents the correlation of the grade I of the hypertensive retinopathy with hypertension. In this work, we present an extensive characterization of the hypertension retinopathy as well as the need to develop reliable methods to measure the arteriolar narrowing through the AVR in order to stratify the cardiovascular risk associated to hypertension.

The method proposed to compute the AVR is fully automatic. The AVR is estimated as the ratio between artery and vein widths measured in several circumferences centered at the optic disc. Hence, the optic disc is located with a method based on the DoG filtering and the Hough transform whereas the centerlines of vessels segments in the circumferences of analysis are detected by the MLSEC-ST operator. According to the validation tests performed, the following remarks can be made. On one hand, the approach

used for the optic disc location is good for healthy images but it presents limitations in some ailing retinas because its basis is the detection of brightest areas with large number of centerlines. However, unhealthy images can present shining zones which do not correspond with the optic disc and where false positive centerlines are more likely. On the other hand, in POSTEL study, the vessel detection has been compared with ART-VENA, a semiautomatic method for the AVR computation clinically validated. The proposed approach improved the sensitivity and reduced the false positive vessels achieved with ART-VENA in a database composed of images acquired at two different centers.

The vessel width measurement method is based on deformable models initialized at the centerline vessels detected in the previous step. The evaluation of the method made in the REVIEW public database indicates that the method is comparable and, in some cases, overcomes the performance achieved by other techniques. However, REVIEW images with high central light reflex and JPEG compression cause diffuse edges which evinced limitations in the Canny edge detector. The main drawback of the method is the treatment of the high resolution images with strong central light reflex, in which the centerline and edge detectors can interpret one vessel as two different vessels. This phenomenon does not appear if the image is reduced. Therefore, a preprocessing step to locate the central light reflex would improve the method.

The vessel classification into arteries and veins combines a local clustering using the K-means algorithm and a vessel tracking based on the minimal path approach. This step is one of the main contributions of this work. The local clustering approach allows to mitigate the effect of the uneven lightness in the classification, whereas the tracking procedure provides a way to ensure the class of a vessel taking into account the color information along the vascular structure. Other unsupervised and supervised classification methods in combination with several feature vectors have been tested and the proposed approach demonstrated to be the best for the large dataset used.

An algorithm to select the set of suitable vessels segments for the AVR calculus which emulates the selection made by medical experts is also proposed. On one hand, the experiments carried out to test the AVR computation with different sets of vessel segments have

demonstrated that the method provides an estimation of the AVR close to the estimation measured by medical experts in a quite large dataset. On the other hand, the experiments have made evident the high influence of the selected vessels in the calculus, and the need of estimating the AVR using the same set of vessels for a patient. This finding was also previously reported by Knudtson et al. [4] who realized that the Hubbard's formulas were dependent on the number of selected vessels so they propounded a reformulation using only the six main arteries and veins.

Moreover, a novel method based on vessel registration is presented in order to compute the patient's AVR at different images acquired over time using the same set of vessel measured at the same points. This AVR monitoring is another main contribution of this work providing a valuable and reliable assessment of the vessel width evolution. The correlation obtained between the AVR computed by monitoring system and an expert at six month follow-up images revealed that the system behaves almost like another medical expert.

The AVR computation methodology as well as the monitoring system were integrated in the SIRIUS web application. The clinical studies and experiments made throughout this work demonstrated that the system offers a perfect collaborative environment for physicians and researchers of different centers.

The system's usefulness was verified with the clinical validations made in the POSTEL and VAMPAHICA studies with images acquired at different health care centers and distinct retinal cameras. The former showed an increment in the AVR and in the arteriolar average width of hypertensive patients after six months of treatment. The latter revealed an increment in the AVR in the highest quartile at the end of one year follow-up were left ventricular hypertrophy and amount of target organ damage experienced a favorable outcome. Although the amount of target organ damage has not yet been definitely shown as a prognostic indicatorfactor, greater cardiovascular risk risk has been described in patients with a higher amount of target organ damage.

7.1 Further work

The usefulness of the SIRIUS system and the AVR methodology was demonstrated in this thesis, however tools for image analysis in the medical field should be continuously improving and adapting to the needs and trends of the moment as well as to new datasets.

Regarding the proposed AVR methodology, the following improvements could be considered. In the optic disc detection, methods to measure the vessel convergence could be included in the proposed OD detection approach to avoid its limitations in case of unhealthy retinal images. Moreover, in the vessel detection, other boundaries detection techniques could be tested in order to improve the performance in case of diffuse edges. The use of a bilateral filter in the noise reducing step of Canny edge detector could prevent the offset in edges caused by the Gaussian filtering. Furthermore, an algorithm for the identification or filtering of the central light reflex could also improve the vessel detection method.

One of the goals should be to become SIRIUS system in a complete retinal analysis tool. In addition to the modules developed in this work, SIRIUS has algorithms for the automatic detection an evolution of the microaneurysms related to diabetic retinopathy as well as for the measurement of the vessel tortuosity. It would be advantageous including in SIRIUS more modules for recognizing other fundus image alterations such as arteriovenous nicking, hard and soft exudates, papilledema or macular degeneration among others. Furthermore, more patient's clinical variables associated to different pathologies of study could also be incorporated in order to correlate the automatic measures derived from the retinal images with the clinical ones.

From a clinical standpoint, further studies are needed with more patients and for a longer follow-up period to definitively establish the AVR as prognostic indicatorfactor in hypertension and can stratify the cardiovascular risk. Moreover, it would be interesting to propose other studies to analyze the relationship between the retinal microcirculation and other diseases, taking advantage of the direct observation of retinal vessels and the capabilities offered in this work.

Appendix A

MLSEC-ST operator

This Appendix is devoted to explain the operator *Multilocal Level Set Extrinsic Curvature* enhanced by the *Structure Tensor* (MLSEC-ST) proposed by Lopez et al. in [44].

Given a function $L : \Omega \subset \mathbb{R}^d \rightarrow \mathbb{R}$, the set points $S_l = \{x \in \Omega | L(x) = l\}$ is the *level set* associated to a constant l. In 2D ($d = 2$), L can be thought of as a topographic relief whose level curves constitute the mentioned level sets. Moreover, a discrete image can be defined as the sampling of a d-dimensional continuous function $L : \Omega \subset \mathbb{R}^d \rightarrow \Gamma \subset \mathbb{R}$.

As Figure A.1 shows the curvature extrema of the level curves forms connected curves called vertex curves, which mark the top of ridges and bottoms of valleys in the image, that is, the creases [132]. Specifically, negative minima of the level curve curvature (m^-), level by level, form valley-like curves and positive maxima (M^+), ridge-like curves. Thus, in [132, 133] the definition of crease implies to find the zeros of the directional first derivative of the level curve curvature as follows:

$$\nabla\kappa \cdot \mathbf{v} = 0, \begin{cases} \mathbf{v}^t \cdot \nabla\nabla\kappa \cdot \mathbf{v} < 0 & \text{and} \quad \kappa > 0 \quad \text{for ridges} \\ \mathbf{v}^t \cdot \nabla\nabla\kappa \cdot \mathbf{v} > 0 & \text{and} \quad \kappa < 0 \quad \text{for valleys} \end{cases} \tag{A.1}$$

where t means transpose, $\cdot$ represents the matrix product, κ is the level set curvature, $\mathbf{v}$ the level curve tangent, the operators $\nabla = (\partial/\partial x^1, \ldots, \partial/\partial x^d)$ and $\nabla\nabla = (\nabla^t\nabla)$ designate the gradient and the Hessian of a function, respectively.

For d-dimensional images, level curves have to be generalized to level sets. In general, a

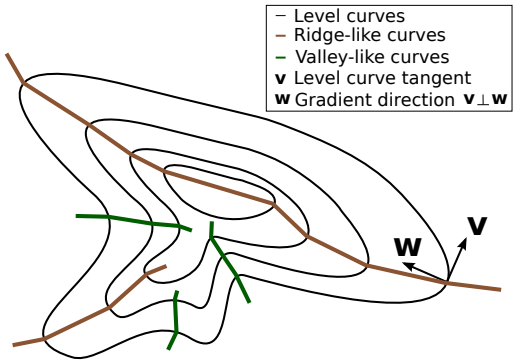

Figure A.1: Crease curves (ridges and valleys) as the loci of extrema of the level-curve curvature κ.

level set, S_l, can be defined as $(d-1)$-dimensional hypersurfaces on Ω. Each $x \in \Omega$ belongs just to one of these hypersurfaces, defined implicitly by $F(y) = L(y) - L(x) = L(y) - l = 0$. Thus, Lopez et al. [44] reformulate the *level definition* [133] of creases for d-dimensional images as follows: Let $|\xi_1| \geq \cdots \geq |\xi_d|$ be the *principal curvatures* of the level hypersurface passing through $\mathbf{x}$, with $\mathbf{t}_1, \ldots, \mathbf{t}_d$ their corresponding *principal directions*. Then, $\mathbf{x}$ is an r-dimensional crease if

$$\forall_i \in \mathcal{I}_{d-r} \quad \nabla\xi_i \cdot \mathbf{t}_i = 0, \begin{cases} \mathbf{t}_i^t \cdot \nabla\nabla\xi_i \cdot \mathbf{t}_i < 0 & \text{and} \quad \xi_i > 0 \quad \text{if ridge} \\ \mathbf{t}_i^t \cdot \nabla\nabla\xi_i \cdot \mathbf{t}_i > 0 & \text{and} \quad \xi_i < 0 \quad \text{if valley} \end{cases} \tag{A.2}$$

According to tensorial calculus, the LSEC can be expressed in terms of the derivatives of L as follows:

$$\kappa_d = (L_\alpha L_\beta L_{\alpha\beta} - L_\alpha L_\alpha L_{\beta\beta})(L_\gamma L_\gamma)^{-\frac{3}{2}}, \quad \alpha, \beta, \gamma \in \mathcal{X}_d \tag{A.3}$$

For $d = 2$ and using Cartesian coordinates, the level curve curvature is obtained as:

$$\kappa = \kappa_2 = (2L_x L_y L_{xy} - L_y^2 L_{xx} - L_x^2 L_{yy})(L_x^2 L_y^2)^{-\frac{3}{2}} \tag{A.4}$$

where

$$L_\alpha = \frac{\partial L}{\partial \alpha}, \quad L_{\alpha\beta} = \frac{\partial^2 L}{\partial \alpha \partial \beta}, \quad \alpha, \beta \in \{x, y\} \tag{A.5}$$

Even though in theory, the LSEC is a good creaseness measure, in practice, its local definition makes it inappropriate for discrete domains. LSEC does not fulfill the continuity

and homogeneity properties expected. It contains discontinuities at the center of elongated objects and takes different values.

To avoid the lack of continuity and homogeneity of LSEC in discrete domains, Lopez et al. [44] proposed the MLSEC operator as creaseness measure. In 2D, the level curve curvature, κ, can be defined through the orthogonal relationship between level curves and the slope lines which integrate the gradient vector $\mathbf{w}$. This orthogonality implies a connection between the level curve curvature and the degree of parallelism of the slope lines. That is, when the level curves are parallel and straight lines, the slope lines are also parallel and straight, whereas if level curves bend, the slope lines diverge/converge. Thus, using the divergence operator which measures the degree of parallelism, the level set curvature can be defined as follows:

$$\bar{\kappa}_d = -\mathrm{div}(\bar{\mathbf{w}}) \tag{A.6}$$

where $\bar{\mathbf{w}}$, the normalized gradient vector field, is defined as:

$$\bar{\mathbf{w}} = \begin{cases} \mathbf{w}/\|\mathbf{w}\| & \text{if } \|\mathbf{w}\| > 0 \\ \mathbf{0}_d & \text{if } \|\mathbf{w}\| = 0 \end{cases} \tag{A.7}$$

In the 2D case, let $\mathbf{x}$ be a point where the divergence of a 2D vector field $\mathbf{u}$ has to be computed. Let $\mathcal{C}$ a simple closed curve in $\mathbb{R}^2$, parameterized by ℓ, which encloses the point $\mathbf{x}$; let $\mathbf{n}$ be its unitary normal vector and ω the area enclosed by $\mathcal{C}$. Then, the divergence of $\mathbf{u}$ at $\mathbf{x}$ can also be defined as:

$$\mathrm{div}(\mathbf{u}) = \lim_{\omega \to 0} \frac{1}{\omega} \int_{\mathcal{C}} \mathbf{u}^t \cdot \mathbf{n} d\ell \tag{A.8}$$

This definition can be generalized for any dimension d, assuming that $\mathcal{C}$ is a $(d-1)$-dimensional simple closed boundary of a neighborhood $\mathcal{W}$ $(\partial\mathcal{W} = \mathcal{C})$ of volume ω including $\mathbf{x}$ and that $\mathrm{d}\ell$ is the $(d-1)$-dimensional volume element of $\mathcal{C}$. So, the multilocal level set extrinsic curvature, (MLSEC), denoted by $\bar{\kappa}_d$, is defined as a discretized version of Eq. A.8, where the multilocality is achieved assuming as selectable parameters the neighborhood $\mathcal{W}$ or its boundary $\mathcal{C}$. That is, the gradient vectors along the path $\mathcal{C}$ around $\mathbf{x}$ are taken into account to compute $\mathrm{div}(\bar{\mathbf{w}})$ at $\mathbf{x}$. Thus, the MLSEC operator for

a discrete domains is defined as:

$$\bar{\kappa}_d = -\text{div}(\bar{\mathbf{w}}) = -\frac{d}{r}\sum_{k=1}^{r} \bar{\mathbf{w}}_{\mathbf{k}}^{\mathbf{t}} \cdot \mathbf{n}_{\mathbf{k}} \tag{A.9}$$

where the adjacency r will be given by the specific $\mathcal{C}$. For example, the simplest case in 2D case ($d = 2$) is given by the four nearest neighbors of each pixel ($r = 4$).

Once $\bar{\kappa}_d$ has been established as a good creaseness measure, Lopez et al. [44] proposed filtering the gradient vector field of the image using the *structure tensor*, a well-known tool for analyzing oriented textures. The objective is achieving a higher creaseness, increasing the degree of attraction/repulsion at ridge/valley creases. At the same time, the creaseness measure is attenuated at not interesting zones.

In the d-dimensional space, given a symmetric neighborhood of size σ_I centered at a given point $\mathbf{x}$, called as $\mathcal{N}(\mathbf{x}; \sigma_{\mathcal{I}})$, the structure tensor is defined to be the symmetric and semi-positive definite $d \times d$ matrix

$$\mathbf{S}(\mathbf{x}; \sigma_I) = \mathcal{N}(\mathbf{x}; \sigma_I) * (\mathbf{w}(\mathbf{x}) \cdot \mathbf{w}^t(\mathbf{x}) \tag{A.10}$$

where the convolution "$*$" is element wise.

The eigenvector which corresponds to the highest eigenvalue of $\mathbf{S}(\mathbf{x}; \sigma_I)$, say $\mathbf{w}'(\mathbf{x}; \sigma_I)$, yields the *dominant gradient orientation* at $\mathbf{x}$, where "dominant" means inside the neighborhood $\mathcal{N}(\mathbf{x}; \sigma_I)$. A suitable choice for this window is a d-dimensional Gaussian, i.e., $\mathcal{N}(\mathbf{x}; \sigma_I) = G(\mathbf{x}; \sigma_I)$, which implies that a gradient vector at a point $\mathbf{y}$ inside the neighborhood contributes to the computation of $\mathbf{S}(\mathbf{x}; \sigma_I)$ weighted as a function of the distance from $\mathbf{x}$ to $\mathbf{y}$. The eigenvector which corresponds to the lowest eigenvalue of $\mathbf{S}(\mathbf{x}; \sigma_I)$, namely, $\mathbf{v}'(\mathbf{x}; \sigma_I)$, yields the *dominant orientation* at $\mathbf{x}$, which is perpendicular to the *dominant gradient orientation*.

This analysis assumes that within each neighborhood there is a single dominant orientation. In order to verify this assumption, a normalized *confidence measure* is introduced: a real value $\mathbf{C} \in [0, 1]$ which can be computed from the eigenvalues of the structure tensor, is associated to each orientation. A suitable function is:

$$\mathbf{C}(\mathbf{x}; \sigma_I; c) = 1 - e^{-(\lambda_\triangle(\mathbf{x}; \sigma_I))^2/2c^2} \tag{A.11}$$

where c is a predefined threshold and λ_δ is obtained from the eigenvalues of S, $\lambda_1, \ldots, \lambda_d$

$$\lambda_\Delta(\mathbf{x};\sigma_I) = \sum_{i=1}^{d} \sum_{j=i+1}^{d} (\lambda_i(\mathbf{x};\sigma_I) - \lambda_j(\mathbf{x};\sigma_I))^2 \tag{A.12}$$

Thus, the MLSEC-ST creaseness measure for a 2D image is achieved following the next steps:

1. Compute the structure tensor $\mathbf{S}$ based on the gradient vector field $\mathbf{w}$

$$\begin{aligned} \mathbf{S}(\mathbf{x};\sigma_I) &= \begin{pmatrix} s_{11}(\mathbf{x};\sigma_I;\sigma_D) s_{12}(\mathbf{x};\sigma_I;\sigma_D) \\ s_{12}(\mathbf{x};\sigma_I;\sigma_D) s_{22}(\mathbf{x};\sigma_I;\sigma_D) \end{pmatrix} \\ s_{11}(\mathbf{x};\sigma_I;\sigma_D) &= G(\mathbf{x};\sigma_I) * (L_x(\mathbf{x};\sigma_D) L_x(\mathbf{x};\sigma_D)) \\ s_{12}(\mathbf{x};\sigma_I;\sigma_D) &= G(\mathbf{x};\sigma_I) * (L_x(\mathbf{x};\sigma_D) L_y(\mathbf{x};\sigma_D)) \\ s_{22}(\mathbf{x};\sigma_I;\sigma_D) &= G(\mathbf{x};\sigma_I) * (L_y(\mathbf{x};\sigma_D) L_y(\mathbf{x};\sigma_D)) \end{aligned} \tag{A.13}$$

   where σ_D called the *differentiation scale*, denotes the standard deviation of the Gaussian kernel involved in the differentiation process to compute $\mathbf{w}$. In opposition, σ_I is called the *integration scale*. The first parameter is tuned to the size of the objects whose orientation has to be determined, whereas, the second one is adjusted to the size of the neighborhood in which an orientation is dominant.

2. Perform the eigensystem analysis of S. The dominant gradient orientation is given by the normalized eigenvector $\mathbf{w}'$ corresponding to the highest eigenvalue. In the structure tensor analysis, opposite directions are equally treated. So, to recover the direction, in 2D, $\mathbf{w}'$ and $\mathbf{w}$ are put in the same quadrant. Then, the new vector field is obtained as:

$$\tilde{\mathbf{w}} = sign(\mathbf{w}'^t \mathbf{w}) \mathbf{w}' \tag{A.14}$$

   where

$$sign(x) = \begin{cases} +1 & if \;\; x > 0 \\ -1 & if \;\; x < 0 \\ 0 & if \;\; x = 0 \end{cases}$$

   In this manner, attraction/repulsion of vector is reinforced.

3. Compute the new creaseness measure, the MLSEC-ST as:

$$\tilde{\kappa}_d = -\text{div}(\tilde{\mathbf{w}}) \tag{A.15}$$

4. Compute a confidence measure $\mathbf{C}$ to reduce creaseness in not interesting structures. Then, $\mathbf{C}\tilde{\kappa}_d$ is taken as final creaseness measure.

Additionally, in the algorithm used in this work, two another confidence measures are considered in order to ensure that the final creases correspond to vessel centerlines. The first confidence measure is the crease strength, whereas the second one is its length. Thus, first, the creases whose $\mathbf{C}\tilde{\kappa}_d$ is less than a preestablished threshold, t_S, are set to zero. After that, the creases are filtered by counting the number of connected pixels. Those creases whose number of points is less than a threshold, t_L, are set also to zero.

Appendix B

Lightness and contrast normalization

This Appendix describes two techniques to normalize the lightness and contrast in retinal images used in this work. The methods are the Foracchia et al's approach [134] and the *Multiple-Scale Retinex* (MSR) proposed by Jobson et al. [135].

B.1 Foracchia et al's approach

Foracchia et al. [134] proposed a method to normalize the lightness and contrast variability in retinal images based on estimating both features in background small areas, spreading to the whole image and then removing from it. The method assumes the following model of the retinal image:

$$I = f(I^{\circ}) = f(I_b^{\circ} + I_f^{\circ}) \tag{B.1}$$

where I° is the original image, I_b° is the original background, that is, the ideal background free of vasculature and other retinal structures included any lesion which are modeled in the original foreground, I_f°, and f represents the transformation made at the acquisition process which produces the lightness and contrast deformation.

The original background image follows a normal distribution with mean the ideal uniform lightness, μ_b, and standard deviation, σ_b, is the natural variation in the retinal pigmentation, ($I_b^{\circ} \sim \mathcal{N}(\mu_b, \sigma_b)$).

A captured image is modeled as follows:

$$\begin{aligned} I(x,y) &= f(I^\circ(x,y)) = C(x,y)I^\circ(x,y) + L(x,y) \\ &= C(x,y)I_b^\circ(x,y) + C(x,y)I_f^\circ(x,y) + L(x,y) \end{aligned} \tag{B.2}$$

where $C(x,y)$ and $L(x,y)$ represent the deviation factor of contrast and lightness respectively, which can be considered as images since they are space-dependent functions.

Thus, the normalized image is computed estimating the contrast and lightness, $\hat{C}$ and $\hat{L}$, as follows:

$$\hat{I}^\circ(x,y) = \frac{I(x,y) - \hat{L}(x,y)}{\hat{C}(x,y)} \tag{B.3}$$

Taking into account only the background pixels ($(x,y) \in \mathcal{B}$) where, by definition, $I_f^\circ = 0$, the equation B.1 is as follows:

$$I(x,y) = C(x,y)I_b^\circ(x,y) + L(x,y) \;\; , (x,y) \in \mathcal{B} \tag{B.4}$$

Considering the statistical model of I_b°, ($I_b^\circ \sim \mathcal{N}(\mu_b, \sigma_b)$), from the previous equation is deduced that $I(x,y) \sim \mathcal{N}(L(x,y), C(x,y))$ for $(x,y) \in \mathcal{B}$. Then, the normalized image is achieved through the equation B.3, estimating $\hat{L}(x,y)$ and $\hat{C}(x,y)$ by the mean and standard deviation of the background pixels in the observed image ($I(x,y),\ (x,y) \in \mathcal{B}$).

To estimate the mean and standard deviation in the background, first, the background pixels have to be determined. In that way, the image is divided in a tessellation of squares S_i with side s, where s is selected to obey the next three premises: L and C are constant in the square, at least the 50% of pixels in the region belong to background, and the intensity of the background and foreground pixels are very different. Then, the mean $\hat{\mu}(S_{\frac{m}{s}\times\frac{n}{s}})$ and standard deviation $\hat{\sigma}(S_{\frac{m}{s}\times\frac{n}{s}})$ images are build, computing the mean $\hat{\mu}(S_i)$ and the standard deviation $\hat{\sigma}(S_i)$ for each S_i. The full images $\hat{\mu}(S_{m\times n})$ and $\hat{\sigma}(S_{m\times n})$ are computed by bicubic interpolation from the small images $\hat{\mu}(S_{\frac{m}{s}\times\frac{n}{s}})$ and $\hat{\sigma}(S_{\frac{m}{s}\times\frac{n}{s}})$, being $m \times n$ the original image resolution. Hence, the membership to the background for each pixel in the image is determined by means of the Mahalanobis distance as follows:

$$(x,y) \in \mathcal{B} \leftrightarrow \left| \frac{I(x,y) - \hat{\mu}(S_{m\times n})(x,y)}{\hat{\sigma}(S_{m\times n})(x,y)} \right| < t \tag{B.5}$$

where t is a threshold that was set to 1, while a value of 200 for the tessella side was selected empirically.

Once the background pixels are determined, the same tessellation of squares is taken into account and the mean and standard deviation for the background pixels at each tessella are computed. Then, a bicubic interpolation is applied again to achieve $\hat{L}(x, y)$ and $\hat{C}(x, y)$. Finally, the normalized image is obtained applying the equation B.3. It should be noted that as the input image is a color image, this normalization has to made to each color component and then combining the results.

B.2 Retinex technique

The color constancy is a feature of the human color perception system to ensure that the perceived color of objects remains relatively constant under varying illumination conditions. Various models in the literature try to emulate the color constancy of human visual system, but the Land's retinex theory [136, 137] further reduced the computational complexity of the model.

Land's retinex theory assumes that the three classes of cone receptors, corresponding to the three long, middle and short-wavelenght regions of the visible spectrum, or colloquially, red, green and blue, are independent. With this assumption, at each channel i, the lightness I_i is the product of the illumination M_i and the reflectance R_i.

$$I_i(x, y) = M_i(x, y)R_i(x, y) \tag{B.6}$$

Taking the logarithm of the previous equation the multiplication is transformed into addition

$$I'_i(x, y) \quad = log(I_i(x, y)) = log(M_i(x, y)) + log(R_i(x, y)) \tag{B.7}$$

Another main assumption of the retinex theory is that the illumination varies slowly in space, so its wavelength is large an its frequency low; whereas the sharp changes are due to the reflectance.

Following the previous assumptions, the implementations of the retinex theory and other techniques such as, homomorphic filtering, produce an image that depends only on reflectance $R_i(x, y)$, subtracting from the original image an approximation of the illumination $M_i(x, y)$. While, the homomorphic filtering separates the illumination by a low pass filtering in Fourier space, the retinex implementations are applied in spatial domain.

The retinex implementations proposed in this work to reduce, or ideally, to remove the lightness variation in retinal images are the Jobson et al. approaches, the Single-Scale Retinex (SSR) [138] and the Multiple-Scale Retinex (MSR) [135].

In the SSR, the illumination is estimated by means of a Gaussian form and, then, it is subtracted from the original image to obtain a description invariant to illumination. This is given by the next equation:

$$R'_i(x, y) = \log I_i(x, y) - \log[F(x, y) * I_i(x, y)] \tag{B.8}$$

where $R'_i(x, y)$ is the retinex output, that is, the estimated reflectance in log domain, $I_i(x, y)$ is the i-th component of original image, '$*$' denotes the convolution operation and $F(x, y)$ is the weighting function

$$F(x, y) = Ke^{\frac{-x^2 + y^2}{c^2}} \tag{B.9}$$

where K is selected to obey

$$\int\int F(x, y)dxdy = 1 \tag{B.10}$$

then $K = \dfrac{1}{(\sum_x \sum_y F(x, y))}$ and c is the scale that controls the Gaussian surround. Small values for c imply more dynamic range compression preserving the fine details in the image, but also they can affect negatively the quality of color image. Moreover, halo artifacts may be generated when two closed areas have very different intensities. Thus, to balance the positive and negative effects of small and large scales and to reduce halo artifact induced by the single-scale retinex, the multi-scale approach arises [135]. The MSR is simply a weighted sum of several different SSR outputs computed with different

scales as follows:

$$R_{MSR_i} = \sum_{n=1}^{N} w_n R'_{n_i} \tag{B.11}$$

where R_{MSR_i} is the MSR output in the i-th color component, N is the number of scales, R'_{n_i} is the SSR output in the i-th color component on the n-th scale and w_n is the weight of the output of the n-th scale. Jobson et al. [135], experimentally, achieved that equal weighting of the scales $w_n = 1/3$, with $N = 3$ was enough for most of the applications.

The main advantages of these two retinex algorithms are the easy implementation and manipulation of parameters and the lack of requirements for scene calibration. In addition, the MSR came up to get simultaneously the dynamic range compression of the retinex in small scale and the tonal rendition of the big-scale retinex.

Appendix C

Minimal paths

This Appendix summarizes the minimal path approach presented by Cohen and Kimmel [86].

A snake or active contour is a curve guided by external constraint forces and image forces which push it towards image feature edges. From the classical active contour equation presented by Kass et al. [71], many approaches have emerged to solve different problems in varied domains and to overcome the main drawbacks of the original model: manual initialization, the stucking in local minima and the unchangeable topology.

Following the approach of the geodesic active contours [139], Cohen and Kimmmel reformulated the classical snake equation [71]. The aim of this model is to find the curve $C(s)$ that minimizes the following equation:

$$\begin{array}{rl} E(\mathcal{C}) & = \int_\Omega E_{int}(\mathcal{C}(s)) + E_{ext}(\mathcal{C}(s))ds \\ & = \int_\Omega w\|\frac{\partial \mathcal{C}}{\partial s}(s)\|^2 + P(\mathcal{C}(s))ds \end{array} \tag{C.1}$$

where $\Omega \in [0, L]$ and L is the length of the curve. The internal energy is the partial derivative of the curve with respect to its arc-length parameter, s, and controls the regularity in the contour by the parameter w. The external energy term is the potential, P, which represents the desired image features.

Since s represents the arc-length parameter, $\|\frac{\partial \mathcal{C}}{\partial s} = 1\|$ and the energy of the model

has the following form:

$$E(\mathcal{C}) = \int_{\Omega} w + P(\mathcal{C}(s))ds = \int_{\Omega} \widetilde{P}(\mathcal{C}(s))ds \tag{C.2}$$

The regularization of this model is achieved by the constant $w > 0$. This term integrates as $\int_{\Omega} wds = w \times \text{length}(C)$ and allows us to control the smoothness of the contour.

Given a potential $P > 0$ that takes lower values near desired features, we are looking for paths along that minimize the previous equation. Then, the surface of minimal action $\mathcal{U}$ is defined as the minimal energy integrated along a path between a starting point p_0 and any point p:

$$\begin{aligned} \mathcal{U}(p) &= \inf_{\mathcal{A}_{p_0,p}} \int_{\Omega} (w + P(C(s)))ds \\ &= \inf_{\mathcal{A}_{p_0,p}} \int_{\Omega} \tilde{P}(C(s))ds \end{aligned} \tag{C.3}$$

where $\mathcal{A}_{p_0,p}$ is the set of all paths between the points p_0 and p. Hence, the minimal path between two points p_0 and p_1 is computed from this surface map by backpropagation starting from p_1 until p_0.

In order to compute $\mathcal{U}$, a front propagation equation related to C.3 is defined:

$$\frac{\partial C(s,t)}{\partial t} = \frac{1}{\widetilde{P}} \vec{n}(s,t) \tag{C.4}$$

where t represents the time, $\widetilde{P} = P + w$, and $\vec{n}(s,t)$ is the normal to the closed curve $C(.,t)$. This equation evolves the front from a small circle centered at p_0 up to each point inside the image domain. The value of $\mathcal{U}(p)$ is the time t when the front passes over p.

There are several numerical approaches to compute the surface of minimal action. However, the Fast Marching Method [140] is recommended for any real time application. Given the potential values $P_{i,j} = P(i\Delta x, j\Delta y)$ in a grid, where $\Delta x = \Delta y = 1$, the Fast Marching method approximates $U_{i,j}$ by u using the following equation:

$$\begin{aligned} P_{i,j}^2 &= (\max\{u - U_{i-1,j}, u - U_{i+1,j}, 0\})^2 \\ &+ (\max\{u - U_{i,j-1}, u - U_{i,j+1}, 0\})^2 \end{aligned} \tag{C.5}$$

Algorithm 4 summarizes the steps involved in the computation of the surface of minimal action. Since the method selects the pixels in a specific order, it is only necessary one pass on the image.

Algorithm 4 Fast Marching method

Definitions:

- *Alive* set: points of the grid for which U has been computed and it will not be modified.
- *Trial* set: next points in the grid to be examined (4-connectivity) for which a estimation of U is computed using the points in *alive* set.
- *Far* set: the remaining points of the grid for which there is not an estimate for U.

Initialization:

- For each point in the grid, let $U_{i,j} = \infty$ (large positive value).
  Put all points in the *far* set.
- Set the start point $(i, j) = p_0$ to be zero:
  $U_{p_0} = 0$, and put it in the *trial* set.

Marching loop:

- Select $p = (i_{min}, j_{min})$ from *trial* with the lowest value of U.
- If p is equal to p_1 being p_1 the final point then we finish.
- Else put p in *alive* and remove it from the *trial* set.
- For each of the 4 neighboring grid points (k, l) of (i_{min}, j_{min}):
  - If (k, l) belongs to *far* set, then put (k, l) in *trial* set.
  - If (k, l) is not in *alive* set, then set $U_{k,l}$ with Equation C.5.

Finally, the minimal path is obtained by back-propagation from p_1 to p_0 using a discrete steepest descent algorithm, selecting at each step the connected pixel with the lowest $\mathcal{U}$. However, this method accumulates an angular error, so more precise methods, such as Heun or Runge-Kutta, could be also used.

Appendix D

Image registration

This Appendix is devoted to explain the image registration technique used in the AVR monitoring system.

The registration algorithm is a feature-based registration method whose landmark is the vessel tree [141]. Following the idea that the vessels can be thought as creases (ridges and valleys) when images are seen as landscapes, the registration process is based on the alignment of crease images. Thus, the first stage of the algorithm is to obtain the crease images of the reference and the new sample images using the MLSEC-ST operator [44]. After obtaining the crease images, an iterative optimization process to align both images is performed. That is, the reference image is fixed and the other one is transformed until a global maximum is accomplished. A suitable function to measure the alignment quality is the correlation function:

$$Corr_\tau = \sum_{x \in f} f(x) g(\tau(x)) \tag{D.1}$$

where f and g are the crease images and τ represent the transformation whose five parameters (x and y translation, t_x, t_y, rotation angle θ in clockwise direction and x and y scale, s_x, s_y) we want to test.

The search space is defined by the function $Corr_\tau$ and the five parameters of the transformation. The function is non monotonic, that is, it has many local maxima and

it is expensive to compute since it involves image transformations. Thus, to simplify the optimization process, the multiple resolution approach proposed by Elsen et al. [142] is carried out. Moreover, with the same aim in mind, the transformation is not applied to all pixels in the image, only the main creases with pixel values higher than a fixed threshold are transformed.

The multiple resolution approach is handled by two pyramids (Figure D.1) where the two crease images to register are at the bottom and each pyramid level is a half-resolution version of the image in the previous level, until images have a size of 64 pixels in one dimension.

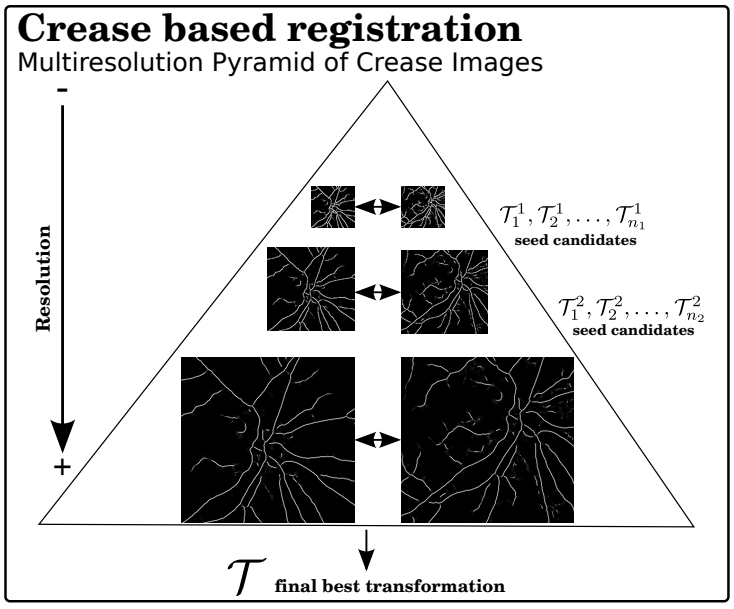

Figure D.1: Schema of the multiple resolution registration process

The search starts at the top of the pyramid where an exhaustive search can be accomplished at the Fourier domain to compute the correlation. Thus, the search seeds are the image transformations which maximize $Corr_\tau$ computed in the frequency domain. At this level, the transformations performed involve only rotations of an angle of 5° during a certain number of iterations. For a pyramid of three levels, the number of iterations was 10 and the number of seeds considered at each level were 6, 3 and 1, respectively. In the remaining levels, a Downhill Simplex algorithm is applied to optimize the correlation. At

those levels, the search seed are the optimized transformations of the previous level and the search process finishes when the difference between the maximum and the minimum values found in a neighborhood is lower than a preestablished threshold.

Once the registration process has been finished and the two images are aligned, the registered crease images are used to obtain a similarity measure between them in order to determine the quality of the register process. This measure is the normalized cross-correlation coefficient, γ defined as:

$$\gamma = \frac{\sum_{x,y}[f(x,y)-\bar{f}]\,[g(x,y)-\bar{g}]}{\sqrt{\sum_{x,y}[f(x,y)-\bar{f}]^2 \sum_{x,y}[g(x,y)-\bar{g}]^2}} \tag{D.2}$$

where $\bar{g}$ is the mean of the registered image and $\bar{f}$ is the mean of the reference image. The registration process is valid if γ is higher than a threshold, otherwise, the AVR can not be computed using monitoring.

In order to evaluate the registration method, a dataset composed of 20 retinal images was used. The images were taken with a Canon CR6-45NM non-mydriatic retinal camera with a 768×584 pixel resolution. For each image, 50 random transformations were applied with maximum translation and rotation values of ± 100 pixels and $\pm 5°$, respectively, and without scaling. These transformations represent the maximum transformation values of the majority of the analyzed images. Table D.1 shows the mean and standard deviation values of the absolute difference between the transformation applied and the transformation recovered by the method, the mean square error (MSE) of the recovered transformations and the registration accuracy (RA). The absolute difference was computed as $\overline{\tau_a - \tau_r} = |(t_x - t'_x) + (t_y - t'_y) + (\theta - \theta') + (s_x - s'_x) + (s_y - s'_y)|$, where τ_a and τ_r represent the applied and the recovered transformations being $t_x, t_y, \theta, s_x, s_y$ and $t'_x, t'_y, \theta', s'_x, s'_y$ their translation, rotation and scaling parameters, respectively. The registration accuracy represents the percentage of the transformations where the applied and the recovered transformations are equal with ± 1 pixel of difference. To obtain this measure, four points are selected manually and their positions in the transformed and the dynamic images are compared. Thus, the average of the euclidean distances between the

positions of the four points is calculated. If the absolute value of the average is less or equal than 1 pixel, the applied and the recovered transformation are aligned. The small MSE value and the high RA indicate the good performance of the image registration method.

	$\overline{\boldsymbol{\tau}_a - \boldsymbol{\tau}_r}$	**MSE**	**RA(%)**
Mean	0.033	0.097	99.100
Standard deviation	0.050	0.070	1.550

Table D.1: Image registration accuracy in a dataset of 20 retinal images.

Appendix E

Crossover and bifurcation detection

This Appendix explains the algorithm used to detect the crossover and bifurcation points in retinal vessels in order to discard these points from the AVR computation. The method was described in [143] for locating the landmark points in a personal authentication system based on the retinal vessel tree. We select this method because the detection of points of interest is performed directly on the vessel centerlines obtained with MLSEC-ST algorithm, without a segmentation of the vascular tree and a subsequent skeletonization thereof.

The algorithm consists on tracking the vessel centerlines in order to obtain the relationships between them. The vessel centerlines given by the MLSEC-ST algorithm present discontinuities in crossovers and bifurcations because the different orientations of the vessels involved or in other areas with low contrast or noise. Thus, before locating the points of interest, the centerline segments are joined to build the whole vascular tree.

The first step of the algorithm is the tracking and labeling of the centerline segments as line of 1 pixel width. To this end, each pixel of the centerline image is examined from top to bottom and from left to right, starting the segment tracking when a non-null pixel is found. In case the pixel is isolated, it is removed. Otherwise, the 4 pixels in a 8-neighborhood which have not been tracked yet (the three at bottom and the one to the right as Figure E.1 shows) are analyzed and the tracking starts in one or two directions

depending on the number of the neighbors which belong to centerlines. Thus, if the pixel has only one neighbor, the tracking is performed in one direction and the pixel is marked as endpoint. In case of two or more neighbors, two tracking process are thrown. At each step of the tracking, only one neighbor is selected as next point of the segment. The pixel selected is the one with the most non-flagged neighbors corresponding to the segment pixels in order to keep segments of 1-pixel width. In case of tie, the pixel is selected according to the most repeated orientation in the previous steps.

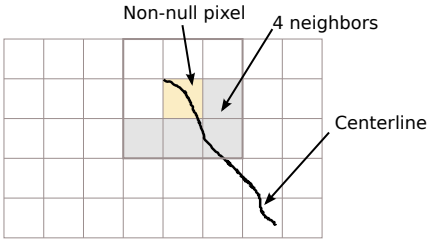

Figure E.1: Four neighbors to analyze for each non-null pixel found in the centerline tracking.

Once the segments have been labeled in the whole image and the endpoints were located, the relationships between segments are identified. The simplest relationship is the union which occurs when a segment is the continuation of the other in the same retinal vessel. To find this situation, pairs of close segments are joined through a straight line, and the smoothness of the joining is analyzed by the angles between the line and the direction of segments calculated by the orientation of the endpoints. The union is accepted if both angles are less than a threshold, t_θ. A value $t_\theta = \frac{3\pi}{4}$ rad was used with success in all cases.

Crossovers and bifurcations are the other relationships between segments to be located. However these can be simplified to bifurcations since a crossover can be seen as two close bifurcations from the same vessel. The criterion to locate bifurcations is to find an endpoint close to a segment where the segment of the endpoint starts. Thus, for each endpoint in the image, its direction is computed and it is prolonged in that direction a fixed maximum distance by a straight line. A neighborhood near the prolongation is analyzed in order to locate other segments. In case a point, p_b which belongs to other segment is located, the angle between its direction and the endpoint direction is computed.

If the angle is less than a threshold, t_α, and the distance between p_b and the extremes of its segment is larger than a threshold, d_b, the point p_b is marked as bifurcation and it is joined to the endpoint. We have used $t_\alpha = \pi$ rad and $d_b = 5$ pixels.

Finally, two close bifurcation points are merged into a crossover point by the midpoint between them.

Additionally, in the tracking process a segment filtering is performed. Thus, segments whose length does not exceed a certain threshold are not taken into account. The minimum length required for a centerline segment was 24 pixels.

Appendix F

Related Publications

G. Coll de Tuero, S. G. Vázquez, A. Rodríguez Poncelas, M. A. Barcel 'o, J. Barrot de la Puente, M. G. Penedo, A. Pose-Reino, M. Pena-Seijo, M. Saez, "Prognostic value of the evolution of fundus lesions in newly diagnosed hypertensive patients at one year follow-up", Journal of Hypertension , 2013 (pending of acceptation).

S. G. Vázquez, N. Barreira, M. G. Penedo, M. Pena-Seijo, F. Gómez-Ulla, "Evaluation of SIRIUS retinal vessel width measurement in REVIEW dataset", Proceedings of the 26^{th} IEEE International Symposium On Computer-Based Medical Systems, 2013 (pending of publication).

S. G. Vázquez, N. Barreira, M. G. Penedo, M. Rodríguez-Blanco, "Reliable monitoring system for arteriovenous ratio computation", Computerized Medical Imaging and Graphics , 2013 (pending of acceptation).

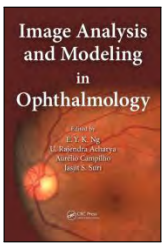

M. G. Penedo, S. G. Vázquez, N. Barreira, M. Saez, A. Pose-Reino, M. Rodríguez-Blanco, "Arteriovenous Ratio Calculation using Image Processing Techniques", Image Analysis and Modeling in Ophthalmology. CRC Press (Taylor & Francis)., 1, Chapter 13, 2012. (pending of publication).

M. Saez, S. G. Vázquez, M. G. Penedo, M. A. Barceló, M. Pena, G. Coll de Tuero, A. Pose-Reino, "Development of an automated system to classify retinal vessels into arteries and veins", Computer Methods and Programs in Biomedicine, 108, 367-376, 2012.

S. G. Vázquez, B. Cancela, N. Barreira, M. G. Penedo, M. Rodríguez-Blanco, M. Pena Seijo, G. Coll de Tuero, M. Antònia Barceló, M.Saez, "Improving retinal artery and vein classication by means of a minimal path approach", Machine Vision and Applications, 1-12, Springer-Verlag, 2012.

S. G. Vázquez, N. Barreira, M. G. Penedo, M. Rodríguez-Blanco, "The significance of the vessel registration for a reliable computation of arteriovenous ratio", LNCS: Image Analysis and Recognition (ICIAR), Springer-Verlag, 7325,347-354, 2012.

S. G. Vázquez, N. Barreira, M. G. Penedo, M. Rodríguez-Blanco, F. Gómez-Ulla, A. González, G. Coll de Tuero, "Automatic arteriovenous ratio computation: emulating the experts ", Technological Innovation for Value Creation. IFIP Advances in Information and Communication Technology, 372, 563-570, Springer Berlin Heidelberg, Costa da Caparica, Lisbon, Portugal , February 2012.

M. Pena, M. G. Penedo, M. Ortega, S. G. Vázquez, F. Gómez-Ulla, A. Pose-Reino, "SIR-IUS, Computerized Tool for Automatic Analysis of Retinal Microcirculation", Journal of Hypertension, 29, e202, 2011.

M. Pena, S. G. Vázquez, A. Pose-Reino, J.L. Daz, M. Suárez, M. G. Penedo, R. Monte-Secades, J.C. Estévez, "Comparison semi-automatic method based on snake model vs linear model to study of hypertensive retinopathy", Journal of Hypertension, 28, e495, 2010.

S. G. Vázquez, B. Cancela, N. Barreira, M. G. Penedo, M. Saez, "On the Automatic Computation of the Arterio-Venous Ratio in Retinal Images: Using Minimal Paths for the Artery/Vein Classification",Proceedings of the 2010 International Conference on Digital Image Computing: Techniques and Applications (DICTA), 599-603, IEEE Computer Society, Sydney, Australia, December 2010.

S. G. Vázquez, N. Barreira, M. G. Penedo, M. Ortega, A. Pose-Reino, "Improvements in Retinal Vessel Clustering Techniques:Towards the Automatic Computation of the Arterio Venous Ratio", Computing, 90 (3-4), 197-217, Springer Vienna, 2010.

S. G. Vázquez, N. Barreira, M. G. Penedo, M. Saez, A. Pose-Reino, "Using retinex image enhancement to improve the Artery/Vein classification in retinal images", LNCS: Image Analysis and Recognition (ICIAR), 6112, 50-59, Springer Berlin Heidelberg, 2010.

S. G. Vázquez, N. Barreira, M. Penas, M. G. Penedo, A. Pose-Reino, "Automatic Classification of Retinal Vessels into Arteries and Veins", Seventh IASTED International Conference on Biomedical Engineering (BioMed), 1, 231-236, ACTA Press, Innsbruck, Austria, February 2010.

Bibliography

[1] N. L. Stokoe and R. W. Turner. Normal retinal vascular pattern. arteriovenous ratio as a measure of arterial calibre. *Br J Ophthalmol.*, 50(1):21–40, 1966.

[2] L. D. Hubbard, R. J. Brothers, W. N. King, L. X. Clegg, R. Klein, L. S. Cooper, A. R. Sharrett, M. D. Davis, and J. Cai. Methods for evaluation of retinal microvascular abnormalities associated with hypertension/sclerosis in the atherosclerosis risk in communities studies. *Ophthalmology*, 106:2269 – 2280, 1999.

[3] A. Pose-Reino, F. Gomez-Ulla, B. Hayik, M. Rodriguez-Fernndez, M.J. Carreira-Nouche, A. Mosquera-Gonzlez, M. Gonzlez-Penedo, and F. Gude. Computerized measurement of retinal blood vessel calibre: description, validation and use to determine the influence of ageing and hypertension. *Journal of Hypertension*, 23(4):843 – 850, 2005.

[4] Michael D. Knudtson, Kristine E. Lee, Larry D. Hubbard, Tien Yin Wong, Ronald Klei, and Barbara E.K. Klein. Revised formulas for summarizing retinal vessel diameters. *Current Eye Research*, 27(3):143 – 149, 2003.

[5] D Purves, GJ Augustine, D Fitzpatrick, and editors. et al. *Neuroscience. 2nd edition.* Sunderland (MA): Sinauer Associates, 2001.

[6] Paul L. Kaufman Paul and Albert Alm. *Fisiología del ojo. Versión en espaol de la 10 edición de la obra original en inglés.* Sunderland (MA): Sinauer Associates, 2004.

[7] T.T. Nguyen, J.J. Wang, and T.Y. Wong. Retinal Vascular Changes in Pre-diabetes and Prehypertension: New findings and their research and clinical implications. *Diabetes Care*, 30(10):2708 – 2715, 2007.

[8] JJ. Kanski. *Oftalmología Clínica*. Madrid: Elsevier, 2004.

[9] Gunn RM. On ophthalmoscopic evidence of general arterial disease. *Trans Ophthalmol Soc UK*, 18:356–381, 1898.

[10] HP Wagener and NM Keith. Diffuse arteriolar disease with hypertension and the associated retinal lesions. *Medicine*, 18:317–430, 1939.

[11] NM Keith, HP Wagener, and NW Barker. Some different types of essential hypertension: their course and prognosis. *Am J Med Sci.*, 197:332–343, 1939.

[12] HG Scheie. Evaluation of ophthalmoscopic changes of hypertension and arteriolar sclerosis. *Arch Ophthalmol.*, 49(2):117–138, 1953.

[13] PM Dodson, GY Lip, SM Eames, JM Gibson, and DG Beevers. Hypertensive retinopathy: a review of existing classification systems and a suggestion for a simplified grading system. *Journal of Human Hypertension*, 10(2):93–98, 1996.

[14] European Society of Hypertension-European Society of Cardiology Guidelines Committee. 2003 european society of hypertension-european society of cardiology guidelines for the management of arterial hypertension. *Journal of Hypertension*, 21(6):1011–1053, 2003.

[15] G Mancia G, G De Backer, A Dominiczak, R Cifkova, R Fagard, G Germano, G Grassi, AM Heagerty, SE Kjeldsen, S Laurent, K Narkiewicz, L Ruilope, A Rynkiewicz, RE Schmieder, HA Boudier, and A Zanchetti. 2007 esh-esc practice guidelines for the management of arterial hypertension: Esh-esc task force on the management of arterial hypertension. *Journal of Hypertension*, 25(9):1751–1762, 2007.

[16] C Cuspidi, G Macca, M Salerno, L Michev, V Fusi, B Severgnini, C Corti, S Meani, F Magrini, and A Zanchetti. The eye as a target organ: An updated classification of hypertensive retinopathy. *Ital Heart J.*, 2(9):702–706, 2001.

[17] T. Wong and P. Mitchell. The eye in hypertension. *The Lancet*, 369(9559):425–435, 2007.

[18] T.Y. Wong, R. Klein, A.R. Sharrett, B.B. Duncan, D.J. Couper, B.E.K. Klein, L.D. Hubbard, and F.J. Nieto. Retinal arteriolar diameter and risk for hypertension. *Ann Intern Med*, 140(4):248–55, 2004.

[19] Wayne Smith, Jie Jin Wang, Tien Yin Wong, Elena Rochtchina, Ronald Klein, Stephen R. Leeder, and Paul Mitchell. Retinal arteriolar narrowing is associated with 5-year incident severe hypertension: The blue mountains eye study. *Hypertension*, 44(4):442–447, 2004.

[20] Wong TY, Duncan BB, Golden SH, Klein R, Couper DJ, Klein BE, Hubbard LD, Sharrett AR, and Schmidt MI. Associations between the metabolic syndrome and retinal microvascular signs: the atherosclerosis risk in communities study. *Invest Ophthalmol Vis Sci.*, 45(9):2949–2954, 2004.

[21] Thanh T. Nguyen, Jie Jin Wang, F.M. Amirul Islam, Paul Mitchell, Robyn J. Tapp, Paul Z. Zimmet, Richard Simpson, Jonathan Shaw, and Tien Y. Wong. Retinal arteriolar narrowing predicts incidence of diabetes: The australian diabetes, obesity and lifestyle (ausdiab) study. *Diabetes*, 57(3):536–539, 2008.

[22] Wong T, Klein R, Sharrett A, and et al. Cerebral white matter lesions, retinopathy, and incident clinical stroke. *JAMA*, 288(1):67–74, 2002.

[23] M. Kamran Ikram, Frank Jan de Jong, Johannes R. Vingerling, Jacqueline C. M. Witteman, Albert Hofman, Monique M. B. Breteler, and Paulus T. V. M. de Jong. Are retinal arteriolar or venular diameters associated with markers for cardiovascular disorders? the rotterdam study. *Investigative Ophthalmology & Visual Science*, 45(7):2129–2134, 2004.

[24] Wong TY, Rosamond W, Chang PP, and et al. Retinopathy and risk of congestive heart failure. *JAMA*, 293(1):63–69, 2005.

[25] Wong T, Klein R, Sharrett A, and et al. Retinal arteriolar narrowing and risk of coronary heart disease in men and women: The atherosclerosis risk in communities study. *JAMA*, 287(9):1153–1159, 2002.

[26] Lawton S. Cooper, Tien Y. Wong, Ronald Klein, A. Richey Sharrett, R. Nick Bryan, Larry D. Hubbard, David J. Couper, Gerardo Heiss, and Paul D. Sorlie. Retinal microvascular abnormalities and mri-defined subclinical cerebral infarction: The atherosclerosis risk in communities study. *Stroke*, 37(1):82–86, 2006.

[27] M. Lalonde, M. Beaulieu, and L. Gagnon. Fast and robust optic disc detection using pyramidal decomposition and hausdorff-based template matching. *IEEE Transactions on Medical Imaging*, 20(11):1193–1200, 2001.

[28] A. Hunter, D. Steel, A. Basu, R. Ryder, E. Fletcher, and L. Kennedy. Optic nerve head segmentation. *IEEE Transactions on Medical Imaging*, 23(2):256 – 264, 2004.

[29] A. Osareh, M. Mirmehdi, B. T. Thomas, and R. Markham. Classification and localisation of diabetic-related eye disease. In *Proceedings of the 7th European Conference on Computer Vision-Part IV*, pages 502–516, 2002.

[30] C. Sinthanayothin, J. Boyce, H. Cook, and T. Williamson. Automated localisation of the optic disc, fovea, and retinal blood vessels from digital colour fundus images. *Br J Ophthalmol.*, 83(8):902–910, 1999.

[31] Sekhar S., Al-Nuaimy W., and Nandi A.K. Automated localisation of retinal optic disk using hough transform. *ISBI 2008. 5th IEEE International Symposium on Biomedical Imaging*, 15(6):1577 – 1580, 2008.

[32] R. A. Abdel-Ghafar and T. Morris. Progress towards automated detection and characterization of the optic disc in glaucoma and diabetic retinopathy. *Medical Informatics and the Internet in Medicine*, 32(1):19 – 25, 2007.

[33] A. Aquino, M.E. Geguúndez-Arias, and D. Mariín. Detecting the optic disc boundary in digital fundus images using morphological, edge detection, and feature extraction techniques. *IEEE Transactions on Medical Imaging*, 29(11):1860 – 1869, 2010.

[34] F. Mendels, C. Heneghan, and J. Thiran. Identification of the optic disk boundary in retinal images using active contours. In *Proceedings of the Irish Machine Vision and Image Processing Conference*, pages 103–115, 1999.

[35] Koichiro Akita and Hideki Kuga. A computer method of understanding ocular fundus images. *Pattern Recognition*, 15(6):431–443, 1982.

[36] T. Walter and J. Klein. Segmentation of color fundus images of the human retina:detection of the optic disc and the vascular tree using morphological techniques. In *ISMDA*, pages 282–287, 2001.

[37] M. Foracchia, E. Grisan, and A. Ruggeri. Detection of optic disc in retinal images by means of a geometrical model of vessel structure. *IEEE Transactions on Medical Imaging*, 23(19):1189 – 1195, 2004.

[38] Hoover A. and Goldbaum M. Locating the optic nerve in a retinal image using the fuzzy convergence of the blood vessels. *IEEE Transactions on Medical Imaging*, 22(8):951 – 958, 2003.

[39] A.A.-H. Abdel-Razik Youssif, A.Z. Ghalwash, and A.A.S. Abdel-Rahman Ghoneim. Optic Disc Detection From Normalized Digital Fundus Images by Means of a Vessels' Direction Matched Filter. *IEEE Transactions on Medical Imaging*, 27(1):11 – 18, 2008.

[40] Meindert Niemeijer, Michael D. Abràmoff, and Bram van Ginneken. Fast detection of the optic disc and fovea in color fundus photographs. *Medical Image Analysis*, 13(6):859 –870, 2009.

[41] A. M. Mendonça, F. Cardoso, A. V. Sousa, and A. J. C. Campilho. Automatic localization of the optic disc in retinal images based on the entropy of vascular directions. In *ICIAR (2)*, pages 424–431, 2012.

[42] D.H. Ballard. Generalizing the hough transform to detect arbitrary shapes. *Pattern Recognition*, 13(2):111–122, 1981.

[43] M. Blanco, M. G. Penedo, N. Barreira, M. Penas, and M. J. Carreira. Localization and extraction of the Optic Disc using the Fuzzy Circular Hough Transform. *Lecture Notes Artificial Intelligence: Artificial Intelligence and Soft Computing*, 4029:713–721, 2006.

[44] A. M. López, D. Lloret, J. Serrat, and J. J. Villanueva. Multilocal Creaseness Based on the Level-Set Extrinsic Curvature. *Computer Vision and Image Understanding*, 77(2):111 – 144, 2000.

[45] Paul Hough. Method and Means for Recognizing Complex Patterns. U.S. Patent 3.069.654, December 1962.

[46] M. M. Fraz, P. Remagnino, A. Hoppe, B. Uyyanonvara, A. R. Rudnicka, C. G. Owen, and S. A. Barman. Blood vessel segmentation methodologies in retinal images - a survey. *Comput. Methods Prog. Biomed.*, 108(1):407–433, October 2012.

[47] S. Chaudhuri, S. Chatterjee, N. Katz, M. Nelson, and M. Goldbaum. Detection of blood vessels in retinal images using two-dimensional matched filters. *Medical Imaging, IEEE Transactions on*, 8(3):263 –269, sep 1989.

[48] L. Gang, O. Chutatape, and S.M. Krishnan. Detection and measurement of retinal vessels in fundus images using amplitude modified second-order gaussian filter. *Biomedical Engineering, IEEE Transactions on*, 49(2):168 –172, 2002.

[49] Mohammed Al-Rawi, Munib Qutaishat, and Mohammed Arrar. An improved matched filter for blood vessel detection of digital retinal images. *Computers in Biology and Medicine*, 37(2):262–267, 2007.

[50] L. Sukkaew, B. Uyyanonvara, S. Barman, A. Fielder, and K. Cocker. Automatic extraction of the structure of the retinal blood vessel network of premature infants. *J Med Assoc Thai*, 90(9):1780–92, 2007.

[51] M. Niemeijer, J.J. Staal, B. van Ginneken, M. Loog, and M.D. Abramoff. Comparative study of retinal vessel segmentation methods on a new publicly available database. In J. Michael Fitzpatrick and M. Sonka, editors, *SPIE Medical Imaging*, volume 5370, pages 648–656. SPIE, SPIE, 2004.

[52] J. Staal, M.D. Abramoff, M. Niemeijer, M.A. Viergever, and B. van Ginneken. Ridge-based vessel segmentation in color images of the retina. *Medical Imaging, IEEE Transactions on*, 23(4):501 –509, april 2004.

[53] J.V.B. Soares, J.J.G. Leandro, R.M. Cesar, H.F. Jelinek, and M.J. Cree. Retinal vessel segmentation using the 2-d gabor wavelet and supervised classification. *Medical Imaging, IEEE Transactions on*, 25(9):1214 –1222, sept. 2006.

[54] C.A. Lupascu, D. Tegolo, and E. Trucco. Fabc: Retinal vessel segmentation using adaboost. *Information Technology in Biomedicine, IEEE Transactions on*, 14(5):1267 –1274, sept. 2010.

[55] Y.A. Tolias and S.M. Panas. A fuzzy vessel tracking algorithm for retinal images based on fuzzy clustering. *Medical Imaging, IEEE Transactions on*, 17(2):263 –273, april 1998.

[56] FabiolaM. Villalobos-Castaldi, EdgardoM. Felipe-Rivern, and LuisP. Snchez-Fernndez. A fast, efficient and automated method to extract vessels from fundus images. *Journal of Visualization*, 13:263–270, 2010.

[57] A.M. Mendonca and A. Campilho. Segmentation of retinal blood vessels by combining the detection of centerlines and morphological reconstruction. *Medical Imaging, IEEE Transactions on*, 25(9):1200 –1213, sept. 2006.

[58] O. Chutatape, Liu Zheng, and S.M. Krishnan. Retinal blood vessel detection and tracking by matched gaussian and kalman filters. In *Engineering in Medicine and*

Biology Society, 1998. Proceedings of the 20th Annual International Conference of the IEEE, volume 6, pages 3144 –3149 vol.6, oct-1 nov 1998.

[59] Yi Yin, Mouloud Adel, and Salah Bourennane. Retinal vessel segmentation using a probabilistic tracking method. *Pattern Recognition*, 45(4):1235–1244, 2012.

[60] L. Espona, M.J. Carreira, M.G. Penedo, and M. Ortega. Retinal vessel tree segmentation using a deformable contour model. In *Pattern Recognition, 2008. ICPR 2008. 19th International Conference on*, pages 1 –4, 2008.

[61] B. Al-Diri, A. Hunter, and D. Steel. An active contour model for segmenting and measuring retinal vessels. *Medical Imaging, IEEE Transactions on*, 28(9):1488 – 1497, 2009.

[62] I. G. Caderno, M. G. Penedo, N. Barreira, C. Mari no, and F. González. Precise Detection and Measurement of the Retina Vascular Tree. *Pattern Recognition and Image Analysis: Advances in Mathematical Theory and Applications*, 15(2):523 – 526, 2005.

[63] Olaf Brinchmann-Hansen and Halvor Heier. Theoretical relations between light streak characteristics and optical properties of retinal vessels. *Acta Ophthalmologica*, 64(S179):33–37, 1986.

[64] P.H. Gregson, Z. Shen, R.C. Scott, and V. Kozousek. Automated grading of venous beading. *Computers and Biomedical Research*, 28(4):291–304, 1995.

[65] Liang Zhou, M.S. Rzeszotarski, L.J. Singerman, and J.M. Chokreff. The detection and quantification of retinopathy using digital angiograms. *Medical Imaging, IEEE Transactions on*, 13(4):619 –626, dec 1994.

[66] J. Lowell, A. Hunter, D. Steel, A. Basu, R. Ryder, and R.L. Kennedy. Measurement of retinal vessel widths from fundus images based on 2-d modeling. *Medical Imaging, IEEE Transactions on*, 23(10):1196 –1204, oct. 2004.

[67] A. Mosquera, R. Dosil, V. Leborán, F. Pardo, F. Gómez-Ulla, B. Hayik, A. Pose, and M. Rodríguez. Art-vena: Retinal vascular caliber measurement. *Pattern Recogni-*

tion and Image Analysis. 1st Iberian Conference on Pattern Recognition and Image Analysis, 2003.

[68] X. Xu, M. Niemeijer, Q. Song, M. Sonka, M.K. Garvin, J.M. Reinhardt, and M.D. Abramoff. Vessel boundary delineation on fundus images using graph-based approach. *IEEE Transactions on Medical Imaging*, 30(6):1184 –1191, 2011.

[69] Dinesh K. Kumar, Behzad Aliahmad, and Hao Hao. Retinal vessel diameter measurement using unsupervised linear discriminant analysis. *ISRN Ophthalmology*, 2012, 2012.

[70] N. Barreira, M. Ortega, J. Rouco, M. G. Penedo, A. Pose-Reino, and C. Mari no. Semi-automatic procedure for the computation of the arteriovenous ratio in retinal images. *International Journal for Computational Vision and Biomechanics*, 3(2):135–147, 2010.

[71] Michael Kass, Andrew Witkin, and Demetri Terzopoulos. Snakes: Active contour models. *International Journal Of Computer Vision*, 1(4):321–331, 1988.

[72] J. F. Canny. A computational approach to edge detection. *IEEE Trans. Pattern Analysis and Machine Intelligence*, 8(6):679–698, 1986.

[73] H.F. Jelinek, C. Lucas, D.J. Cornforth, W. Huang, and M.J. Cree. Towards vessel characterization in the vicinity of the optic disc in digital retinal images. *in: McCane (Ed.),* P*roceedings of the Image and* V*ision* C*omputing* N*ew* Z*ealand*, 2005.

[74] Radim Chrástek, Matthias Wolf, Klaus Donath, Heinrich Niemann, and Georg Michelsont. Automated Calculation of Retinal Arteriovenous Ratio for Detection and Monitoring of Cerebrovascular Disease Based on Assessment of Morphological Changes of Retinal Vascular System. IAPR *Workshop on Machine Vision Applications, Nara, Japan*, 11-13:240–243, 2002.

[75] Wendy Aguilar, M. Elena Martínez-Pérez, Yann Frauel, Francisco Escolano, Miguel Angel Lozano, and Arturo Espinosa-Romero. Graph-based methods for

retinal mosaicing and vascular characterization. In *GbRPR*, volume 4538 of *Lecture Notes in Computer Science*, pages 25–36. Springer, 2007.

[76] Kai Rothaus, Xiaoyi Jiang, and Paul Rhiem. Separation of the retinal vascular graph in arteries and veins based upon structural knowledge. *Image and Vision Computing*, 27(7):864 – 875, 2009.

[77] A. Simó and E. de Ves. Segmentation of macular fluorescein angiographies. A statistical approach. *Pattern Recognition*, 34(4):795 – 809, 2001.

[78] H. Li, W. Hsu, M. L. Lee, and H. Wang. A piecewise Gaussian model for profiling and differentiating retinal vessels. In *ICIP03*, volume 1, pages 1069–1072, 2003.

[79] Enrico Grisan and Alfredo Ruggeri. A divide et impera strategy for automatic classification of retinal vessels into arteries and veins. *Engineering in Medicine and Biology Society, 2003. Proceedings of the 25th Annual International Conference of the IEEE*, 1:890 – 893, 2003.

[80] M. Niemeijer, B. van Ginneken, and M. D. Abràmoff. Automatic classification of retinal vessels into arteries and veins. *Medical Imaging 2009: Computer-Aided Diagnosis. Edited by Karssemeijer, Nico; Giger, Maryellen L.. Proceedings of the SPIE*, 7260:72601F–72601F–8, 2009.

[81] Mark Hall, Eibe Frank, Geoffrey Holmes, Bernhard Pfahringer, Peter Reutemann, and Ian H. Witten. The weka data mining software: An update. *SIGKDD Explorations*, 11(1), 2009.

[82] A. Zamperini, A. Giachetti, E. Trucco, and Khai Sing Chin. Effective features for artery-vein classification in digital fundus images. In *Computer-Based Medical Systems (CBMS), 2012 25th International Symposium on*, pages 1 –6, june 2012.

[83] S. G. Vázquez, N. Barreira, M. G. Penedo, M. Ortega, and A. Pose-Reino. Improvements in retinal vessel clustering techniques:towards the automatic computation of the arterio venous ratio. *Computing*, 90(3-4):197–217, 2010.

[84] S. G. Vázquez, N. Barreira, M. G. Penedo, M. Saez, and A. Pose-Reino. Using retinex image enhancement to improve the artery/vein classification in retinal images. In Aurlio Campilho and Mohamed Kamel, editors, *Image Analysis and Recognition*, volume 6112 of *Lecture Notes in Computer Science*, pages 50–59. Springer-Verlag, 2010.

[85] S. G. Vázquez, B. Cancela, N. Barreira, M.G. Penedo, M. Rodríguez-Blanco, M. Pena Seijo, G. Coll de Tuero, M.A. Barceó, and M. Saez. Improving retinal artery and vein classification by means of a minimal path approach. *Machine Vision and Applications*, pages 1–12, 2012.

[86] L.D. Cohen and R. Kimmel. Global minimum for active contour models: a minimal path approach. In *Computer Vision and Pattern Recognition, 1996. Proceedings CVPR '96, 1996 IEEE Computer Society Conference on*, pages 666 –673, June 1996.

[87] S. G. Vázquez, N. Barreira, M. G. Penedo, M. Penas, and A. Pose-Reino. Automatic classification of retinal vessels into arteries and veins. In *7th International Conference Biomedical Engineering (BioMED 2010)*, volume 1, pages 230–236, 2010.

[88] M. Saez, S. G. Vázquez, M. G. Penedo, M. A. Barceló, M. Pena-Seijo, G. Coll de Tuero, and A. Pose-Reino. Development of an automated system to classify retinal vessels into arteries and veins running title: Automated classification or retinal vessels. *Computer Methods and Programs in Biomedicine (in second revision)*, 2011.

[89] S. G. Vázquez, B. Cancela, N. Barreira, M. G. Penedo, and M. Saez. On the automatic computation of the arterio-venous ratio in retinal images: Using minimal paths for the artery/vein classifications. In *Proceedings of the 2010 International Conference on Digital Image Computing: Techniques and Applications*, DICTA '10, pages 599–603. IEEE Computer Society, 2010.

[90] Alexandru-Paul Condurache and Til Aach. Vessel segmentation in angiograms using hysteresis thresholding. In *Proceedings of MVA*, pages 269–272, 2005.

[91] Ro F. Frangi, Wiro J. Niessen, Koen L. Vincken, and Max A. Viergever. Multiscale vessel enhancement filtering. In *Medical Image Computing and Computer-Assisted Intervention (MICCAI)*, pages 130–137. Springer-Verlag, 1998.

[92] J.C. Parr and G.F. Spears. Mathematic relationships between the width of a retinal artery and the widths of its branches. *Am. J. Ophthalmol.*, 77:478 – 483, 1974.

[93] A.V. Stanton, B. Wasan, A. Cerutti, S. Ford, R. Marsh, P.P. Sever, S.A. Thom, and A.D. Hughes. Vascular network changes in the retina with age and hypertension. *J. Hypertens.*, 13:1724 – 1728, 1995.

[94] Li H, Hsu W, Lee ML, and Wong TY. Automatic grading of retinal vessel caliber. *Heart*, 52(7):1352–1355, 2009.

[95] M. Niemeijer, Xu Xiayu, A.V. Dumitrescu, P. Gupta, B. van Ginneken, J.C. Folk, and M.D. Abramoff. Automated measurement of the arteriolar-to-venular width ratio in digital color fundus photographs. *IEEE Transactions on Medical Imaging*, 30(11):1941 –1950, nov. 2011.

[96] X. Benavent, L. Martnez-Costa, G. Ayala, J. Domingo, and P. Marco. Semi-automated evaluation tool for retinal vasculopathy. *Computer Methods and Programs in Biomedicine*, 95(3):288 – 299, 2009.

[97] J.C. Parr and G.F. Spears. General caliber of the retinal arteries expressed as the equivalent width of the central retinal artery. *Am. J. Ophthalmol.*, 77:472 – 477, 1974.

[98] N. Patton, T. Aslam, T. Macgillivray, B. Dhillon, and I. Constable. Asymmetry of retinal arteriolar branch widths at junctions affects ability of formulae to predict trunk arteriolar widths. *Invest Ophthalmol Vis Sci*, 47(4):1329–1333, 2006.

[99] M. Ortega, N. Barreira, J. Novo, M. G. Penedo, A. Pose-Reino, and F. Gmez-Ulla. Sirius: A web-based system for retinal image analysis. *International Journal of Medical Informatics*, 79:722–732, 2010.

[100] A. Pose-Reino, M. Pena Seijo, M. González Penedo, M. Ortega Hortas, M. Rodríguez Blanco, P. Vega, J.L. Díaz Díaz, N. Fernández, J.C. Estévez, and F. Gómez-Ulla Irazábal. Estimation of the retinal microvascular calibre in hypertensive patients with the snakes semiautomatic model. *Med Clin (Barc)*, 135(4):145–150, 2010.

[101] S. G. Vázquez, N. Barreira, M. G. Penedo, M. Rodriguez-Blanco, F. Gómez-Ulla, A. González, and G. Coll de Tuero. Automatic arteriovenous ratio computation: Emulating the experts. In LuisM. Camarinha-Matos, Ehsan Shahamatnia, and Gonalo Nunes, editors, *Technological Innovation for Value Creation*, volume 372 of *IFIP Advances in Information and Communication Technology*, pages 563–570. Springer Berlin Heidelberg, 2012.

[102] M. Ortega, J. Rouco, J. Novo, and M. G. Penedo. Vascular landmark detection in retinal images. In *LNCS: Computer Aided Systems Theory, Revised Selected Papers EUROCAST 2009*, volume 5717, pages 211–217, 2009.

[103] S. G. Vázquez, N. Barreira, M.G. Penedo, and M. Rodríguez-Blanco. The significance of the vessel registration for a reliable computation of arteriovenous ratio. In Aurélio Campilho and Mohamed Kamel, editors, *Image Analysis and Recognition*, volume 7325 of *Lecture Notes in Computer Science*, pages 347–354. Springer-Verlag, 2012.

[104] H. Handels, Ch. Busch, J. Encarnação, Ch. Hahn, V. Kühn, J. Miehe, S.I. Pöppl, E. Rinast, Ch. Roßmanith, F. Seibert, and A. Will. Kamedin: a telemedicine system for computer supported cooperative work and remote image analysis in radiology. *Computer Methods and Programs in Biomedicine*, 52(3):175–183, 1997.

[105] Farah Magrabi, Nigel H. Lovell, and Branko G. Celler. A web-based approach for electrocardiogram monitoring in the home. *International Journal of Medical Informatics*, 54(2):145–153, 1999.

[106] Thorbjörn Lundberg, Goran Westman, Sten Hellstrom, and Herbert Sandstrom. Digital imaging and telemedicine as a tool for studying inflammatory conditions

in the middle ear-evaluation of image quality and agreement between examiners. *International Journal of Pediatric Otorhinolaryngology*, 72(1):73–79, 2008.

[107] Madona Azar and Robert Gabbay. Web-based management of diabetes through glucose uploads: Has the time come for telemedicine? *Diabetes Research and Clinical Practice*, 83(1):9 – 17, 2009.

[108] Seyyed Ehsan Mahmoudi, Alireza Akhondi-Asl, Roohollah Rahmani, Shahrooz Faghih-Roohi, Vahid Taimouri, Ahmad Sabouri, and Hamid Soltanian-Zadeh. Web-based interactive 2d/3d medical image processing and visualization software. *Computer Methods and Programs in Biomedicine*, 98(2):172 – 182, 2010.

[109] T. Goudas, C. Doukas, A. Chatziioannou, and I. Maglogiannis. A collaborative biomedical image-mining framework: Application on the image analysis of microscopic kidney biopsies. *Biomedical and Health Informatics, IEEE Journal of*, 17(1):82–91, 2012.

[110] W. Hsu, S. Antani, L.R. Long, L. Neve, and G.R. Thoma. Spirs: a web-based image retrieval system for large biomedical databases. *Int J Med Inform*, 78 Suppl 1, 2008.

[111] Chi-Ren Shyu, Carla E. Brodley, Avinash C. Kak, Akio Kosaka, Alex M. Aisen, and Lynn S. Broderick. Assert: A physician-in-the-loop content-based retrieval system for hrct image databases. *Computer Vision and Image Understanding*, 75(12):111 – 132, 1999.

[112] T. M. Lehmann, B. B. Wein, J. Dahmen, J. Bredno, F. Vogelsang, and M. Kohnen. Content-based image retrieval in medical applications: a novel multistep approach. In M. M. Yeung, B. L. Yeo, and C. A. Bouman, editors, *Proceedings of SPIE: Storage and Retrieval for Media Databases 2000*, volume 3972, pages 312–320, 2000.

[113] Daniel Keysers, Jrg Dahmen, Hermann Ney, Berthold Wein, and Thomas Lehmann. A statistical framework for model-based image retrieval in medical applications, 2003.

[114] Henning Müller, Nicolas Michoux, David Bandon, and Antoine Geissbuhler. A review of content-based image retrieval systems in medical applications-clinical benefits and future directions. *International Journal of Medical Informatics*, 73(1):1–23, 2004.

[115] Y. Li, T.P. Karnowski, K.W. Tobin, L. Giancardo, S. Morris, S.E. Sparrow, S. Garg, K. Fox, and E. Chaum. A health insurance portability and accountability act-compliant ocular telehealth network for the remote diagnosis and management of diabetic retinopathy. *Telemed J E Health*, 17(8):627–34, 2011.

[116] L. Tramontan, E. Poletti, D. Fiorin, and A. Ruggeri. A web-based system for the quantitative and reproducible assessment of clinical indexes from the retinal vasculature. *Biomedical Engineering, IEEE Transactions on*, 58(3):818 –821, march 2011.

[117] C. Swanson, K.D. Cocker, K.H. Parker, M.J. Moseley, and A.R. Fielder. Semiautomated computer analysis of vessel growth in preterm infants without and with rop. *Br J Ophthalmol*, 87(12):1474–7, 2003.

[118] Wallace DK, Freedman SF, Zhao Z, and Jung S. Accuracy of roptool vs individual examiners in assessing retinal vascular tortuosity. *Archives of Ophthalmology*, 125(11):1523–1530, 2007.

[119] M. Niemeijer, B. van Ginneken, M.J. Cree, A. Mizutani, G. Quellec, C.I. Sanchez, B. Zhang, R. Hornero, M. Lamard, C. Muramatsu, X. Wu, G. Cazuguel, J. You, A. Mayo, Qin Li, Y. Hatanaka, B. Cochener, C. Roux, F. Karray, M. Garcia, H. Fujita, and M.D. Abramoff. Retinopathy online challenge: Automatic detection of microaneurysms in digital color fundus photographs. *Medical Imaging, IEEE Transactions on*, 29(1):185 –195, jan. 2010.

[120] C.M. Wilson, K.D. Cocker, M.J. Moseley, C. Paterson, S.T. Clay, W.E. Schulenburg, M.D. Mills, A.L. Ells, K.H. Parker, G.E. Quinn, A.R. Fielder, and J. Ng. Computerized analysis of retinal vessel width and tortuosity in premature infants. *Invest Ophthalmol Vis Sci*, 49(8):3577–85, 2008.

[121] D. Fiorin and A. Ruggeri. Computerized analysis of narrow-field rop images for the assessment of vessel caliber and tortuosity. In *Engineering in Medicine and Biology Society,EMBC, 2011 Annual International Conference of the IEEE*, pages 2622 –2625, 30 2011-sept. 3 2011.

[122] A. Perez-Rovira, T. MacGillivray, E. Trucco, K.S. Chin, K. Zutis, C. Lupascu, D. Tegolo, A. Giachetti, P.J. Wilson, A. Doney, and B. Dhillon. Vampire: Vessel assessment and measurement platform for images of the retina. In *Engineering in Medicine and Biology Society,EMBC, 2011 Annual International Conference of the IEEE*, pages 3391 –3394, 30 2011-sept. 3 2011.

[123] J.J. Staal, M.D. Abramoff, M. Niemeijer, M.A. Viergever, and B. van Ginneken. Ridge based vessel segmentation in color images of the retina. *IEEE Transactions on Medical Imaging*, 23(4):501–509, 2004.

[124] B. Al-Diri, A. Hunter, D. Steel, M. Habib, T. Hudaib, and S. Berry. Review - a reference data set for retinal vessel profiles. In *Engineering in Medicine and Biology Society, 2008. EMBS 2008. 30th Annual International Conference of the IEEE*, pages 2262 –2265, 2008.

[125] Antonio Pose-Reino, Marta Pena Seijo, Manuel González Penedo, Marcos Ortega Hortas, María Rodríguez Blanco, Pilar Vega, José Luis Díaz Díaz, Noa Fernández, Juan Carlos Estévez, and Francisco Gómez-Ulla Irazábal. Determinación del calibre vascular retiniano en hipertensos con un método semiautomático basado en el modelo de snakes. *Medicina Clínica*, 135(4):145–150, 2010.

[126] VICAVR, VARPA Images for the Computation of the Arterio/Venular Ratio, database. http://www.varpa.es/vicavr.html, 2009.

[127] VICAVR-2, VARPA Images for the Computation of the Arterio/Venular Ratio, database. http://www.varpa.es/vicavr2.html, 2011.

[128] Gabriel Coll de Tuero, Quintí Foguet Boreu, Antonio Rodríguez-Poncelas, Ramon Creus, Maria Sanmartín, Narcis Salleras, Marc Saez, and Maria Antònia Barceló.

Assessment of self-monitoring of blood pressure in the diagnosis of isolated clinic hypertension. *Blood pressure*, 15(4):227–236, 2006.

[129] M. Pena, M. G. Penedo, M. Ortega, S. G. Vázquez, F. Gómez-Ulla, and A. Pose-Reino. Sirius, computerized tool for automatic analysis of retinal microcirculation. *Journal of Hypertension*, 29:e202, 2011.

[130] G. Coll de Tuero, S. G. Vázquez, A. Rodríguez Poncelas, M. A. Barcel 'o, J. Barrot de la Puente, M. G. Penedo, A. Pose-Reino, M. Pena-Seijo, and M. Saez. Prognostic value of the evolution of fundus lesions in newly diagnosed hypertensive patients at one year follow-up. *Journal of Hypertension*, 2013 (pending of acceptation).

[131] N. Barreira, S. G. Vázquez, C. Ferreira, E. Azevedo, J. Rouco, R. Rocha, and Aurélio Campilho. Web system for medical history management and advanced data analysis. In *18th meeting of ESNCH and 3rd meeting of CARNet*, May 2013 (pending of publication).

[132] J.M. Gauch and S.M. Pizer. Multiresolution analysis of ridges and valleys in grey-scale images. *IEEE Transactions on Pattern Analysis and Machine Intelligence*, 15:635–646, 1993.

[133] D. Eberly, R. Gardner, B. Morse, S. Pizer, and C. Scharlach. Ridges for image analysis. *Journal of Mathematical Imaging and Vision*, 4:353–373, 1994. 10.1007/BF01262402.

[134] Marco Foracchia, Enrico Grisan, and Alfredo Ruggeri. Luminosity and contrast normalization in retinal images. *Medical Image Analysis*, 9(3):179–190, 2005.

[135] D. J. Jobson, Z. Rahman, and G. A. Woodell. A Multiscale Retinex for Bridging the Gap Between Color Images and the Human Observation of Scenes. *IEEE Transactions On Image Processing*, 6(7), 1997.

[136] E. H. Land and J. J. McCann. Lightness and retinex theory. *J. Opt. Soc. Am.*, 61(1):1–11, Jan 1971.

[137] E. H. Land. An alternative technique for the computation of the designator in the retinex theory of color vision. *Proc Natl Acad Sci*, 83(10):3078–3080, 1986.

[138] D. J. Jobson, Z. Rahman, and G. A. Woodell. Properties and performance of a center/surround retinex. *IEEE Transactions On Image Processing*, 6(3), 1997.

[139] V. Caselles, R. Kimmel, and G. Sapiro. Geodesic active contours. *Computer Vision, IEEE International Conference on*, 0:694, 1995.

[140] J. A. Sethian. A fast marching level set method for monotonically advancing fronts. In *Proc. Nat. Acad. Sci*, pages 1591–1595, 1995.

[141] C. Mariño, M. G. Penedo, M. Penas, M. J. Carreira, and F. Gonzalez. Personal authentication using digital retinal images. *Pattern Analysis and Applications*, 9(1):21–33, 2006.

[142] P. Van den Elsen, J. Antoine Maintz, E.-J.D. Pol, and M. Viergever. Automatic registration of CT and MR brain images using correlation of geometerical features. *IEEE Transactions on Medical Imaging*, 14(2):384–396, 1995.

[143] M. Ortega and M. G. Penedo. *Retinal vessel tree as biometric pattern.* Biometrics, Ed. Intech Open Access Publishing. (Book Chapter), 2011.